Measurement of Deeply Virtual Compton Scattering at HERA

Vom Fachbereich Physik
der Universität Dortmund
und der Faculté des Sciences
Université Libre de Bruxelles
zur Erlangung des akademischen Grades
eines Doktors der Naturwissenschaften
genehmigte

Dissertation

von

Diplom–Physiker Rainer Stamen

aus Ense

Dortmund
November 2001

Abstract

In this thesis the results of the first measurement of Deeply Virtual Compton Scattering in electron–proton collisions at HERA are presented. The analysed data were taken with the H1 detector during the 1997 data taking period corresponding to an integrated luminosity of $8\,\mathrm{pb}^{-1}$. The differential cross sections $\frac{d\sigma}{dQ^2}$ and $\frac{d\sigma}{dW}$ of the reaction $ep \to e\gamma p$ have been measured in the kinematic domain $2 < Q^2 < 20\,\mathrm{GeV}^2$, $30 < W < 120\,\mathrm{GeV}$ and $|t| < 1\,\mathrm{GeV}^2$. After subtracting the contribution of the Bethe–Heitler process the photon proton cross section for the DVCS process $\sigma^{\gamma^* p \longrightarrow \gamma p}$ has been determined. The results are compared to QCD based calculations which are able to describe the measurement.

Kurzfassung

Die Ergebnisse der ersten Messung tiefvirtueller Comptonstreuung in Elektron–Proton Kollisionen bei HERA werden vorgestellt. Die analysierten Daten wurden mit dem H1 Detektor während der Datennahmeperiode 1997 aufgezeichnet und entsprechen einer integrierten Luminosität von $8\,\mathrm{pb}^{-1}$. Die differentiellen Wirkungsquerschnitte $\frac{d\sigma}{dQ^2}$ und $\frac{d\sigma}{dW}$ für die Reaktion $ep \to e\gamma p$ wurden im kinematischen Bereich $2 < Q^2 < 20\,\mathrm{GeV}^2$, $30 < W < 120\,\mathrm{GeV}$ und $|t| < 1\,\mathrm{GeV}^2$ gemessen. Nach Abzug des Beitrags des Bethe–Heitler Prozesses, wurde der Photon Proton Wirkungsquerschnitt $\sigma^{\gamma^* p \longrightarrow \gamma p}$ bestimmt. Die Ergebnisse werden mit QCD basierten Berechnungen verglichen, die in der Lage sind die Messung zu beschreiben.

Resumé

La présente thèse de doctorat porte sur l'analyse des données accumulées par l'expérience H1 auprès du collisionneur électron-proton HERA. Ce travail présente, pour la première fois, la mesure de la section efficace de la diffusion Compton profondément virtuel. Cette mesure utilise les évènements collectés durant la prise de données de 1997, accumulant une luminosité de 8 pb^{-1}. La section efficace de la réaction $ep \to e\gamma p$ est présentée differentiellement en $\frac{d\sigma}{dQ^2}$ et $\frac{d\sigma}{dW}$, dans la domaine $2 < Q^2 < 20\,\mathrm{GeV}^2$, $30 < W < 120\,\mathrm{GeV}$ et $|t| < 1\,\mathrm{GeV}^2$. Aprés la soustration du contribution Bethe–Heitler la section efficace photon–proton $\sigma^{\gamma^* p \longrightarrow \gamma p}$ est extrahit. Les résultats obtenus sont en bon accords avec certaines prédictions basées sur les calculs de chromodynamique quantique.

Contents

Chapter 1

Introduction

In high energy lepton–hadron scattering experiments an elementary particle, the lepton, is probing the hadron, a composite particle and thus delivers an excellent tool to investigate the hadrons structure. The results of early experiments led to the partonic picture of hadrons, in which they (e.g. the proton) consist of quarks. This was refined by more precise data and was one of the foundations of Quantum Chromo Dynamics (QCD) the quantum field theory of the strong interaction which describes hadron interactions on the basis of quarks and gluons (partons). Nowadays one of the aims of such lepton–hadron scattering experiments is the precise measurement of the parton density functions and the determination of the strong coupling constant α_s. This provides the possibility for very sensitive tests of the validity of different approximation methods which are applied in perturbative QCD calculations.

At the ep–collider HERA[1] a class of reactions has been 'rediscovered' the so called diffractive interactions which in the past have been observed in soft hadron–hadron scattering experiments and which are successfully described in the framework of Regge theory. The aim of current measurements of diffractive interactions is to understand these in the framework of perturbative QCD. Deeply Virtual Compton Scattering (DVCS), the reaction under investigation in this thesis, is a diffractive process for which pQCD calculations are expected to be reliable, and which furthermore opens the possibility to extract information about the structure of the proton which exceeds the meanwhile well known parton density functions.

The measurement of DVCS was proposed to access the generalised parton distributions which are generalisations of the ordinary parton densities and which exhibit also information about elastic form factors and the spin structure of the proton.

1.1 Deep Inelastic Scattering and the Structure of the Proton

In this section a general introduction to Deep Inelastic Scattering (DIS) is presented. The kinematic variables which define the process are introduced and the cross section is defined in terms of the two structure functions F_2 and F_L. These are discussed in the framework of the quark–parton model which is then refined by discussing the basic properties of perturbative QCD. At the end of this section our current knowledge about the partonic structure of the proton is presented.

---

[1] **H**adron **E**lektron **R**ing **A**nlage

Deep Inelastic Scattering (DIS)

In deep inelastic electron–proton scattering [1, 2, 3] the incoming electron interacts with the incoming proton by the exchange of a single gauge boson as shown in Figure 1.1. In neutral current events (NC) a virtual photon (γ^*) or a Z^0–boson is exchanged and an electron and the hadronic final state X are observed; in charged current interactions a W–boson is exchanged and the final state consists of a neutrino and the hadronic system X.
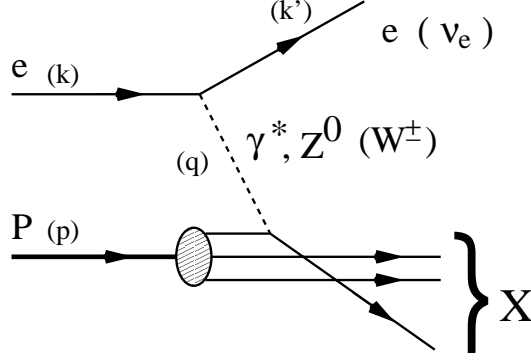

Figure 1.1: *This diagram for deep inelastic electron–proton scattering shows the exchange of a gauge boson between the incoming lepton and the hadron. In the quark–parton model the electron scatters elastically off a constituent quark of the proton. In neutral current events a neutral gauge boson is exchanged and the final state consists of the electron and the hadronic system X whereas in charged current events a charged W–boson is exchanged and a neutrino and the hadronic system X compose the final state of the reaction. The four vectors of the particles are denoted k and k' for the incoming and outgoing lepton respectively and p for the incoming proton.*

Kinematic Variables

The cross section is defined in terms of Lorentz invariant variables which ensures a convenient comparison of the measurements for different experimental setups. The variable Q^2 is the negative of the squared momentum of the exchanged boson,

$$Q^2 = -q^2 = -(k - k')^2, \tag{1.1}$$

where k is the four momentum of the incoming electron and k' denotes the four momentum of the outgoing lepton. The two Bjorken scaling variables x and y are defined as:

$$x = \frac{-q^2}{2pq}, \qquad y = \frac{pq}{pk}, \tag{1.2}$$

where p denotes the four momentum of the incoming proton. Thus x and y are dimensionless variables defined in the range $0 < x, y \leq 1$. The electron–proton centre of mass energy squared s is given by the equation

$$s = (k + p)^2. \tag{1.3}$$

At fixed centre of mass energy $\sqrt{s}$, only two of these four variables are independent due to energy momentum conservation[2]. When neglecting the electron and proton masses they are connected by the relation

$$Q^2 = xys. \qquad (1.4)$$

In addition W is defined as the centre of mass energy of the exchanged boson and the incoming proton

$$W^2 = (q+p)^2 \simeq ys - Q^2. \qquad (1.5)$$

Definition of the Cross Section and the Structure Function F_2

The cross section for neutral current ep interactions is defined such that it takes into account the different couplings of the gauge bosons to the electron and the propagator terms. In the region of low Q^2 ($Q^2 \ll M_{Z^0}^2$) only photon exchange contributes, resulting in a drastic simplification of the cross section expression. The Z^0 exchange and the interference between Z^0 and photon exchange can be neglected safely since the gauge boson masses enter the cross section by the propagator terms which leads to the following ratios for the contributions of the Z^0 exchange and the interference w.r.t. the contribution from single photon exchange to the cross section:

$$\frac{\sigma\left(Z^0\right)}{\sigma\left(\gamma^*\right)} \sim \left(\frac{Q^2}{Q^2 + M_{Z^0}^2}\right)^2, \qquad (1.6)$$

$$\frac{\sigma\left(\gamma^* Z^0\right)}{\sigma\left(\gamma^*\right)} \sim \left(\frac{Q^2}{Q^2 + M_{Z^0}^2}\right). \qquad (1.7)$$

At low Q^2 the differential electron–proton cross section can be written as:

$$\frac{d^2\sigma\left(x, Q^2\right)}{dx dQ^2} = \frac{4\pi\alpha_{em}^2}{xQ^4} \left[\left(1 - y + \frac{y^2}{2}\right) F_2\left(x, Q^2\right) - \frac{y^2}{2} F_L\left(x, Q^2\right)\right] \qquad (1.8)$$

where α_{em} denotes the electromagnetic coupling constant and the structure functions F_2 and F_L depend on the internal structure of the proton. They have to be determined experimentally since they currently cannot be calculated from first principles although non perturbative QCD methods based on lattice QCD exist [4]. The structure function F_2 is proportional to the sum of the cross sections for the exchange of longitudinally and transversely polarised photons whereas F_L only depends on the cross section for the exchange of longitudinally polarised photons. In the kinematic region of not too large y the contribution of the structure function F_L can be neglected and the cross section mainly depends on F_2. A compilation of the most precise F_2 measurements is shown in Figure 1.2 [5, 6, 7, 8, 9, 10, 11, 12]. The structure function F_2 is shown as a function of the photon virtuality Q^2 for different values of the scaling variable x. For values of $x \sim 0.2$ F_2 is independent of Q^2 which was first observed at SLAC [13, 14] and is known as *scaling*. For larger x values the structure functions decreases with increasing Q^2 whereas the opposite behaviour is observed for smaller values of x. The observation of scaling led to the advent of the quark–parton model [15, 16, 17, 18] which was refined by the observation of scaling violations [19] for large and small values of x. These effects have been successfully described in the framework of Quantum Chromo Dynamics (QCD) [20, 21, 22, 23].

---

[2]The reaction is assumed to be independent on the azimuthal angle and therefore this degree of freedom has not been considered.
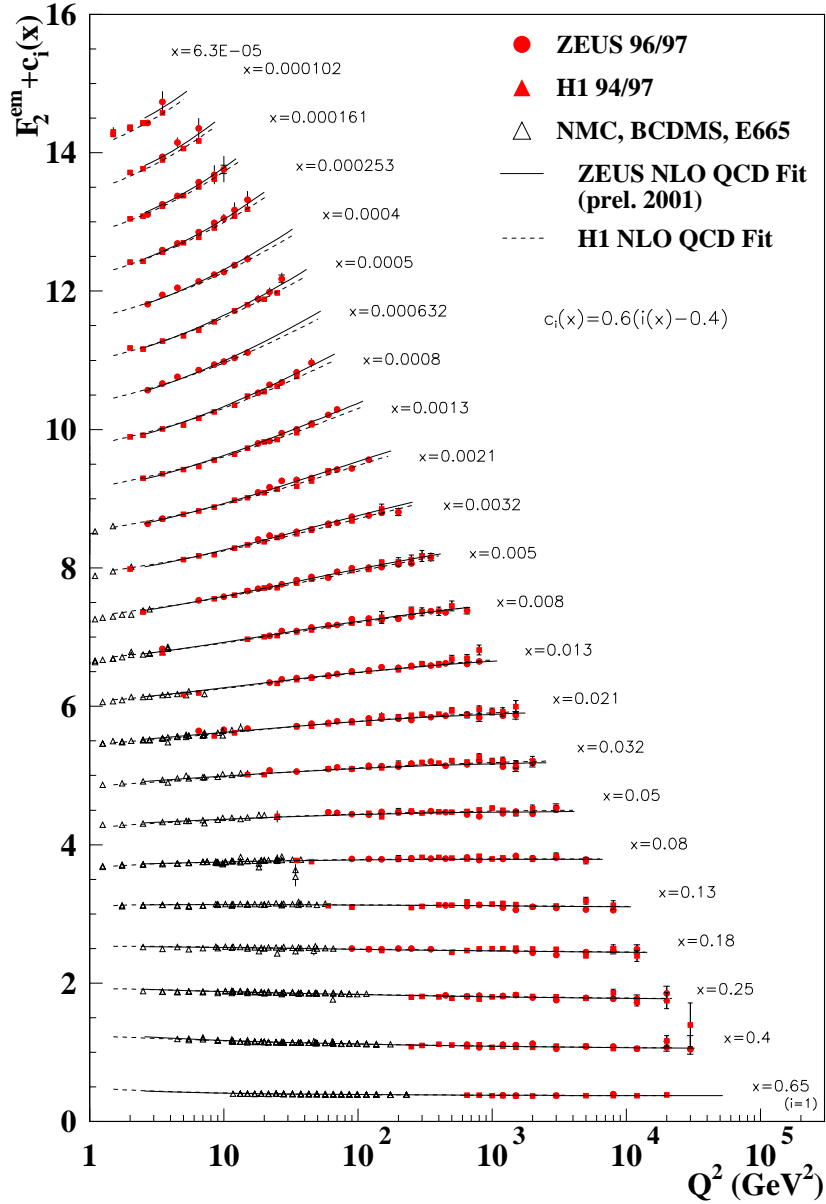
Figure 1.2: *Compilation of the most precise F_2 measurements up to date in dependence of Q^2 for different values of x. The data in the region of low Q^2 and medium to large x are taken by fixed target experiments. These kinematic region has been extended by about 2 orders of magnitude in x and Q^2 by the HERA experiments H1 and ZEUS. The data are compared to next to leading order QCD fits which are able to reproduce the measurements in the whole kinematic range [5, 6, 7, 8, 9, 10, 11, 12].*

The Quark Parton Model

The observation of scaling at SLAC in the kinematic region $1 < Q^2 < 10\,\text{GeV}^2$ for $x \simeq 0.2$ was interpreted by Bjorken and Paschos [15, 16] and by Feynman [17, 18] as being due to the partonic

structure of the proton. In a Thompson–model of the proton in which the proton is an extended particle consisting of a continuous charge distribution a steeply falling structure function F_2 would be expected for all values of x as may be understood as follows. The wavelength of the virtual photon is proportional to the inverse of its virtuality $\lambda \sim 1/\sqrt{-q^2}$ which means that the photon probes smaller distances for larger Q^2 values and therefore it would be sensitive to smaller and smaller fractions of the total electric charge of the proton. Since the coupling of the photon is proportional to the charge this would lead to an F_2 falling with increasing values of Q^2 for all values of x.

In the quark–parton model the proton consists of three point-like partons which can be identified with the quarks introduced by Gell–Mann and Zweig [24, 25] to explain the spectroscopic hadron data. The proton is built from two up–quarks with fractional charge 2/3 and one down–quark with fractional charge -1/3. In this model the electron scatters elastically off one of the three quarks by single photon exchange. Since the time scale of the interaction is very small in comparison to interactions between the constituent quarks the proton can be treated for cross section calculations as an incoherent sum of these three quarks. This model leads to the observed scaling behaviour and the structure function F_2 may then be written as

$$F_2(x) = \sum_f e_f^2 x q_f(x) \tag{1.9}$$

where e_f is the charge of the struck quark and $q_f(x)$ are the quark density functions. In this model, x can be interpreted, in the infinite momentum frame, as the momentum fraction of the protons momentum carried by the struck quark.

By exploring a larger region in the x–Q^2 plane the violation of the scaling behaviour was observed as mentionend before. In addition it was found when summing up the momentum carried by the quarks that only a fraction of the total proton momentum is carried by these partons. These effects can be understood in the framework of Quantum Chromo Dynamics (QCD).

Quantum Chromo Dynamics (QCD)

Quantum Chromo Dynamics is the quantum field theory for strong interactions. With the large success of Quantum Electrodynamics (QED) in describing electromagnetic interactions at high energies it was recognised that renormisable quantum field theories are the most appropriate way to describe interactions of high energy particles. Until the advent of QCD a phenomenological theory the so called Regge theory existed which was able to describe *soft* hadron–hadron interactions (see chapter 1.2). With the observation of the substructure of hadrons a new theory for strong interactions became necessary.

In QCD the proton is built from quarks (as in the quark–parton model) which are spin 1/2 fermions. These are bound together by gluons which are the spin 1 gauge bosons of QCD, a non–abelian gauge theory invariant under SU(3) colour symmetry. In the framework of QCD colour corresponds to a new degree of freedom which takes the rôle of the electric charge in QED. It is carried by the quarks and in contrast to QED also by the gauge bosons, the gluons as a consequence of the non–abelian character of the theory. This leads to a self coupling of the gluons and hence to fundamental differences between QCD and QED.

Renormalisation and the Running Coupling

In perturbative QCD calculations divergent integrals appear which are treated by a renormalisation scheme and hence lead to an effective coupling constant $\alpha_s\left(\mu_r^2\right)$ depending on the energy scale μ_r^2. The requirement that the calculated cross sections are independent of the renormalisation scale μ_r^2 leads to the Renormalisation Group Equation (RGE) which in leading log. approximation (LLA) leads to the scale dependence of the coupling constant:

$$\alpha_s\left(\mu_r^2\right) = \frac{12\pi}{(33 - 2n_f)\ln\left(\mu_r^2/\Lambda_{QCD}^2\right)}. \tag{1.10}$$

Λ_{QCD} is a free parameter which has to be determined by experiments. It represents the lower limit of μ_r for which perturbative QCD calculations are expected to be predictive. n_f is the number of quark flavours with mass $m_q^2 < \mu_r^2$. In contrast to QED the effective strong coupling constant α_s is decreasing for larger values of μ_r^2 as consequense of the gluon self coupling.

The two extremes of small and large μ_r^2 which by the uncertainty principle correspond to large and small distances respectively, are called infrared slavery and asymptotic freedom. In the region of infrared slavery α_s is large and perturbative QCD calculations are not applicable. This long range effect is responsible for the confinement of partons in bound states, the hadrons. In the region of asymptotic freedom α_s is small and the perturbative expansion series (in powers of α_s) of QCD calculations is expected to converge fast which means that quarks can be treated as free particles.

In a pQCD calculation to a fixed order in α_s the cross section depends on the renormalisation scale μ_r^2 through the coupling constant $\alpha_s\left(\mu_r^2\right)$. When calculating up to all orders the terms involving μ_r^2 cancel and the cross section becomes independent of the renormalisation scale.

The Factorisation in DIS

The theorem of factorisation has been proven for hard scattering [26] and states that short range effects in the scattering amplitude, calculable in pQCD, can be separated from long range effects which are accounted to the parton density functions (pdf's). The proton structure function F_2 can be written as

$$F_2\left(x, Q^2\right) = \sum_{i=q,\bar{q},g} \int_x^1 d\xi f_i\left(\xi, \mu_r^2, \mu_f^2, \alpha_s\right) \cdot C_i^V\left(\frac{x}{\xi}, \frac{Q^2}{\mu_r^2}, \mu_f^2, \alpha_s\right). \tag{1.11}$$

In this decomposition μ_f^2 is the factorisation scale, f_i are the parton density functions and C_i^V are the coefficient functions. These describe the interaction of the exchanged boson V with a quark i (see Figure 1.3) which is calculable in perturbative QCD. The factorisation scale μ_f^2 defines the energy scale above which additional parton emissions from the quark are included in the perturbative QCD calculation. Long range effects which are not calculable in pQCD (e.g. parton emission with $k_T^2 < \mu_f^2$) are absorbed in the parton density functions f_i which therefore also become dependent on the factorisation scale μ_f^2. The parton density functions f_i can be interpreted in leading order calculations as probability to find a parton of type i for a certain value of x in the hadron. These are universal functions which only depend on the hadron type whereas the coefficient functions C_i^V are process dependent.
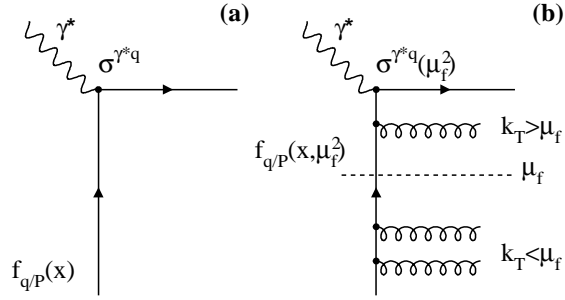
Figure 1.3: a) *Leading order diagram for the interaction of the virtual photon with a quark of the proton. b) In NLO calculations diagrams with e.g. additional parton emission have to be taken into account. The factorisation theorem states that parton emission with a large scale is taken into account in the scattering amplitude, calculable in pQCD whereas parton emission below the scale μ_f is absorbed in the parton density function which has to be determined experimentally.*

Parton Density Functions

Since the parton density functions cannot be calculated from first principles they have to be extracted from the experimental data although perturbative QCD calculations predict the evolution (e.g. in Q^2) of parton densities once they are known at at a certain starting point $(f_i(x, Q_0^2))$. The proton structure function F_2 can be developed in a perturbation series in powers of α_s which contains terms $\alpha_s \ln (Q^2/Q_o^2)$, $\alpha_s \ln (1/x)$ and mixed terms $\alpha_s (Q^2/Q_o^2) \ln (1/x)$. Three different kind of evolution equations exist differing in the choice of terms added up from this perturbative expansion. The evolution of the parton density functions corresponds to a ladder diagram shown in Figure 1.4 and the summation of certain terms can be interpreted as ordering in either k_T or x of the rungs from the ladder (see e.g. [27]).

DGLAP Evolution and Operator Product Expansion

With the Dokshitzer, Gribov, Lipatov, Altarelli and Parisi (DGLAP) evolution equation [28, 29, 30, 31] the evolution of the parton density functions in dependence of Q^2 is predicted. In leading order the two coupled equations can be written as:

$$\frac{dq_i(x, Q^2)}{d \ln Q^2} = \frac{\alpha_s(Q^2)}{2\pi} \int_x^1 \frac{dz}{z} \left[\sum_j q_j(z, Q^2) P_{ij}\left(\frac{x}{z}\right) + g(z, Q^2) P_{ig}\left(\frac{x}{z}\right) \right], \qquad (1.12)$$

$$\frac{dg(x, Q^2)}{d \ln Q^2} = \frac{\alpha_s(Q^2)}{2\pi} \int_x^1 \frac{dz}{z} \left[\sum_j q_j(z, Q^2) P_{gj}\left(\frac{x}{z}\right) + g(z, Q^2) P_{gg}\left(\frac{x}{z}\right) \right]. \qquad (1.13)$$

Here $q_i(z, Q^2)$ and $g(z, Q^2)$ denote the quark and the gluon density functions. P_{ij} are the splitting functions (see Figure 1.5) which describe the parton emission calculable in perturbative QCD. Starting from a certain input density function $f_i(x, Q_0^2)$ the parton density is calculable for higher Q^2 values by solving the DGLAP evolution equations. This scheme corresponds to a strong k_T ordering $(k_{T,1} \ll k_{T,2} \ll ... \ll Q^2)$ of the subsequent parton emission as can be seen in Figure 1.4 whereas the ordering in x is only weak $(x_1 > x_2 > ... > x)$.
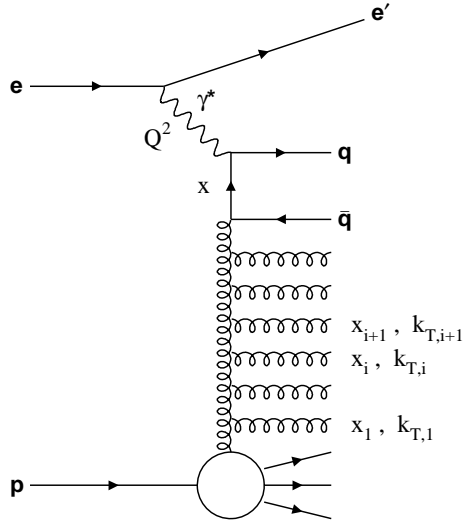
Figure 1.4: *In perturbative QCD the evolution of the structure function F_2 can be described by such a ladder diagram. In the DGLAP approach the subsequent parton emissions are strongly ordered in k_T $\left(k_{T,1} \ll k_{T,2} \ll ... \ll Q^2\right)$ and only weak ordering in x $(x_1 > x_2 > ... > x)$ is required. In the BFKL approach which is expected to be valid at very low x a strong ordering in x $(x_1 \gg x_2 \gg ... \gg x_i)$ is required whereas in k_T no ordering is present.*
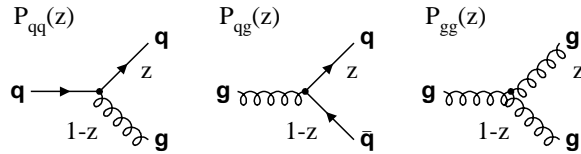

Figure 1.5: *First order diagrams for three different splitting functions $P_{ij}(z)$.*

In a more formal approach the DGLAP evolution equations can be derived by the method of Operator Product Expansion (OPE) [32]. The matrix element of the reaction $ep \longrightarrow eX$ is proportional to the hadronic transition amplitude

$$M \sim\, < X|O|p > \tag{1.14}$$

where O is the operator which describes the transition from the initial proton $|p >$ to the hadronic final state $< X|$ (see Figure 1.1). The total cross section is proportional to the square of the matrix element

$$\sigma \sim |M|^2 \sim \sum_X < p|O'|X >< X|O|p > \tag{1.15}$$

which can be simplified when summing up all contributions of the hadronic final state X which leads to the relation

$$|M|^2 \sim\, < p|O'O|p > . \tag{1.16}$$

This method can be visualised in the quark–parton model by the diagram in Figure 1.6. The Operator Product Expansion consists of expanding the product $O'O$ in terms of quark and gluon fields where the leading diagram (Figure 1.6) can be interpreted as a if a quark is projected out
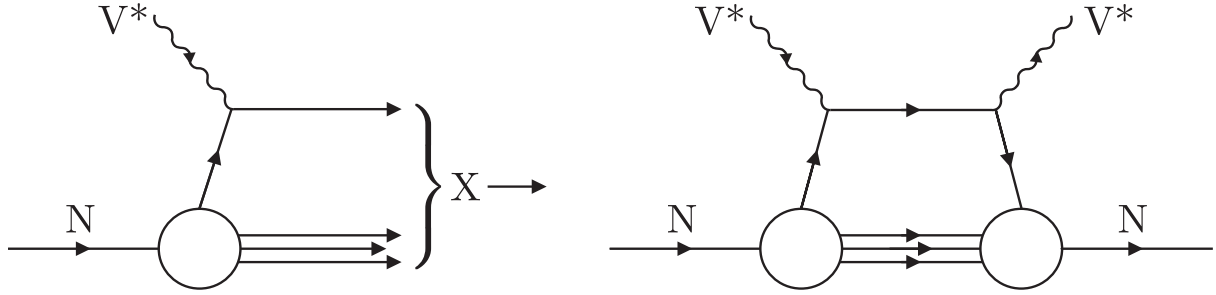
Figure 1.6: *left: leading order diagram for the matrix element $X|O|p>$; right: leading order diagram for the matrix element $<p|O'O|p>$.*

the proton which then interacts with the virtual photon and subsequently enters the proton again. In the context of the factorisation theorem the upper part of the diagram represents the hard scattering amplitude calculable in pQCD and the lower part is a representation for the parton densities. Note that the quark line between the vertices of the coupling gauge boson is on shell due to energy momentum conservation.

BFKL and CCFM Evolution

Several other approaches exist to model the structure function F_2 in regions where the DGLAP approximation does not hold. In the approach by Balitsky, Fadin, Kuraev and Lipatov (BFKL) [33, 34, 35] the terms in $\ln(1/x)$ of the perturbative expansion of F_2 are summed up which leads to a strong ordering in x in the ladder diagram (Figure 1.4) $(x_1 \gg x_2 \gg ... \gg x_i)$ The BFKL equation can be written in terms of the unintegrated gluon density $f_g(x, k_T^2)$ from which the ordinary gluon distribution can be calculated by integration over k_T. It thus predicts the evolution of F_2 as function of x.

The approach by Catani, Ciafaloni, Fiorani and Marchesini (CCFM) [36, 37, 38] gives the BFKL solution at low x and the DGLAP one at large Q^2. It is based on a strong angular ordering of subsequent parton emission.

Todays structure function measurements can be entirely described in the DGLAP scheme for $Q^2 \gg 1\,\mathrm{GeV}^2$ but there is indication that the DGLAP approach fails to describe certain exclusive measurements of the hadronic final state in ep collisions [39, 40] which might be the first sign for BFKL effects.

Parameterisations of Parton Density Functions

In order to model the structure function F_2 several parameterisations for parton densities exist where most of them are based on a polynomial ansatz (e.g. $xg = Ax^\delta(1-x)^\eta$) at a certain starting scale Q_0^2. The evolution to higher values of Q^2 is then performed by solving the DGLAP evolution equations and the free parameters of this ansatz are determined by a fit to the data.

The approach of Glück, Reya and Vogt (GRV) [41] is based on a dynamical model in which at a very low scale (chosen to be $Q_0^2 \simeq 0.34\,\mathrm{GeV}^2$), only valence like partons are assumed to exist. The parton density functions at higher values of Q^2 are then calculated by the DGLAP

evolution equations.

Figure 1.7 shows the GRV parton density functions at a) the starting scale $Q^2 = \mu^2$ and b) after evolution to $Q^2 = 5\,\text{GeV}^2$ [42]. It can be seen that the valence like gluon density very fastly evolves to low values of x which can be understood by gluon radiation from the valence partons which is resolved for larger values of Q^2. In Figure 1.7c) a fit to the data for the different parton flavours is shown [43] at the scale $Q^2 = 10\,\text{GeV}^2$ which compares qualitatively with the GRV prediction.
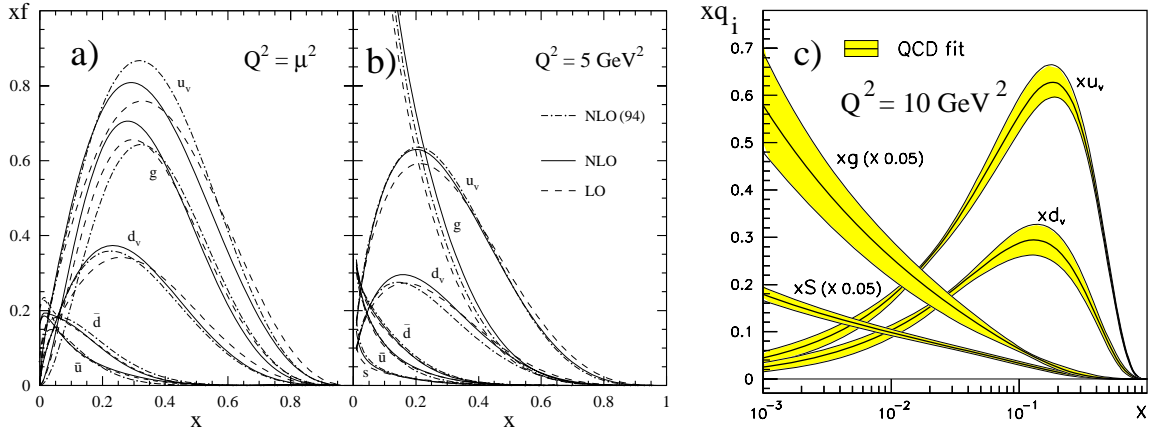

Figure 1.7: *a) parton density functions in the GRV approach at the starting scale $Q^2 = \mu^2$; b) pdf's after evolution at $Q^2 = 5\,\text{GeV}^2$; c) QCD fit of the pdf's at $Q^2 = 10\,\text{GeV}^2$ [42, 43].*

1.2 Diffractive Scattering

The investigation of hadron–hadron interactions at high energies has been a rich source of information about the strong interaction. Especially the study of events with low momentum transfer has been of great interest [44, 45, 46]. In the pre QCD era these kind of events have been successfully described in the framework of Regge-theory [47] which is based on the S-Matrix approach. In this model the hadron–hadron interactions are described by the exchange of meson and baryon trajectories. At high energies the pomeron trajectory, corresponding to a pseudo particle with the quantum numbers of the vacuum, exchange was proposed to explain the rise of cross sections at high energies. Measurements of diffractive events with jet production gave the first hint of the partonic structure of the pomeron.

Diffractive events have also been observed in deep inelastic electron–proton scattering at HERA where the pomeron is exchanged between the photon fluctuated into a hadronic state and the proton. The large range of the photon virtuality Q^2 available at HERA opened the possibility to measure precisely the partonic structure of the diffractive exchange.

In a QCD based model for the pomeron exchange, diffractive events were proposed to be described by a two gluon exchange model which can be best tested studying vector meson production. This model then leads consequently to the concept of generalised parton distributions which relates also to the partonic structure of the proton.

Diffractive Scattering in Soft Hadron–Hadron Interactions

Experimental Observations

In Figure 1.8 the cross section for elastic proton–proton scattering is plotted for different centre of mass energies as a function of $|t|$ where t is the squared momentum transfer between the two hadrons [46]. For low centre of mass energies a falling cross–section is observed where the slope gets steeper towards higher centre of mass energies. In addition a minimum and a maximum appear. This shape is similar to the diffraction pattern as observed when a plane wave of light passes a disc. The shape of the cross section down to the first minimum can be approximated
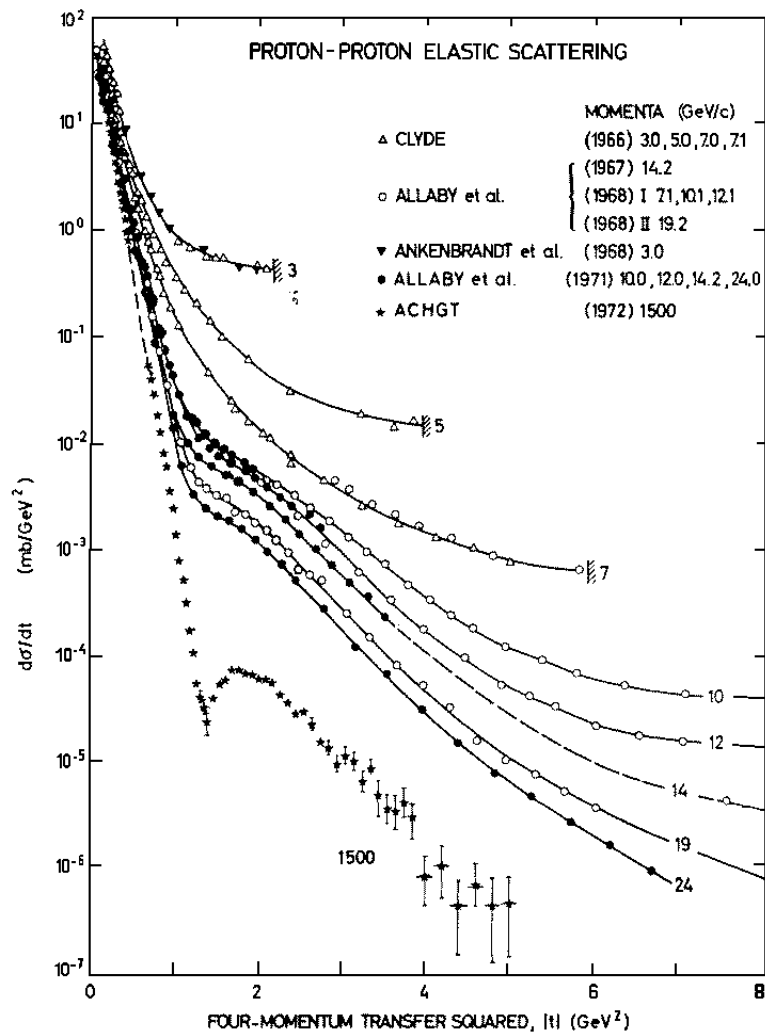

Figure 1.8: *Compilation of measurements of the differential cross section for elastic pp scattering as a function of $|t|$ for different values of the centre of mass energy* [46].

11

by an exponential function of the form[3]:

$$\frac{\mathrm{d}\sigma}{\mathrm{d}t} = \left(\frac{\mathrm{d}\sigma}{\mathrm{d}t}\right)\bigg|_{t=0} e^{-b|t|} \tag{1.17}$$

with $b \sim 10\,\mathrm{GeV}^{-2}$.

The data can be interpreted in the spirit of the similarity between optical and hadronic diffraction [45]. In this picture one discusses the scattering of a fast hadron represented by a plane wave in the field of a hadron at rest. In optical diffraction the following formula holds for $kR \gg 1$:

$$\frac{I}{I_0} \simeq 1 - \frac{R^2}{4}k^2\theta^2 \tag{1.18}$$

which describes the fraction of observed intensity w.r.t. the initial intensity as a function of the diffraction angle θ, where R is the radius of the disc and k denotes the wave number of the incident light wave. If one relates the scattering angle θ to the momentum transfer t in hadron–hadron interactions, the wave number k to the momentum of the hadrons, and the radius of the disc R to the mass of the pion one can deduce a t-slope b of $b = 12.5\,\mathrm{GeV}^{-2}$ resulting in the right order of magnitude as measured.

Aspects of Regge Theory

The only theory to describe soft hadron–hadron interactions is Regge theory [47]. Apart from the fact that it was invented well before QCD, it still provides the only possibility to predict cross sections for these kind of reactions since perturbative QCD calculations are not applicable due to the absence of a hard scale in the process.

Regge theory was introduced in the framework of non–relativistic quantum mechanics and generalised the idea of Yukawa explaining particle interactions by the exchange of virtual particles. Later it was generalised to also describe relativistic particle interactions. It is based on S-Matrix theory which connects the wave function of the initial state $|i>$ with that of the final state $|f>$ by the relation:

$$|f> = S|i> . \tag{1.19}$$

The foundations of Regge–theory are the following axioms:

- The superposition principle states that a particle state ψ_γ can be decomposed linearly in the form $|\psi_\gamma> = \alpha|\psi_\alpha> + \beta|\psi_\beta>$ correctly taking into account the selection rules.

- The forces are required to be of short range. This is fulfilled for strong interactions since the interaction range is of the order of the inverse of the pion mass: $R \sim 1/m_\pi \sim 10^{-15}\,\mathrm{m}$.

- The Lorentz invariance principle states that the S-Matrix is a Lorentz scalar which itself only depends on Lorentz scalars.

- The unitarity requirement which corresponds to the conservation of probability states that $S^\dagger S = 1 = SS^\dagger$.

- Maximal analyticity of first order is required (see below).

---

[3]Note that in a more careful analysis the sum of two exponatial funtions has to be used [46]

- Generalisation of angular momentum in the complex plane is introduced (see below).

If one considers the reaction $A + B \longrightarrow C + D$. The Mandelstam variables s_{ij} are real numbers defined by relationes of the form $s_{ij} = (\pm P_i \pm P_j)^2$ with $i, j \in (A, B, C, D)$. Maximal analyticity of first order means that these variables can be extended into the complex plane which allows the use of complex analysis. The S-Matrix can now be written as a function of these complex numbers. In the limit of real numbers one gets back the S-Matrix for particle reactions in the physical region. A consequence of this axiom is the crossing symmetry which states that if the reaction $A + B \longrightarrow C + D$ is described by the variable $s = (P_A + P_B)^2$ and $t = (P_A - P_C)^2$ by the S–Matrix $S(s, t)$ one can calculate the amplitude[4] for the reaction $A + \bar{C} \longrightarrow D + \bar{B}$ by exchange of s and t which leads to the amplitude $S(t, s)$ as depicted in Figure 1.9.
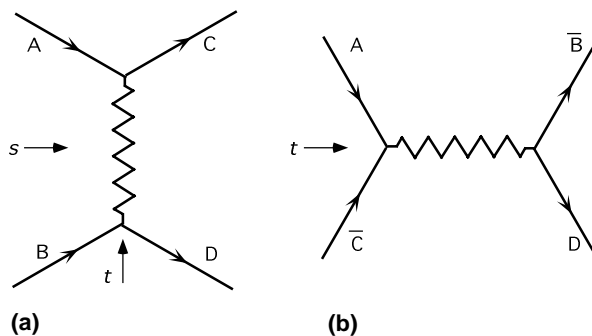

(a)   **(b)**

Figure 1.9: *The two diagrams show the reactions $AB \longrightarrow CD$ and $A\bar{C} \longrightarrow \bar{B}D$ respectively. These processes share the same scattering amplitude. If the s-channel reaction a) can be described by the exchange of a particle in the t-channel then Regge theory predicts that the t-channel reaction b) is dominated by production of a resonance which subsequently decays into the final state. This prediction originates from the crossing symmetry being the consequence of one of the axioms of Regge theory.*

The solution of the non relativistic Schrödinger equation are eigenstates of the angular momentum with integer or half integer eigenvalues. In Regge theory the angular momentum is continued in the complex plane. The physical meaningful results are achieved by projecting the results on the real axis of the complex angular momentum plane.

If one considers the reaction $\pi^+ \pi^- \longrightarrow p\bar{p}$ one can describe it by the fusion of the two pions to a ρ, ρ' or even higher excited states which than decay into the $p\bar{p}$ pair. This corresponds to the diagram in Figure 1.9 b with $A = \pi^+$, $\bar{C} = \pi^-$, $\bar{B} = \bar{p}$ and $D = p$. All intermediate states $(\rho, \rho', ...)$ must have the same quantum numbers except for the angular momentum J which only depends on the relative angular momentum of the two incident pions. The allowed states are hence a discrete series of states with integer spin. Regge theory states now that the scattering amplitude of the crossed channel $(\pi^+ p \longrightarrow \pi^+ p)$ can be calculated by exchanging the Mandelstam variables s and t in the scattering amplitude

$$S_{\pi^+ p \longrightarrow \pi^+ p}(s, t) = S_{\pi^+ \pi^- \longrightarrow p\bar{p}}(t, s). \tag{1.20}$$

It was observed that all intermediate states of the reaction $\pi^+ \pi^- \longrightarrow p\bar{p}$ lie on a straight line the so called ρ–trajectory when plotting the spin of the physical states as function of the squared

---

[4]Note that the s and t channel are defined according to [47].

mass which is shown in Figure 1.10. The ρ–trajectory connects the s–channel ($t < 0$) and t–channel ($t > 0$) region which corresponds in this example to the reaction $\pi^+ p \longrightarrow \pi^+ p$ with $t = m^2$. When extending the trajectory into the s–channel region the value $\alpha(t) = Re(J)$ is used to predict cross sections for the crossed channel (see below) which agrees well with the observations. The trajectory depends on the intercept $\alpha(0) = \alpha_0$ and the slope α'

$$\alpha(t) = \alpha_0 + \alpha' \cdot t. \tag{1.21}$$

Figure 1.10 shows that the measurements of the ρ trajectory in the s–channel region agree well with the prediction when continuing the Regge trajectory from the t–channel region into the s–channel region. A large amount of data from hadron–hadron scattering can be explained by Regge theory using the known meson and baryon spectra as origin for Regge trajectories.
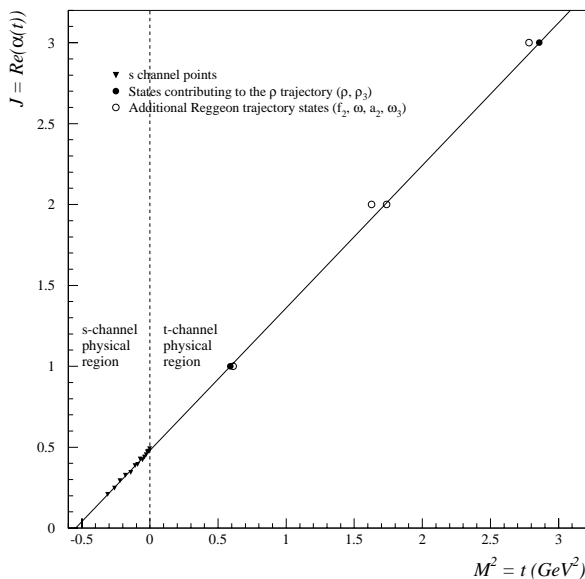

Figure 1.10: *The ρ trajectory: In the t–channel region the bound states (ρ, ρ_3) are shown. A straight line through these states is continued into the s–channel region where it is compared to data from hadron–hadron interactions.*

The total cross section for hadron–hadron interactions is connected to the imaginary part of the forward scattering amplitude $\mathcal{A}$ by the optical theorem which states

$$\sigma_{tot}(AB) \sim \frac{1}{s} \mathrm{Im} \mathcal{A} (AB \longrightarrow AB)(s, t = 0). \tag{1.22}$$

Hence this relation can be used to calculate total cross sections when knowing the scattering amplitude. Regge theory provides predictions e.g. for the energy dependence of total cross section:

$$\sigma_{tot} \sim s^{2\alpha(0)-2}, \tag{1.23}$$

where s is the centre of mass energy of the hadron–hadron interaction. The measurement of the energy dependence of the cross section therefore provides access to the intercept α_0 of the trajectory. When measuring the t–dependence of cross sections also the determination of the slope α' becomes possible (see Figure 1.10).

It was observed (see Figure 1.11) that the total cross section decreases with energy for low energies which is explained by Regge–trajectories originating from the known baryon and meson spectra whereas the rise of the cross section for high energies was not expected. To account for
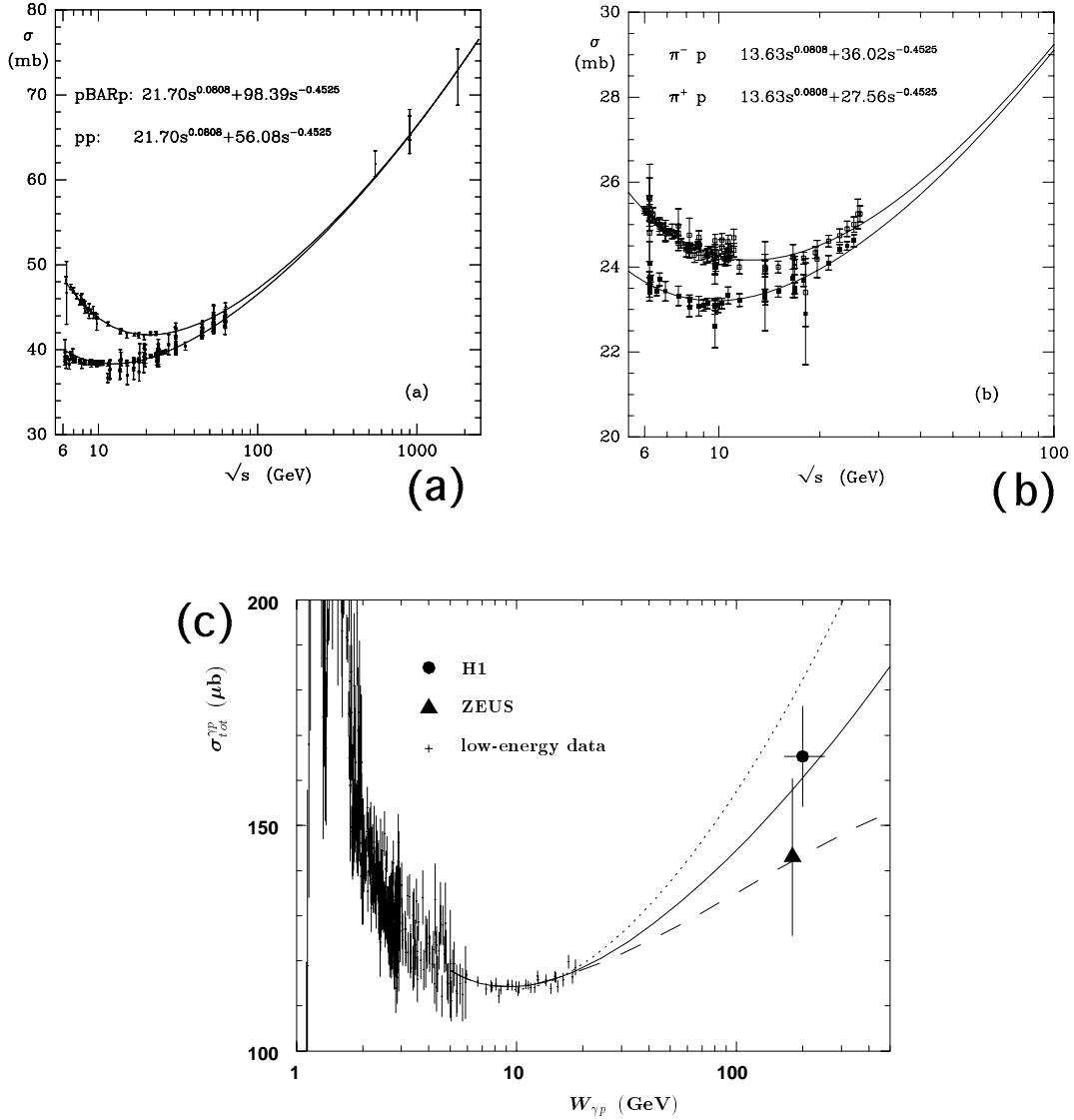
Figure 1.11: *Compilation of measurements for total hadron–hadron cross sections as a function of the centre of mass energy $\sqrt{s}$ for different hadron types. a) proton–proton and proton–antiproton cross sections; b) π^+p and π^-p cross sections; c) photon–proton cross sections, where the photon can be treated as hadron in the vector meson dominance model (see text)* [48].

this rise the Pomeron trajectory was introduced which is characterised by the quantum numbers of the vacuum. From the rise of σ_{tot} for different reactions the Pomeron trajectory can be derived [48]:

$$\alpha(t) = 1.08 + 0.25 \cdot t. \qquad (1.24)$$

It is measured in the s–channel region and a real particle in the t–channel regime is expected but not yet found. This particle is most probably glueball, i.e. a composite state of two valence

gluons with the quantum numbers of the vacuum.

With introduction of the Pomeron trajectory also the observations discussed at the beginning of this section can be explained. The shrinkage of the diffractive peak can be predicted since Regge theory states:

$$b = b_0 + 2\alpha' ln\left(\frac{s}{s_0}\right) \tag{1.25}$$

and the double peak structure of the differential cross section as function of t at high energies (see Figure 1.8) can be explained by interference between single and multiple Pomeron exchange.

Following the idea by Ingelmann and Schlein [49] the structure of the vacuum exchange was investigated using diffractive events in presence of a hard scale suitable to resolve the partonic structure of the Pomeron. In proton–antiproton interactions this was done studying diffractive events with high transverse momentum jets. The measured cross section for this kind of events has been interpreted to be dominated by a large gluon content of the Pomeron [50, 51]. Following the same idea at HERA diffractive events have been investigated in the presence of a hard scale.

Diffraction in Electron–Proton Interactions

In the first years of HERA operation a widely unexpected large amount of diffractive events was observed [52, 53, 54, 55].

Inclusive Diffraction in Electron–Proton Interactions

Such events are identified by the presence of a large gap in rapidity η^5 in which no particle production is observed. The corresponding diagram for diffraction in electro–production is shown in Figure 1.12. The hadronic system Y propagates in the direction of the incoming proton while the system X is observed in the central part of the detector. Due to the high centre of mass energy in the photon–proton system it can be assumed that for the main part of the available phase space Pomeron exchange is dominant. In order to account for the new degrees of freedom for diffractive processes it is necessary to introduce the additional kinematic variables

$$M_X^2 = p_X^2, \qquad M_Y^2 = P_Y^2, \qquad t = (P - p_Y)^2,$$

$$x_{I\!P} = \frac{q \cdot (P - p_Y)}{q \cdot P}, \qquad \beta = \frac{x}{x_{I\!P}} = \frac{-q^2}{2q \cdot (P - P_Y)},$$

where M_X and M_Y are the invariant masses of the hadronic systems X and Y and t is the momentum transfer squared at the proton vertex. $x_{I\!P}$ can be interpreted as the longitudinal momentum carried by the exchanged Pomeron whereas β is the momentum fraction of the struck quark w.r.t. the pomeron momentum.

The cross section for diffractive DIS as depicted in Figure 1.12 can be written as a five fold differential cross section depending on: $x_{I\!P}$, β, Q^2, M_Y and t. Since M_Y and t cannot be measured at present one must integrate over these variables obtaining a three fold differential

---

[5] η is defined as $\eta = -\frac{1}{2} \ln\left(\tan\frac{\theta}{2}\right)$

cross section which is then related to the diffractive structure function $F_2^{D(3)}$ introduced similarly to the inclusive proton structure function F_2 [57]:

$$\frac{d^3\sigma_{ep \longrightarrow eXY}}{dx d\beta dQ^2} = \frac{4\pi\alpha_{em}^2}{\beta^2 Q^4}\left(1 - y + \frac{y^2}{2}\right)F_2^{D(3)}. \tag{1.26}$$

Following the idea of Ingelmann and Schlein [49] the virtual photon which is emitted by the incoming electron can probe the structure of the Pomeron with different spatial resolution according to its virtuality Q^2. As factorisation was proven to hold for this process [56] the differential cross section can be analysed in terms of a hard scattering amplitude and parton density functions similarly to inclusive DIS. The structure function $F_2^D(3)$ was further assumed to factorise into a Pomeron flux and a Pomeron structure function which then was analysed in terms of parton distributions for the Pomeron. The QCD analysis indicated a large gluon component [57] which is in line with the results from jet production in hadron–hadron interactions [51].
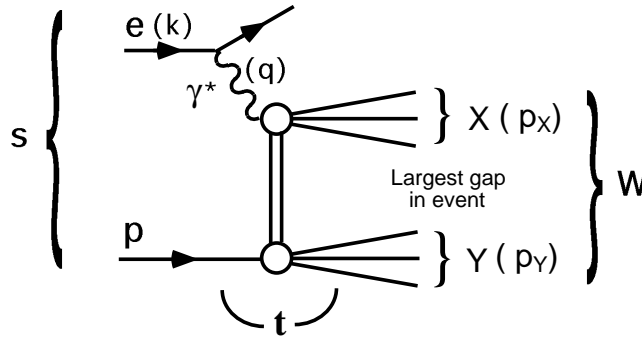

Figure 1.12: *The diagram for diffractive electroproduction at HERA. The photon emitted by the incoming electron interacts with the Pomeron and resolves its structure. In the hadronic final state two systems X and Y are separated by a gap in rapidity with no hadron production.*

The diffractive exchange can be studied in more detail by selecting diffractive events with specific properties of the hadronic final state X (see Figure 1.12). Events with two high energetic particle jets have been studied [58] and also events with charmed mesons in the final state have been analysed [59] where a hard scale is provided either by the transverse momentum of the jets or the mass of the charm quark to resolve the partonic structure of the Pomeron. The results of these analysis are consistent with the QCD analysis of the diffractive structure function.

Vector Meson Production

In order to test the diffractive exchange more exclusive events have been analysed where the hadronic system X consists only of a vector meson. Vector meson production ($ep \longrightarrow e\text{VM}p$) has been extensively studied at HERA for different types of vector mesons and also in the different kinematic regimes [60, 61, 62, 63, 64, 65, 66, 67, 68]. The data can be interpreted in terms of Regge theory in connection with the vector meson dominance model (VDM) [69, 70] as well as in the framework of perturbative QCD [71]. It therefore opens the possibility to study the

applicability of both approaches and allows a separation of effects calculable in perturbative QCD from soft physics observed in hadron–hadron interactions.

In the VDM the photon emitted by the incoming electron fluctuates into a vector meson which then scatters diffractively on the proton as depicted in Figure 1.13. In the VDM the production of vector mesons with the same quantum numbers as the photon is described (i.e. ρ, ω, ϕ, ...) since the Pomeron is characterised by the quantum numbers of the vacuum.
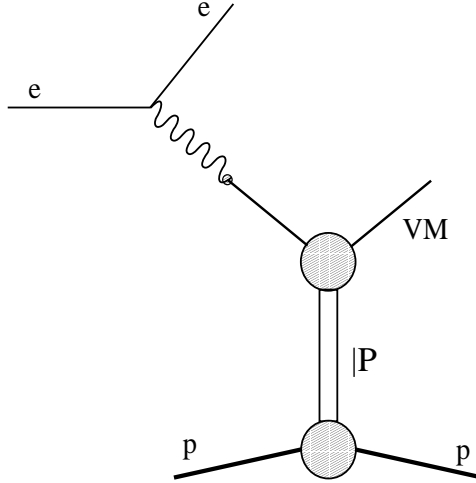

Figure 1.13: *Diagram for vector meson production in the vector meson dominance model in conjunction with Regge theory. The incoming electron emits a photon (real or virtual) which fluctuates into a hadronic system, the vector meson, which subsequently interacts with the proton by pomeron exchange. Only the production of vector mesons with the same quantum numbers as the photon are described within this model since the pomeron carries the quantum numbers of the vacuum.*

Figure 1.14 shows the measured cross section for vector meson production in photoproduction $\left(Q^2 \simeq 0\right)$ as a function of W, the photon–proton centre of mass energy. For the production of light vector mesons (ρ, ϕ and ω) the rise of the cross section at high W can be described as before in the framework of Regge theory by the exchange of the known Pomeron trajectory. The photoproduction of light vector mesons belongs therefore to the class of soft diffractive interactions. In the presence of a hard scale μ^2 as is the case for J/ψ production with $\mu^2 = m_c^2$, where the charm mass provides the hard scale, the rise of the cross section is steeper than predicted by Regge theory.

For light vector meson production a hard scale can be introduced by selecting events in the kinematic domain $Q^2 > \text{few GeV}^2$. Here a similar behaviour can be observed indicating, that the rise of the cross section for high values of W becomes steeper when Q^2 rises. This can be seen in Figure 1.15 where the slope δ of the cross section as function of W $\left(\sigma \sim W^\delta\right)$ is shown for different values of Q^2. For low Q^2 the rise of the cross section is comparable to the rise predicted by Regge theory. For large values of Q^2 the rise is significantly larger. These kind of interactions are called hard diffractive interactions and expected to be calculable within the framework of perturbative QCD since the presence of a hard scale ensures convergence of the perturbation series.

In summary this means that in the presence of a hard scale Regge theory is not able anymore
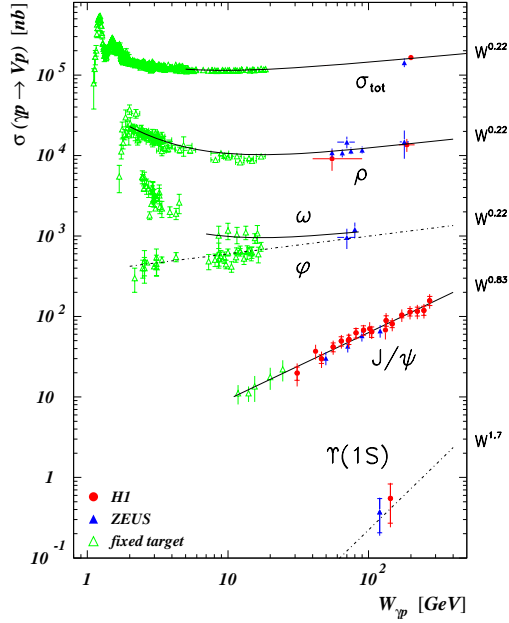
Figure 1.14: *Measured cross sections for the production of various types of vector mesons in photoproduction $\left(Q^2 \simeq 0\right)$ as a function of W, the photon proton centre of mass energy, is shown [60, 61, 62, 63, 64, 65, 66, 67, 68]. For light VM production the rise at large values of W is comparable to that predicted by pomeron exchange. For heavy vector meson production (i.e. J/ψ) the observed rise is steeper than for light vector mesons.*
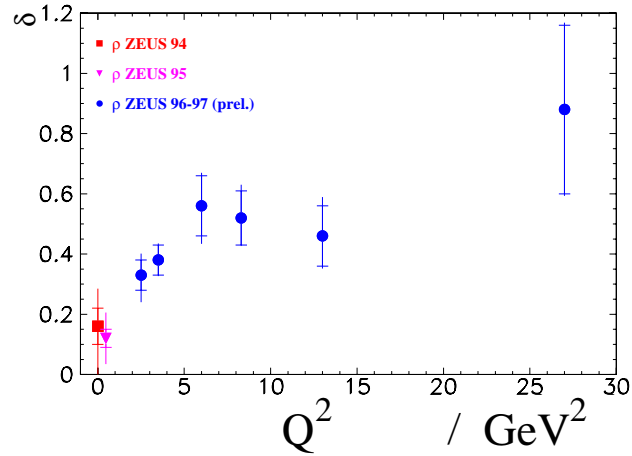
Figure 1.15: *The slope of the cross section δ as function of W $\left(\sigma \sim W^\delta\right)$ for diffractive production of ρ mesons is shown as function of the photon virtuality Q^2 [72]. For low values of Q^2 the fitted slope δ is comparable to the one predicted by pomeron exchange. For large values of Q^2 the slope is significantly larger.*

19

to describe diffractive processes. Due to the presence of a hard scale these kind of interactions are expected to be calculable in the framework of perturbative QCD. The investigation of these processes can be used to study the transition from soft to hard processes by varying the hard scale either by variation of the mass of the final vector meson, by the investigation of events in different regions of the photon virtuality Q^2 or by studying events with a large momentum transfer t at the proton vertex.

The Two Gluon Exchange Model

The two gluon exchange model [73, 74] was invented as model for the Pomeron and has been applied to the diffractive production of vector mesons. Figure 1.16 shows one of the diagrams to be calculated for this process. The virtual photon emitted by the incoming electron fluctuates in a $q\bar{q}$ system which then interacts with the proton by the exchange of two gluons. The quark–antiquark system subsequently recombines to the vector meson. The exchange of two gluons is the simplest way to establish the quantum numbers of the vacuum. The two quarks which build the final state vector meson have to be very close in phase space to avoid a break up before the VM has been formed. This condition is fulfilled in case of the two gluon exchange since the quark–antiquark pair stems from the photon and a small transverse momentum between the partons is possible. When exchanging two quarks which then couple directly to the incoming photon and the outgoing vector meson a large transverse momentum is enforced, due to energy momentum conservation, between the two partons leading to a suppression of this contribution for the reaction at low x.
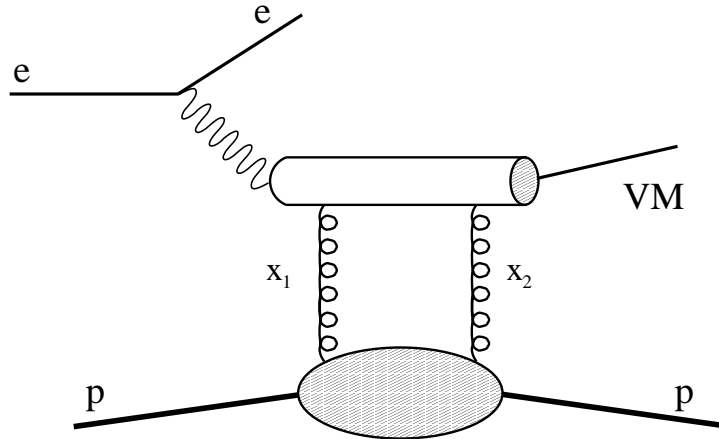
Figure 1.16: *Diagram for the production of vector mesons in the framework of QCD. The photon which is emitted by the incoming electron splits in a quark–antiquark pair which then interacts with the proton by the exchange of two gluons. After the interactions the quark–antiquark pair recombines to a vector meson. The diagram is fully calculable in perturbative QCD except the transition from the quark–antiquark pair to the final vector meson which has to be modelled.*

The factorisation theorem for this process has been proven [75] and states that the upper part of the diagram (see Figure 1.16) can be calculated in perturbative QCD and the non perturbative effects may be absorbed into parton density functions similar to ordinary DIS. In the common calculations for vector meson production the two gluons are approximated by the square of the gluon density as derived from DIS. These kind of calculations have been successfully applied to

predict the rise of the cross section for diffractive J/ψ production as function of W.

The approximation of the two gluon exchange by the square of the ordinary gluon density holds for low Q^2 and not too heavy vector mesons. In the domain of large Q^2 or for the production of heavy vector mesons (e.g. Υ) it is expected that an additional effect has to be taken into account when calculating cross sections. In case of photoproduction $\left(Q^2 \simeq 0\right)$ of heavy vector mesons the almost real photon interacting with the proton is transformed to a vector meson with the mass squared M_{VM}^2 (see Figure 1.16). Energy momentum conservation implies a longitudinal momentum transfer from the lower to the upper part of the diagram and hence $x_1 \neq x_2$ where x_1 and x_2 are the longitudinal momentum fractions of the two exchanged gluons. The difference in longitudinal momentum of the two participating partons is:

$$x_1 - x_2 = \frac{Q^2 + M_V^2/4}{W^2} \tag{1.27}$$

where M_V is the mass of the produced vector meson. In order to account for this effect the ordinary parton densities have been extended to the so called generalised parton distributions (GPD's) which become important for the calculations of cross sections for large values of Q^2, heavy vector mesons and for low values of W. In particular for the production of Υ mesons GPD's have to be used to explain the measured cross sections (see below).

1.3   Generalised Parton Distributions

Generalised Parton distributions (GPD's) [6] are functions which generalise and interpolate between different types of functions characterising the structure of the proton (nucleons). In particular the parton density functions as measured in DIS do not provide enough information needed for cross section predictions of certain reactions (e.g. vector meson production). Elastic form factors, unpolarised and polarised parton distributions can be derived from GPD's when integrating over or taking boundary values of these functions.

The concept of GPD's arose from three different theoretical studies[7]. Geyer et al. studied the relation between the Altarelli–Parisi evolution for parton distributions and the Brodsky–Lepage evolution for meson wave functions [77, 78, 79, 80]. The introduced interpolating functions are essentially what is nowadays called GPD's. Jain and Ralston studied hard processes involving hadron helicity flip in terms of an off–diagonal transition amplitude [81]. These can be used to derive elastic form factors. Finally Ji introduced off–forward parton distributions to describe the spin structure of the nucleon [82, 83]. He also proposed the measurement of Deeply Virtual Compton Scattering to extract these new distributions from the data [83].

Definition of GPD's

In this section the formal definition of GPD's is reviewed following the nomenclature of Ji [82, 83]. Additional definitions exist (e.g. [84]) which are basically equivalent and transformation formulae have been provided to switch between different nomenclatures.

---

[6]The term *Generalised Parton Distribution* is nowadays commonly used and comprises all names introduced in the past which originate from the different usage of these functions. Historically the terms: *off–diagonal*, *non–diagonal*, *off–forward* and *non–forward parton distribution* are used as well as *skewed parton distributions*.

[7]For a historical review see [76].

In section 1 it has been discussed that the standard parton distributions are obtained in the framework of Operator Product Expansion (OPE) from the squared proton wave function for all partonic configurations containing a parton with specified polarisation and longitudinal momentum x. After application of the factorisation theorem the hadronic matrix element $< p|O'O|p >$ can be identified with the parton density function which is interpreted as the probability for finding such a parton in the proton. Figure 1.17a) shows the graphical representation of this matrix element.

In contrast to this GPD's are defined as hadronic matrix elements of two unequal hadronic wave functions representing the incoming and outgoing nucleon (e.g. for VM production) $< p'|O|p >$ where $|p >$ denotes the wave function of the incoming proton and $|p' >$ represents the outgoing proton [85]. In Figure 1.17b) and c) the corresponding diagrams are shown.

In comparison to standard DIS two kinematic regimes exist, the so called DGLAP region (Figure 1.17b) and the ERBL region (Figure 1.17c). In the DGLAP region ($|x| > \xi$) the matrix element is interpreted as emission of a parton with longitudinal momentum $(x + \xi) \cdot p$ where p is the momentum of the incident proton and subsequent absorption of a parton with longitudinal momentum $(x - \xi) \cdot p$. For the ERBL region ($|x| < \xi$) which has no counterpart to standard DIS the matrix element is interpreted as emission of a di–parton system with longitudinal momenta $(x + \xi) \cdot p$ and $(-x + \xi) \cdot p$. In case of quarks the two parton system consists of a quark–antiquark pair.

The standard parton density functions are defined on the cross section level whereas the GPD's are functions defined on the amplitude level, i.e. when calculating cross sections (e.g. for vector meson production) the GPD's enter the calculation of the scattering amplitude which then is squared to achieve the cross section expression.

(a)   (b)   (c)
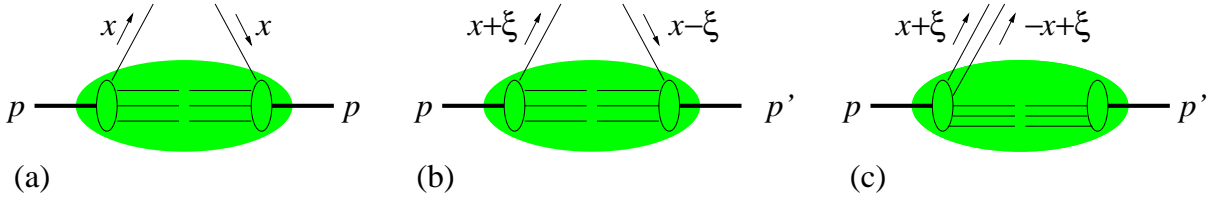
Figure 1.17: *Diagrams representing the hadronic matrix elements: a) for standard DIS and b) and c) for the generalised parton distribution. In contrast to parton densities in standard DIS the GPD's are defined by hadronic matrix elements of unequal hadronic wave functions. One distinguishes between the DGLAP b) and ERBL c) region.*

The generalised parton distributions can formally be defined by Fourier transforms of the hadronic matrix elements:

$$\int \frac{d\lambda}{2\pi} e^{i\lambda x} \langle P'|\overline{\psi}(-\lambda n)\gamma^\mu \psi(\lambda n)|P\rangle = H(x,\xi,t)\, \overline{u}(P')\gamma^\mu u(P)$$
$$+ E(x,\xi,t)\, \overline{u}(P')\frac{i\sigma^{\mu\nu}\Delta_\nu}{2M}u(P), \qquad (1.28)$$
$$\int \frac{d\lambda}{2\pi} e^{i\lambda x} \langle P'|\overline{\psi}(-\lambda n)\gamma^\mu \gamma_5 \psi(\lambda n)|P\rangle = \widetilde{H}(x,\xi,t)\, \overline{u}(P')\gamma^\mu \gamma_5 u(P)$$
$$+ \widetilde{E}(x,\xi,t)\, \overline{u}(P')\frac{\Delta^\mu \gamma_5}{2M}u(P) \qquad (1.29)$$

where $|P\rangle$ and $\langle P'|$ represent the quantum numbers of the incoming and outgoing proton respectively (including differences for the spin state). The operators $\overline{\psi}(-\lambda n)\gamma^\mu\psi(\lambda n)$ and $\overline{\psi}(-\lambda n)\gamma^\mu\gamma_5\psi(\lambda n)$ select the parton with certain properties from the hadronic wave functions. Δ^μ is defined as $\Delta^\mu = p'^\mu - p^\mu$ in the infinite momentum frame, $t = \Delta^2$, $u(P)$ and $\overline{u}(P')$ denote the Dirac spinors of the hadron. An examination of the helicity structure of the scattering amplitude shows that there are exactly four independent generalised parton distributions. The functions H, E, $\widetilde{H}$ and $\widetilde{E}$ are defined for the different quark flavours as well as for the gluon.

The reference system is chosen such that the initial and final nucleon have longitudinal momenta $(1+\xi)p^\mu$ and $(1-\xi)p^\mu$, and the outgoing and incoming partons carry the longitudinal momentum $(x+\xi)p^\mu$ and $(x-\xi)p^\mu$, respectively. Due to energy momentum conservation x and ξ are restricted to

$$0 \;\; < \;\; \xi < \frac{\sqrt{-t}}{\sqrt{M^2 - t/4}}, \tag{1.30}$$

$$-1 \;\; < \;\; x < 1. \tag{1.31}$$

The distributions H_q and E_q are summed over the quark helicities, whereas $\widetilde{H_q}$ and $\widetilde{E_q}$ involve the difference between right and left handed quarks and therefore contain information about the spin structure of the proton. The chiral-even distributions H and $\widetilde{H}$ survive in the forward limit, (i.e. $H(x,\xi,t) \neq 0$ and $E(x,\xi,t) \neq 0$ for $\xi = 0$ and $t = 0$) in which the nucleon helicity is conserved, while the chiral-odd distributions E and $\widetilde{E}$ allow for the possibility of a nucleon helicity flip. The change of the nucleon helicity in case of helicity conservation for the quarks is possible when orbital momentum is transferred by the two partons.

The evolution equations for the generalised parton distributions are modified DGLAP evolution equations in the DGLAP regime ($|x| > \xi$) whereas in the ERBL region ($|x| < \xi$) the Brodsky–Lepage evolution equations are used which originate from the study of evolution equations for meson wave functions[92, 93].

Sum rules and boundary conditions for GPD's

Several sum rules and boundary conditions for GPD's exist, thus drastically restricting the possibilities of models for GPD's.

The Nucleon Spin Structure

The spin of the nucleon can be decomposed in components which are carried by the quarks and by the gluons [82]:

$$\overrightarrow{J}_{\mathrm{N}} = \overrightarrow{J}_q + \overrightarrow{J}_g. \tag{1.32}$$

It can now be shown that:

$$J_{q,g} = \frac{1}{2}\Big(A_{q,g}(0) + B_{q,g}(0)\Big) \tag{1.33}$$

with

$$\int_{-1}^{1} dx\; x\Big(H(x,\xi,t) + E(x,\xi,t)\Big) = A(t) + B(t) \tag{1.34}$$

where the integral over the functions H and E has to be evaluated for the quark and for the gluon distributions. The ξ–dependence drops out when calculating the integral.

The Parton Density Functions

The generalised parton distributions contain information of both the ordinary forward parton distributions and electromagnetic nucleon form factors. In the limit $\Delta^\mu \longrightarrow 0$ one restores the ordinary quark and the quark helicity distributions $q(x)$ and $\Delta q(x)$ for $x > 0$:

$$H(x,0,0) = q(x), \quad \widetilde{H}(x,0,0) = \Delta q(x). \tag{1.35}$$

The Elastic Form Factors

The first moment of the generalised parton distributions is related to the nucleon form factors:

$$\int_{-1}^{1} dx H(x,\xi,t) = F_1(t), \tag{1.36}$$

$$\int_{-1}^{1} dx E(x,\xi,t) = F_2(t), \tag{1.37}$$

$$\int_{-1}^{1} dx \widetilde{H}(x,\xi,t) = G_A(t), \tag{1.38}$$

$$\int_{-1}^{1} dx \widetilde{E}(x,\xi,t) = G_P(t), \tag{1.39}$$

where F_1 and F_2 are the Dirac and Pauli form factors which can be related by linear combinations to the electric and magnetic form factors G_E and G_M. G_A and G_P represent the axial and pseudo-scalar form factors of the nucleon.

Models for GPD's

In this section the model for GPD's from Radyushkin based on Double Distributions will be outlined [80, 84, 86, 87]. Other approaches based on the MIT bag model [76], hadronic light cone wave functions [85] or the chiral quark soliton model [88, 89] are not discussed.

In addition to the boundary conditions discussed for GPD's they have to fulfil a polynomiality condition which is a non trivial consequence from Lorentz invariance. It states that the Mellin moments of the order N of the GPD should by polynomials of the maximal order $N + 1$:

$$\int_{-1}^{1} dx\ x^N\ H^q(x,\xi) = h_0^{q(N)} + h_2^{q(N)}\xi^2 + ... + h_{N+1}^{q(N)}\xi^{N+1}, \tag{1.40}$$

$$\int_{-1}^{1} dx\ x^N\ E^q(x,\xi) = e_0^{q(N)} + e_2^{q(N)}\xi^2 + ... + e_{N+1}^{q(N)}\xi^{N+1}. \tag{1.41}$$

This condition is satisfied when deriving GPD's from Double Distributions (DD) which are two dimensional functions $F(x',y')$ defined in a certain region of the x'–y' plane. The GPD is then calculated from the Double Distribution by the reduction formula:

$$H^q(x,\xi) = \int_{-1}^{1} dx' \int_{-1+|x'|}^{1-|x'|} dy'\ \delta(x' + \xi y' - x)\ F(x',y'). \tag{1.42}$$

In this ansatz the t–dependence has already been factorised out

$$H^q(x,\xi,t) = H^q(x,\xi) \cdot G(t) \tag{1.43}$$

which is a reasonable for HERA kinematics $\left(x_{\text{Bj}} < 10^{-2}\right)$ [83].

Using this ansatz the polynomiality condition is automatically fulfilled independent of the actual form of the double distribution $F\left(x', y'\right)$. In the model from Radyushkin the Double Distribution is further factorised in two functions:

$$F\left(x', y'\right) = \pi^q\left(x', y'\right) f^q\left(x'\right) \tag{1.44}$$

where $\pi^q\left(x', y'\right)$ is the profile function and $f^q\left(x'\right)$ is the ordinary parton distribution. This choice restaurates the ordinary parton density for $\xi = 0$ as required by equation 1.35. In order to satisfy this condition the profile function $\pi\left(x', y'\right)$, which is the only unknown quantity in this model, has to fulfil the following integral equation:

$$\int_{-1+|x'|}^{1-|x'|} \mathrm{d}y' \pi\left(x', y'\right) = 1. \tag{1.45}$$

The shape of the profile function then determines the effect of the GPD's on the cross section calculation.

Since the Double Distribution fulfil the polynomial condition except that the highest term in the polynomial is always 0 an additional term has been introduced by Polyakov and Weiss [90] which accounts for the highest term in the polynomial.

This ansatz is chosen for a certain scale Q_0^2. Once the GPD's are determined at $Q^2 = Q_0^2$ they can be evolved in the DGLAP region ($|x| > \xi$) similar to the DGLAP evolution equations with a kernel that depends on the longitudinal momentum transfer ξ and in the ERBL region ($|x| < \xi$) evolve according to equations similar to the ERBL evolution equations [92, 93] for meson distribution amplitudes.

GPD's in Practice

The first comparison of GPD based calculations with measurements has been done in an analysis by Martin, Ryskin and Teubner when they calculated the cross section for photoproduction of Υ mesons [91]. In Figure 1.18 the cross section measurements from H1 and ZEUS are compared to two different calculations, one based on the leading order expression and the other one including an enhancement factor originating from GPD's. The leading log QCD calculation leads to the simple formula:

$$\left.\frac{d\sigma}{dt}\left(\gamma p \to V p\right)\right|_{t=0} = \frac{\alpha_s^2 \Gamma_{ee}^V}{3\alpha M_V^5} 16\pi^3 \left[xg\left(x, \frac{M_V^2}{4}\right)\right]^2 \tag{1.46}$$

where Γ_{ee}^V is the partial width of the $V \to ee$ decay, α_s is the QCD coupling constant, $\alpha = 1/137$ is the QED coupling constant and $g(x, \mu^2)$ is the gluon density measured at $x = M_V^2/4W^2$ and the scale $\mu = m_Q \simeq M_V/2$. The LO prediction is well below the measurements although the statistical errors are still quite large. This calculation has been corrected for four different effects.

Relativistic corrections and NLO QCD corrections lead to a change of the predicted cross section by 7 % and 20 % respectively. Formula 1.46 accounts only for the imaginary part of the scattering amplitude. When restoring the real part of the QCD amplitude the cross section has to be enhanced by about 50 %. The largest correction originates from effects when using generalised parton distributions. It has been found to account for an enhancement of about a factor of 2. When comparing the measured cross section with the corrected calculation a better description of the data can be observed.
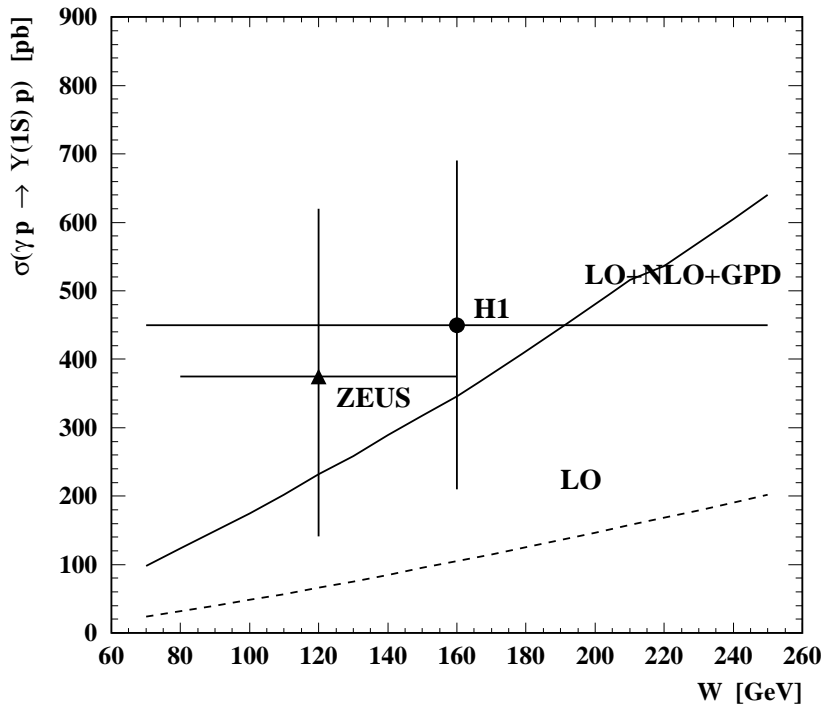
Figure 1.18: *The measurements for photoproduction of Υ mesons are compared to LO calculations (dashed line) and to a calculation including NLO effects as well as corrections due to the real part of the scattering amplitude and a correction due to the GPD's which account for the non forward kinematic situation* [91].

Chapter 2

Deeply Virtual Compton Scattering

2.1 Deeply Virtual Compton Scattering

Deeply Virtual Compton Scattering (DVCS) is defined as the elastic scattering of a virtual photon off a proton with a real photon in the final state. In electron–proton interactions the photon with a virtuality $Q^2 >$ few GeV^2 is emitted by the incoming electron leading to the reaction $ep \longrightarrow e\gamma p$ as depicted in Figure 2.1 a). This process is investigated to study the structure of the proton; in particular it provides access to the generalised parton distributions as introduced in Chapter 1.

It has been proven that in presence of a hard scale ($Q^2 \to \infty$) the DVCS scattering amplitude factorises in a hard scattering coefficient, calculable in perturbative QCD and a soft part which is absorbed in generalised parton distributions [94]. Figure 2.2 shows examples of the leading (a)
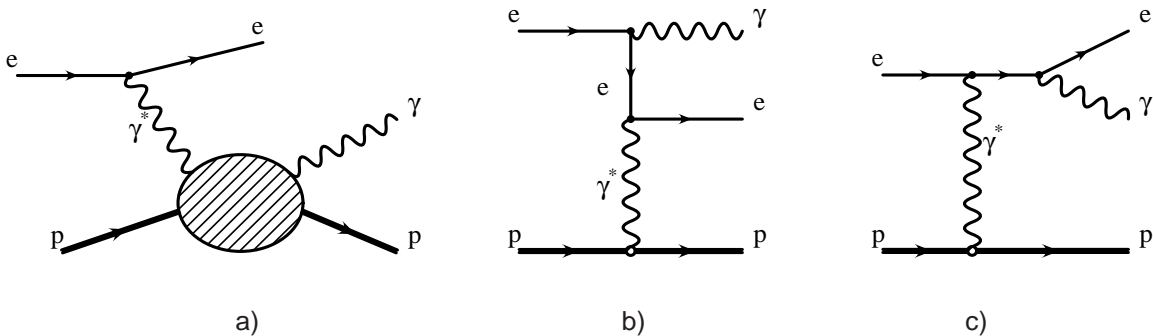
Figure 2.1: *The contributing diagrams for the reaction $ep \longrightarrow e\gamma p$: a) diagram for the Deeply Virtual Compton Scattering process; b) and c) diagrams for the Bethe–Heitler process.*

and next to leading order (b) diagrams of the DVCS process in a QCD approach. In the leading order process the virtual photon scatters off a quark originating from the proton. After emission of the real photon the quark is reabsorbed by the proton. In the NLO diagram the virtual photon interacts via a quark loop with two gluons from the proton. The real photon is also emitted from the quark loop. In contrast to DVCS the contribution of quark exchange to the vector

meson production process is suppressed w.r.t. the two–gluon exchange since the two quarks which form the vector meson have to be very close in phase space to form a stable meson. However this situation is suppressed for HERA kinematics (large W). For low energies (e.g. HERMES kinematics) the quark exchange also has to be taken into account when considering vector meson production.

DVCS calculations are expected to be more reliable than predictions for vector meson production due to the point–like coupling of the final state photon to the quark line. In vector meson production the VM wave function has to be modelled which describes the transition from the quark–antiquark system to the vector meson.
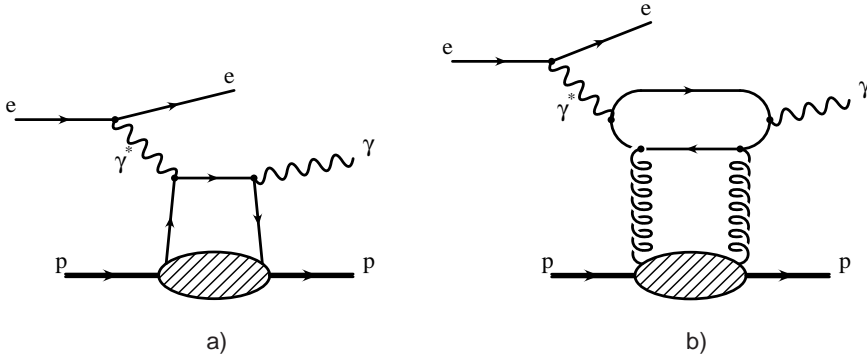

Figure 2.2: *Examples for diagrams of the DVCS process in leading and next to leading order QCD: a) The leading order diagram is the so called handbag diagram where the virtual photon interacts with a quark from a proton with subsequent emission of the real photon. b) In the next to leading order diagram the photon interacts with two gluons from the proton by a quark loop from which also the real photon is emitted.*

In addition to the DVCS process the Bethe–Heitler (BH) process where the real photon is emitted from the electron line contributes to the reaction $ep \longrightarrow e\gamma p$ (see Figure 2.1b) and c)). It leads to a direct contributions to the cross section and a contribution due to the interference of the two processes. The interference term provides the key to extract GPD's from $ep \longrightarrow e\gamma p$ data (see below).

It was found [95] that the DVCS and BH amplitude exhibit a different spin dependence which leads to a non vanishing ϕ dependence of the interference term, where ϕ is defined as the angle between the electron scattering plane and the photon production plane calculated in the virtual photon–proton centre of mass system (see Figure 2.3). The amplitude for the DVCS process shows a ϕ dependence according to:

$$\mathcal{A}_{DVCS} \sim e^{-i\lambda\phi}, \tag{2.1}$$

where λ is the helicity of the intermediate virtual photon γ^*. In contrast to this the BH process exhibits a ϕ dependence following:

$$\mathcal{A}_{BH} \sim e^{-2i\lambda'\phi}, \tag{2.2}$$

where λ' is the helicity of the final state photon. For the pure DVCS and BH contributions to the cross section the ϕ dependences cancel when going from the amplitude to the cross section expression, whereas for the interference term it does not. When evaluating the interference term

for unpolarised ep scattering it turns out that its contribution to the cross section is proportional to $\cos\phi$. This can be exploited by an asymmetry measurement in which one gets access to the real part of the QCD amplitude (see below). Moreover, when studying ep scattering with polarised beams, different ϕ dependencies appear for different beam polarisations which all can be used to access different terms of the scattering amplitude. Once the different contributions to the scattering amplitude are measured the generalised parton distributions can be determined.
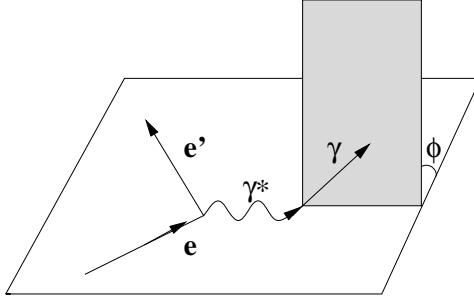

Figure 2.3: *The angle ϕ is defined as the angle between the scattering plane of the electron and the production plane of the real photon in the centre of mass system of the virtual photon and the incoming proton. The production plane of the real photon is defined by its vector and the virtual photon proton axis.*

2.2   Determination of GPD's from the DVCS Measurement

Although this analysis does not aim for a determination of the generalised parton distribution from the measurement, the method will be shortly outlined. As already discussed a measurement of the azimuthal angle asymmetry provides access to the real part of the QCD DVCS amplitude.

The azimuthal angle asymmetry is defined by the formula

$$A = \frac{\int_{-\pi/2}^{\pi/2}\mathrm{d}\phi\,\frac{\mathrm{d}\sigma^{ep\longrightarrow e\gamma p}}{\mathrm{d}\phi} - \int_{\pi/2}^{3\pi/2}\mathrm{d}\phi\,\frac{\mathrm{d}\sigma^{ep\longrightarrow e\gamma p}}{\mathrm{d}\phi}}{\int_{0}^{2\pi}\mathrm{d}\phi\,\frac{\mathrm{d}\sigma^{ep\longrightarrow e\gamma p}}{\mathrm{d}\phi}}, \tag{2.3}$$

where ϕ is the angle between the electron scattering plane and the photon production plane in the photon–proton centre of mass system. It is proportional to the real part of the DVCS amplitude which can be written in the factorised expression as

$$\mathrm{Re}\,\mathcal{A}\left(x, Q^2\right) = \int_{-1+x}^{1}\frac{\mathrm{d}x_1}{x_1}\mathrm{Re}\,C_i\left(x/x_1, Q^2\right)f_i\left(x_1, x, Q^2\right) \tag{2.4}$$

where $\mathrm{Re}\,C_i$ denotes the real part of the hard scattering coefficient and f_i are the generalised parton distributions for quarks and gluons. x_1 denotes the momentum of one of the exchanged partons and x denotes the Bjorken scaling variable.

In order to solve the deconvolution problem a method was proposed [96] based on the ansatz of a polynomial expansion for the GPD at a starting scale Q_0^2. The free parameters are obtained from fits to the data. When evolving the GPD to higher values of Q^2 the validity of this ansatz can be checked by comparing the results to data at these Q^2 values. Although this method is very convenient to apply, it has the disadvantage that the extraction of the GPD is model dependent.

2.3 Theoretical Predictions

The Model from Frankfurt, Freund and Strikman

Similar to ordinary DIS it is possible to calculate the Q^2 evolution for the scattering amplitude of Deeply Virtual Compton Scattering above a normalisation point $Q_0^2 \sim$ few GeV^2 [97]. Below this point the scattering amplitude is dominated by non–perturbative effects which prevents the usage of pQCD.

It was found ([98] and references therein) that the aligned jet model provides a reasonable description of the structure function F_2. When using the Gribov dispersion relation the ratio R of the imaginary parts for the DIS amplitude (in terms of the photon–proton amplitude) and the DVCS amplitude can be calculated as:

$$R = \frac{\mathrm{Im}\mathcal{A}\left(\gamma^* + p \longrightarrow \gamma^* + p\right)_{t=0}}{\mathrm{Im}\mathcal{A}\left(\gamma^* + p \longrightarrow \gamma + p\right)_{t=0}} \approx 0.5 \tag{2.5}$$

for $Q_0^2 \approx 2 - 3\,\mathrm{GeV}^2$. The DVCS process can now be calculated by a sum of soft and hard contributions where the soft contribution has been taken from this aligned jet model estimate and the hard contribution can be calculated in the framework of QCD evolution equations. This leads to the following expression for the evolution of the DVCS scattering amplitude[1]:

$$
\begin{aligned}
\mathrm{Im}\mathcal{A}\left(x, Q^2, Q_0^2\right) \;=\; & \mathrm{Im}\mathcal{A}\left(x, Q_0^2\right) \\
+ \; & 4\pi^2 \alpha_{em} \int_{Q_0^2}^{Q^2} \frac{\mathrm{d}Q'^2}{Q'^2} \int_x^1 \frac{\mathrm{d}x_1}{x_1} \left[P_{qg}\left(x/x_1, \Delta/x_1\right) g\left(x_1, x_2, Q'^2\right) \right. \\
& \left. + P_{qq}\left(x/x_1, \Delta/x_1\right) q\left(x_1, x_2, Q'^2\right) \right]
\end{aligned}
\tag{2.6}
$$

where P_{qg} and P_{qq} are the evolution kernels for generalised parton distributions. Using this relation the value for R has been estimated for the kinematic range accessible in this analysis as $R \approx 0.55$, almost independent on Q^2 and x [97]. The real part of the DVCS amplitude has been calculated using a dispersion relation:

$$\eta = \frac{\mathrm{Re}\mathcal{A}}{\mathrm{Im}\mathcal{A}} = \frac{\pi}{2} \frac{\mathrm{d}\ln\left(x\mathrm{Im}\mathcal{A}\right)}{\mathrm{d}\ln\frac{1}{x}}. \tag{2.7}$$

These relationes can now be used to calculate the complete cross section for the DVCS process. The imaginary part of the DIS amplitude $\mathrm{Im}\mathcal{A}\left(\gamma^* + p \longrightarrow \gamma^* + p\right)_{t=0}$ has been connected via the optical theorem to the DIS cross section which can be expressed in terms of the proton structure function F_2, such that F_2 enters the cross section expression (see below). The value of R accounts for the effect of the generalised parton densities.

The BH process is calculable within the framework of QED using the electro–magnetic form factors G_E and G_M. The complete differential cross section for the reaction $ep \longrightarrow e\gamma p$ is decomposed into the sum of three terms; the DVCS contribution, the BH term and the interference term.

$$\frac{d\sigma^{ep\to e\gamma p}}{dxdydtd\phi} = \frac{d\sigma^{\mathrm{DVCS}}}{dxdydtd\phi} + \frac{d\sigma^{\mathrm{BH}}}{dxdydtd\phi} + \frac{d\sigma^{\mathrm{Int}}}{dxdydtd\phi}, \tag{2.8}$$

---

[1]Note the different convention w.r.t. chapter 1.3.

$$\frac{d\sigma^{\mathrm{DVCS}}}{dxdydtd\phi} = \frac{\pi\alpha^3 s \left(1 + (1-y)^2\right)}{4R^2 Q^6} e^{-b|t|} F_2^2 \left(x, Q^2\right) \left(1 + \eta^2\right), \tag{2.9}$$

$$\frac{d\sigma^{\mathrm{BH}}}{dxdydtd\phi} = \frac{\alpha^3 s y^2 \left(1 + (1-y)^2\right)}{\pi|t|Q^4 (1-y)} \frac{G_E^2(t) + \frac{|t|}{4m_p^2} G_M^2(t)}{1 + \frac{|t|}{4m_p^2}}, \tag{2.10}$$

$$\frac{d\sigma^{\mathrm{Int}}}{dxdydtd\phi} = \pm \frac{\eta\alpha^3 s y \left(1 + (1-y)^2\right)}{2R Q^5 \sqrt{|t|(1-y)}} e^{-b|t|/2} F_2 \left(x, Q^2\right) \frac{G_E(t) + \frac{|t|}{4m_p^2} G_M(t)}{1 + \frac{|t|}{4m_p^2}} \cos\phi. \tag{2.11}$$

Note that the prediction for the DVCS process is valid at $t = t_{\mathrm{min}}$ where t is the momentum transfer at the proton vertex. The model assumes the t-dependence to follow an exponential function: $\frac{d\sigma}{dt} \sim e^{-b|t|}$ which is an ansatz that has been successfully applied to diffractive processes in the region of low $|t|$ (e.g. ρ vector meson production [60]). The interference term shows the $\cos\phi$ dependence which has been discussed already at the beginning of this chapter. The sign of the interference term depends on the polarity of the lepton beam.

Colour Dipole Models

General Properties of Colour Dipole Models

The Colour dipole model of diffraction [99] provides a simple unified picture of diffractive processes. It is able to reproduce the inclusive diffractive structure function $F_2^{D(3)}$ as well as exclusive reactions like vector meson production. Recently this model has been used to predict cross sections for the DVCS process. It is based on the assumption of a factorisation of the reaction in three subprocesses which are well separated in time. In the proton rest frame the incoming virtual photon fluctuates into a quark antiquark pair well before the interaction with the proton. The formation time for the dipole is $\tau \sim 1/M_p x$ which for HERA kinematics ($x \leq 0.01$) is much longer than the typical time scale for strong interactions $\tau \sim 1/m_\pi$. The subsequent formation of the hadronic final state (i.e. the photon in case of DVCS) from the scattered dipole is again much longer than the interaction time with the target. This justifies the basic assumption of the dipole model that the cross section for the interaction of the dipole is independent of how it is formed. The following factorisation formula for the scattering amplitude $\mathcal{A}$, also visualised in Figure 2.4, can be derived

$$\mathcal{A} \left(\gamma^* p \longrightarrow \gamma p\right) = \int \psi_{\gamma^*}^{in} \sigma_{\mathrm{d}} \psi_\gamma^{out}, \tag{2.12}$$

where the incoming and outgoing photon are denoted by the wave functions $\psi_{\gamma^*}^{in}$ and ψ_γ^{out}, respectively. It is integrated over all dipole sizes R and all momentum fractions z of the quark from the quark–antiquark dipole (see below). The cross section σ_{d} describes the interaction of the dipole with the proton. The colour dipole is assumed to be unchanged during the interaction. The different types of dipole models differ very strongly in their assumptions and the method used to derive the dipole cross section. In general the models make assumptions on the decomposition of dipole cross section; free parameters are derived from fits to the data. There exists no model which is able to derive the dipole cross section from first principles. Although the photon wave function is in principle calculable within perturbation theory (at least in leading order) some theories modify it to account for confinement effects for large dipoles.
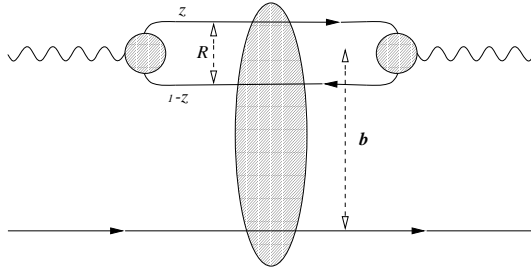
Figure 2.4: *In colour dipole models the incoming virtual photon fluctuates in a quark–antiquark system with radius R which then interacts with the incoming proton. The dipole leaves unchanged during the interaction and subsequently recombines to a real photon.*

The dipole models have been constructed such that they incorporate soft and hard contributions to the cross section. The transverse momentum k_T of the quark–antiquark system is given by

$$k_T^2 \simeq z(1-z)Q^2 + m_q^2 \tag{2.13}$$

where z determines the longitudinal momentum fraction carried by the quark and m_q is the quark mass. This can be related by the uncertainty principle to the radial distance R between the quark and the antiquark. Thus at low Q^2 the reaction is dominated by the interaction of large dipoles with the proton while small dipoles dominate at large Q^2.

The dipole models presented here are valid for $t = t_{\min}$. The cross section as a function of t is calculated by assuming an exponential t dependence

$$\frac{d\sigma}{dt} \sim e^{-b|t|}. \tag{2.14}$$

The Model from Donnachie and Dosch

In a model by Donnachie and Dosch [100] the dipole approach is coupled with the concept of soft and hard pomeron exchange. The scattering amplitude is written as

$$\mathcal{A}(s, t = 0) = 2\pi \int_0^1 dz \int dR\, R\, \rho_\gamma^\lambda(Q_1^2, Q_2^2, R, z)\, \sigma_{\mathrm{d}}(R) \tag{2.15}$$

where z is the longitudinal momentum fraction of the incident photon carried by the quark and R is the diameter of the quark-antiquark dipole. The dipole cross section $\sigma_{\mathrm{d}}(R)$ has been evaluated in a non–perturbative model and has two free parameters which have been determined by fits to $p\bar{p}$ and pp cross section data for which the nucleons have been decomposed in a quark-diquark system and thus can be treated as dipoles. The quark antiquark overlap density of photons $\rho_\gamma^\lambda(Q_1^2, Q_2^2, R, z)$, the product of the incoming and outgoing photon wave functions, for which Q_1^2 and Q_2^2 denotes the virtualities of the incoming and outgoing photon and λ is their helicity, has been calculated in lowest order perturbation theory.

The energy dependence is included by multiplying the cross section with the factor $(W/W_0)^{2\epsilon_{\mathrm{soft}}}$ where $1 + \epsilon_{soft}$ is the intercept of the pomeron trajectory with $\epsilon_{\mathrm{soft}} \sim 0.08$ and $W_0 = 20\,\mathrm{GeV}$. To account for the stronger energy dependence observed in reactions with a hard scale, the two pomeron approach [101] was included in the model such that small dipoles predominantly

interact by the exchange of the hard pomeron component whereas large dipoles interact via the soft pomeron component. Finally Donnachie and Dosch obtain the expression for the cross section at $t = t_{\min}$.

$$\frac{d\sigma}{dt}(Q^2, W, t = t_{min}) =$$
$$\frac{1}{16\pi}\left(r_{\text{soft}}(Q^2)(W/W_0)^{0.16} + r_{\text{hard}}(Q^2)(W/W_0)^{0.84}\right)^2 \times 311 \ \mu\text{b/GeV}^2 \qquad (2.16)$$

where $W_0 = 20$ GeV and

$$r_{\text{soft}}(Q^2) = \left(5.33 - 1.33 \cdot e^{(-4Q^2/Q_0^2)} + 5.37 \, Q^2/Q_0^2\right)^{-1},$$
$$r_{\text{hard}}(Q^2) = \left(49.42 - 7.65 \cdot e^{(-4Q^2/Q_0^2)} + 4.94 \, Q^2/Q_0^2\right)^{-1} \qquad (2.17)$$

with $Q_0^2 = 1$ GeV^2.

The Model of Forshaw, Kerley and Shaw

A model by Forshaw, Kerley and Shaw (FKS) [102, 103] assumes that the dipole cross section depends solely on the properties of the dipole proton system itself, independent of the photon virtuality Q^2, which means that it depends only on the photon–proton centre of mass energy W and on the size of the dipole R. The idea is to extract information on the dipole cross section by assuming a reasonable flexible form to fit the diffractive structure function and the total photon–proton cross section. The cross section is decomposed into two terms to account for soft and hard contributions

$$\sigma_{\text{d}}\left(W^2, R\right) = \sigma_{\text{d soft}}\left(W^2, R\right) + \sigma_{\text{d hard}}\left(W^2, R\right). \qquad (2.18)$$

The functions $\sigma_{\text{d soft}}\left(W^2, R\right)$ and $\sigma_{\text{d hard}}\left(W^2, R\right)$ have been chosen such that for small dipoles the hard contribution dominates while at low Q^2 $\sigma_{\text{d soft}}\left(W^2, R\right)$ contributes most.

The wave functions of the incoming and outgoing photon have been calculated in leading order perturbation theory and multiplied by an enhancement factor to increase contributions from large dipoles. This procedure is justified by the fact that for small $Q^2 < 4m_q^2$ the wavefunction becomes sensitive to the quark mass and that confinement effects are expected to become sizable. The quark mass has been chosen such that $m_q^2 = 0.08\,\text{GeV}^2$ which corresponds to the constituent quark mass.

The Model of McDermott, Frankfurt, Guzey and Strikman

In another model of McDermott, Frankfurt, Guzey and Strikman (MFGS) [102, 104] the dipole cross section $\sigma_{\text{d}}\left(Q^2, W, R\right)$ depends on both, the virtuality of the photon Q^2 and the photon proton centre of mass energy W. It is divided into three parts depending on the dipole size R. For small dipoles $R < R_C$ the cross section is directly related to the LO gluon distribution of the proton

$$\sigma_{\text{d}}\left(x, R < R_C\right) = \frac{\pi^2 R^2}{3}\alpha_s\left(\bar{Q}^2\right)xg\left(x', \bar{Q}^2\right), \qquad (2.19)$$

where x' and $\bar{Q}^2$ are functions of x and Q^2 depending on the dipole size R. The underlying model for this cross section is the two–gluon–exchange model discussed earlier[2]. The upper bound R_C depends on Q^2 and is $R_C = 0.246\,\mathrm{fm}$ for $Q^2 = 2.6\,\mathrm{GeV}^2$. For large dipoles above the pion radius $R > R_\pi = 0.65$ fm the cross section has been modelled by the function

$$\sigma_{\mathrm{d}}\left(R > R_\pi\right) = \sigma\left(\pi p\right) \frac{3R^2}{2R^2 + R_\pi} \left(\frac{x_0}{x}\right)^{0.08} \tag{2.20}$$

independent on Q^2 where $x_0 = 0.01$ has been chosen such that at $R = R_\pi$ σ_{d} matches the total pion proton cross section $\sigma\left(\pi p\right) = 24$ mb. In the intermediate region $R_C < R < R_\pi$ the dipole cross section is interpolated linearly.

This model focuses on the region of small dipoles and is hence only expected to be valid for $Q^2 > 1\ \mathrm{GeV}^2$ where the contribution from large dipoles is expected to be negligible. For the actual predictions of the cross section a generalised gluon distribution has been used.

Predictions Based on Generalised Parton Distributions

All models discussed above depend on different assumptions how hard and soft effects contribute to the DVCS cross section. Freund and McDermott presented [105, 106, 107] the first complete QCD calculation based on generalised parton densities. The used GPD is based on the model of Radyushkin (see chapter 1.3) which uses Double Distributions to derive them. The profile function $\pi^i\left(x', y'\right)$ has been chosen as:

$$\pi^i\left(x', y'\right) = \frac{3}{4} \frac{\left(1 - |x'|\right)^2 - y'^2}{\left(1 - |x'|\right)^3} \tag{2.21}$$

which leads in combination with the ordinary parton distributions (GRV [42] and MRST' [108] have been used) to predictions for the DVCS amplitude. It was calculated in leading order and next to leading order QCD by calculating the coefficient function and solving the evolution equations.

Depending on the actually used parton distribution large differences (factor 2–3) on the amplitude level can be observed which illustrates the high sensitivity of the cross section on effects due to the skewedness effects. These prediction do not yet exist on cross section level which would be a crucial test for GPD based models.

2.4   MC Programs

The final state of the reaction $ep \longrightarrow e\gamma p$ consists of an electron, a photon and a proton, where the electron and photon are detected with the H1 detector[3]. In order to extract the cross section from the measured event rate, MC simulations are performed using event generators as input. They generate the four vectors for the final state particles of the interactions which are then subjected to a detailed detector simulation. Six different MC programs have been used to study the signal as well as different background contributions.

---

[2]Note that the dipole cross section σ_d enters the amplitude (Equation 2.12). When calculating the cross section it depends quadratically on the dipole cross section and the gluon density as naively expected for the two gluon exchange model.

[3]For a detailed discussion of the analysis strategy see chapter 4.1.

TINTIN

The event generator TINTIN, developed in the framework of this thesis (for a detailed description see appendix A), is a program which generates the four vectors of the final state particles for the reaction $ep \longrightarrow e\gamma p$ where the kinematic variables are generated according to the predicted cross section by the calculations of Frankfurt, Freund and Strikman (see chapter 2.3). The program is able to generate events for the BH process, the DVCS process and the sum of the BH and DVCS process taking the interference term into account[4]. The most dominant QED radiative correction, the emission of a real photon from the incoming electron is implemented in the program.

COMPTON 2.0

The MC program COMPTON 2.0 [110, 111, 112] is used to generate events for the Bethe–Heitler process. It generates the elastic contribution as well as inelastic events. The program uses an exact calculation based on helicity amplitudes where the coupling to the proton is given by the electromagnetic form factors (G_E and G_M) for the elastic contributions. The inelastic contribution is divided into two regimes the resonance region ($M_X < 1.8\,\text{GeV}$) and the inelastic continuum ($M_X > 1.8\,\text{GeV}$) where M_X is the invariant mass of the hadronic final state. For the resonance region the three proton resonances $\Delta(1232)$, $N^*(1520)$ and $N^*(1688)$ have been taken into account and the corresponding cross sections are derived from measurements. In the region of the inelastic continuum the cross section has been taken from early F_2 measurements. As will be discussed in chapter 4 the cross section simulation of the inelastic Bethe–Heitler events has been modified according to a revised set of experimental data. The emission of a real photon from the initial electron which is expected to be the dominant higher order QED effect is implemented.

DIFFVM

The MC program DIFFVM [113] was designed to simulate the process of diffractive vector meson production $ep \longrightarrow e\,\text{VM}\,X$ where VM denotes the produced vector meson and X the hadronic final state, separated by a rapidity gap from the vector meson. The predictions of the program are based on the vector meson dominance model (VDM) and Regge theory as discussed in section 1.2. The virtual photon emitted by the incoming electron fluctuates into a vector meson which subsequently scatters off the proton. For the hadronic system X the resonant region as well as the inelastic continuum are taken into account. The program generates the four vectors of the final state particles including the decay products of the produced vector meson.

The DIFFVM program generates different vector meson channels, i.e. all vector mesons which have the same quantum numbers as the virtual photon (ω, ρ, ϕ ...). It can be used to generate elastic vector meson production as well as resonance production and the inelastic continuum.

---

[4]The free parameters have been set in the event generation to the following values: the t–slope parameter $b = 7\,\text{GeV}^{-2}$, the phase of the QCD amplitude, $\eta_{\text{QCD}} = 1 - \frac{\pi}{2}\left(0.176 + 0.33\ln Q^2\right)$ [109] and the sensitivity to the skewedness of the parton densities $R = 0.55$ [97]. The proton structure function F_2 as extracted from the H1 data has been used [5].

GRAPE

The event generator GRAPE [114] is used to simulate the reaction $e^+p \longrightarrow e^+e^-e^+p$. The predicted cross section is based on a calculation of the full matrix element taking all contributing diagrams into account. In the kinematic range relevant for this analysis the cross section is dominated by the two photon process where the photon emitted by the incoming positron interacts with a photon emitted from the proton by the production of an electron positron pair. Using the GRAPE MC program it is again possible to generate the full final state for the elastic and the inelastic reaction.

DJANGO and HERWIG

The MC program DJANGO ([115] and references therein) is a standard DIS event generator which is used for the generation of inclusive deep inelastic scattering events. It is a combination of the programs LEPTO, HERACLES, ARIADNE and JETSET where the program LEPTO calculates the DIS Matrix element. It is interfaced to HERACLES for calculation of the QED radiative corrections. The program ARIADNE simulates the subsequent emission of partons with a large transverse momentum. The results of this program are then interfaced to JETSET which performs the simulation of the fragmention based on the Lund String model. The program produces the four vectors of all final state particles.

The HERWIG program [116] is also a standard DIS event generator similar to the DJANGO program. The basic difference between the two programs relevant for this analysis is the use of a different fragmentation scheme. In contrast to the Lund fragmentation scheme which is used in DJANGO the HERWIG program is based on the cluster fragmentation.

Chapter 3

HERA and H1

In this chapter the HERA[1] storage ring and the H1 experiment are introduced. After a brief description of the HERA machine, an overview of the H1 detector in its 1997 setup is given, concentrating on the components which were used for this analysis.
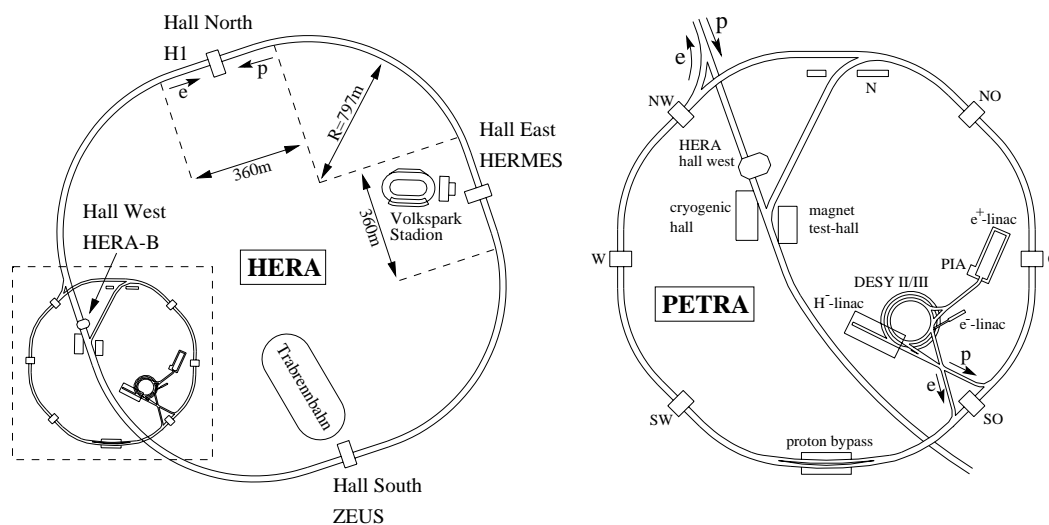
3.1 The Electron–Proton Collider HERA

Figure 3.1: *The electron proton collider HERA with its pre–accelerators.*

The HERA collider is located at the DESY[2] laboratory in Hamburg/Germany. It is the first electron–proton[3] collider ever built. The beam energies are 27.5 GeV for the electrons and 820 GeV for the protons respectively. This leads to an energy in the centre of mass system of

---

[1]**H**adron **E**lektron **R**ing **A**nlage
[2]**D**eutsches **E**lektronen **SY**nchrotron
[3]In the 1997 data taking period HERA accelerated positrons instead of electrons.

$\sqrt{s} \simeq 300 \, \text{GeV}$, which is more than 10 times higher than in formerly performed fixed target experiments. The two beam lines are located in the same tunnel with a circumference of $6.3 \, \text{km}$. The electron ring is equipped with dipole magnets with a field strength of $0.17 \, \text{T}$. The proton ring consists of superconducting dipole magnets with a field strength of $4.7 \, \text{T}$. The proton energy is limited by the field strength of the bending magnets while the maximum electron energy is determined by the power of the cavities which accelerate the electrons and compensate for the energy loss due to synchrotron radiation. The energy loss of protons due to synchrotron radiation can be neglected due to their high mass.

Figure 3.1 shows an overview of HERA and its pre–accelerators. The electrons are provided by a $500 \, \text{MeV}$ linear accelerator which are then ramped up in DESY II (to $7 \, \text{GeV}$) and PETRA (to $12 \, \text{GeV}$). After injection into HERA they are brought to their final beam energy. The protons are produced by passing H^- ions with an energy of $50 \, \text{MeV}$ through a stripping foil where the ions loose their two electrons. The protons are collected in bunches and accelerated in DESY III (to $7.5 \, \text{GeV}$) and in PETRA (to $40 \, \text{GeV}$) and afterwards injected into HERA and accelerated to their final beam energy. Both the electrons and the protons are stored in bunches of 10^{10} to 10^{11} particles which circulate in opposite direction in the HERA storage ring. The time between two bunch crossings is $96 \, \text{ns}$ which leads to a total number of 220 bunches for both the electron and the proton ring. They are filled such that typically 175 of these bunches collide and the additional bunches are filled either for the electrons, the protons or none of them. The lifetime of the proton beam is about $100 \, \text{hours}$, whereas the lifetime of the electron beam is about $10 \, \text{hours}$ which leads to a typical duration of $12 \, \text{hours}$ for a luminosity fill. By the year 2000 an electron current of $40 \, \text{mA}$ and a proton current of $90 \, \text{mA}$ was routiniously achieved leading to peak luminosity of $1.5 * 10^{31} \, \text{cm}^{-2}\text{s}^{-1}$ which corresponds to the design value.

The electron and the proton beam are brought to collisions at two interaction points. Around these the experiments H1 and ZEUS are constructed and take data since 1992. There are two additional fixed target experiments built at the HERA collider. The HERMES detector is a spectrometer which takes data since 1995 and studies interactions of polarised electrons from the electron beam with a polarised gas target (H_2, D, He). The aim of this experiment is to study the spin structure of the proton and related processes. The HERA–B experiment was commissioned in 2000 and is a forward spectrometer which uses an internal wire target to produce interactions between protons from the Halo of the proton beam and nucleons of the target wire. The aim of this experiment is to study CP–violation in the system of neutral B–mesons. This experiment serves also as a charm factory, which opens the possibility to study QCD with heavy quarks at high energies.

Figure 3.2 shows the time structure of a typical proton bunch in the HERA storage ring [117]. A threefold structure is observed where the main bunch is accompanied by two so called satellite bunches $5 \, \text{ns}$ before and after the main peak which are typically a factor 10 to 100 smaller. The interval of $5 \, \text{ns}$ between the main and the satellite bunch originates from the properties of the high frequency system of the HERA accelerating units. The frequency of the accelerating system is $200 \, \text{MHz}$ leading to a stable point in the seperatrix each $5 \, \text{ns}$. The distribution of the proton bunches is very broad in the PETRA accelerating system. When transmitting them to the HERA ring about $7 \, \%$ of the protons do not enter the main bunch but one of the satellite bunches. In the present analysis one cannot distinguish whether the final state particles originate from an interaction of an electron with a proton from the main or the satellite bunch. Therefore the effect of satellite bunch interactions has to be taken into account when analysing the data.

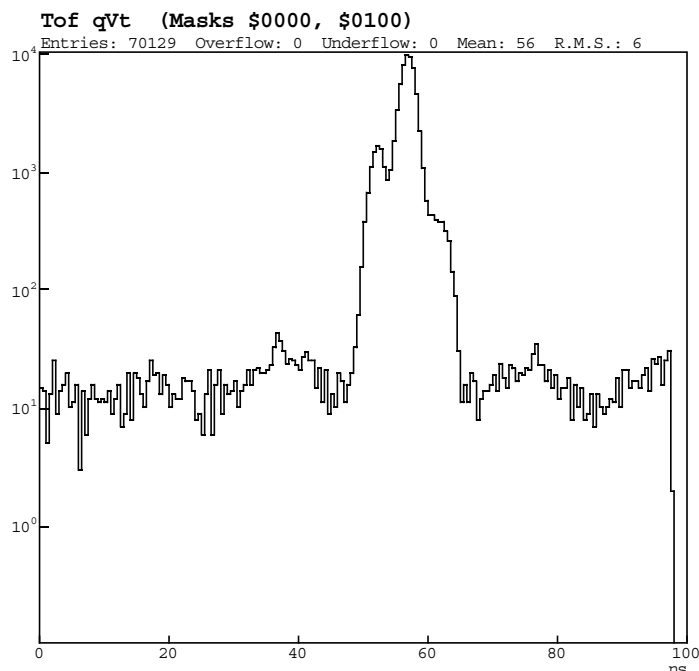Since September 2000 the data taking has been stopped and the HERA accelerator and the

Figure 3.2: *The bunch structure of protons in the HERA storage ring is subdivided into three parts: The main bunch is accompanied by two satellite bunches 5 ns before and after the main peak [117]. The sidebands originating from protons outside stable points in the separatrix are a factor 1000 smaller w.r.t. the main bunch.*

experiments undergo major upgrades. Superconducting quadrupole magnets are built and installed inside the H1 and ZEUS detectors, which enable a better focussing of the beams in the interaction region and therefore lead to a luminosity 4–5 times higher than before.

3.2 The H1 Experiment

The H1 detector [118] is a multi–purpose apparatus to study the final state particles from electron–proton scattering. It is located in the hall north of HERA. In order to study the wide range of the HERA physics program the detector has to satisfy several basic requirements. In neutral current events the kinematic variables are reconstructed from the properties of the scattered electron which requires a good calorimetric measurement for all scattering angles. The electron is scattered in the backward direction[4] for small values of the photon virtuality $Q^2 < 100 \, \text{GeV}^2$, whereas for larger values of Q^2 the electron tends to be scattered in the central or forward direction. Furthermore it is essential that the detector is hermetic in order to measure the momentum of all final state particles to determine the missing momentum which is needed to identify charged current interactions where the neutrino leaves the detector unseen.

Further instrumentation is used to measure muons and particles which leave the main detector

---

[4]The backward direction is defined w.r.t. the incoming proton beam.

through the beam pipe. The approximate size is $12 \times 10 \times 15\,\mathrm{m}$ and the weight is about 2800 tons.
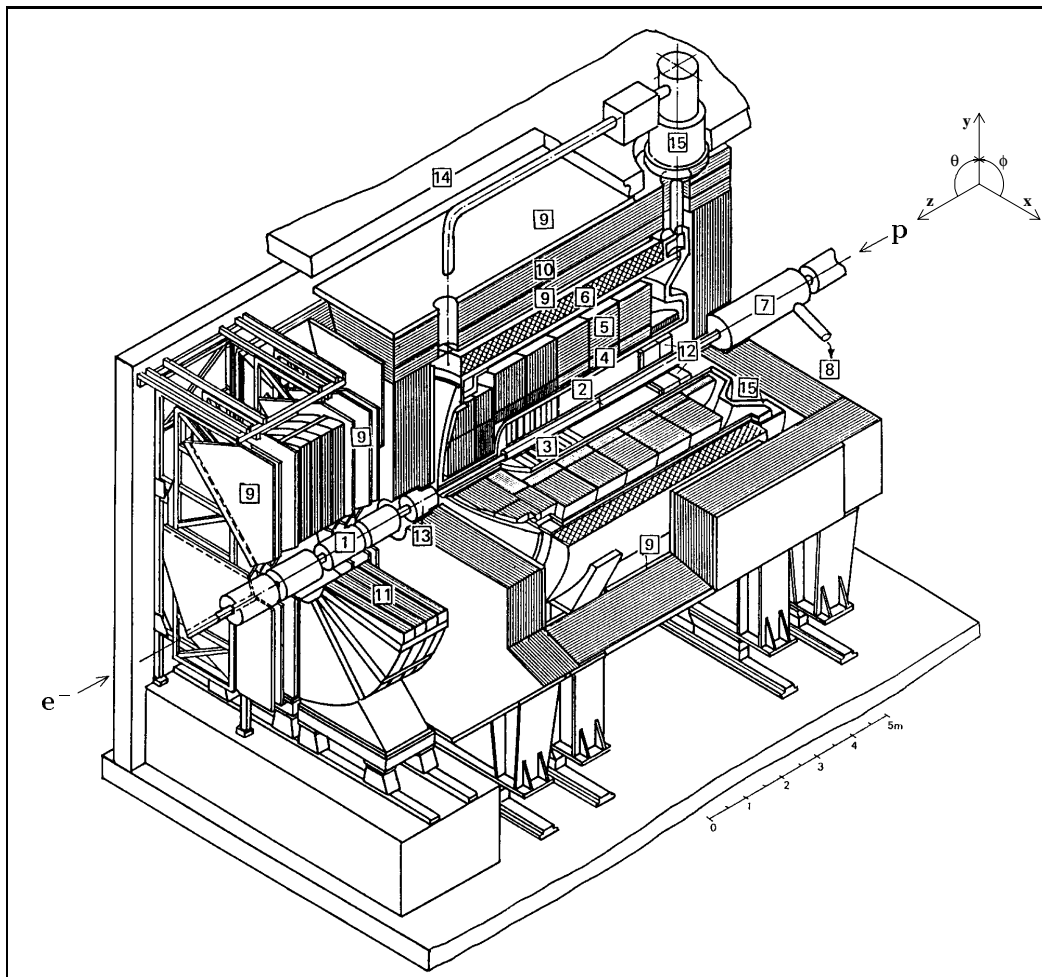
1	Beam pipe and beam magnets	9	Muon chambers
2	Central tracking device	10	Instrumented iron yoke
3	Forward tracking device	11	Forward muon toroid
4	Electromagnetic LAr calorimeter	12	Backw. calorimeter (SpaCal)
5	Hadronic LAr calorimeter	13	PLUG calorimeter
6	Superconducting coil (1.15 T)	14	Concrete shielding
7	Compensating magnet	15	Liquid argon cryostat
8	Helium supply for 7		

Figure 3.3: *The main detector of the H1 experiment*

As indicated in Figure 3.3 the electrons enter through the beam pipe 1 from the left and the protons from the right side. The interaction point is covered by silicon detectors in the central

and the backward region which are followed by the central $\boxed{2}$ and forward $\boxed{3}$ tracking detectors. These are surrounded by a large calorimeter system consisting of a Spaghetti calorimeter $\boxed{12}$ in the backward and a Liquid Argon calorimeter $\boxed{4}$ and $\boxed{5}$ in the central and forward region. Both calorimeters are divided into an electromagnetic and hadronic section. An additional plug calorimeter $\boxed{13}$ is installed in the forward direction close to the beam pipe. The LAr calorimeter is surrounded by a superconducting coil $\boxed{6}$ which provides a homogeneous magnetic field of 1.15 T along the tracking region. The iron return yoke $\boxed{10}$ of the magnet is instrumented with streamer tubes and is used to detect muons and to measure energy leakage from hadrons not fully contained in the LAr calorimeter. The forward muon detector $\boxed{11}$ is used to identify and measure the momentum of penetrating muons in the forward direction through the use of drift chambers and a toroidal magnet. In positive z–direction about 23 m from the interaction point in direction of the incoming protons a set of scintillating detectors is used to identify fragments from electron–proton collisions which leave the main detector through the beam pipe. At about 100 m a hadron calorimeter is placed to measure neutrons which can emerge from electron–proton collisions scattered under low angles. In negative z direction two electromagnetic calorimeters are situated to measure the final state particles from the Bremsstrahlung process which is used to determine the luminosity.

A right handed co–ordinate system is used with the origin at the centre of the central jet chamber. The positive z–direction is defined as being along the proton beam direction, x towards the centre of the HERA ring and y vertically upwards. The z axis corresponds to $\theta = 0$ and the positive x–axis to $\phi = 0$ when using polar co–ordinates. The detector components used in this analysis are now described in detail.

The Central Tracking System

The central tracking devices are part of the large tracking system (see Figure 3.4) of the H1 detector. It covers the angular range $15^o < \theta < 165^o$ with full azimuthal acceptance. Its main components are two large concentric drift chambers (CJC1 and CJC2) with a length of 2.2 m. CJC1 (CJC2) consists of 30 (60) cells with 24 (32) sense wires (Figure 3.4) parallel to the z axis. Its inner radius is 20.3 (53.0) cm and its outer radius 45.1 (84.4) cm respectively. The drift cells are inclined by about 30° with respect to the radial direction. The space point resolution in (r, ϕ) is 170 μm and 2.2 cm in z using a charge division method.

The resolution in z is much improved by the usage of z–chambers (CIZ and COZ) with wires perpendicular to the beam axis. They are located inside and outside of CJC1 at a radius of 18 cm and 47 cm, respectively. CIZ and COZ are divided into 15 and 24 drift cells with 4 sense wires per cell. The achieved resolution in z is 260 μm.

Charged particles are bent by the homogeneous magnetic field of 1.15 T provided by the super-conducting coil around the LAr calorimeter. The combination of CJC1 and CJC2 with the z–chambers leads to momentum resolution for the track measurement of $\sigma(p_T)/p_T < 0.01 \cdot p_T/\text{GeV}$

In addition to the drift chambers two multi–wire proportional chambers (CIP and COP) deliver fast signals used for trigger purposes.
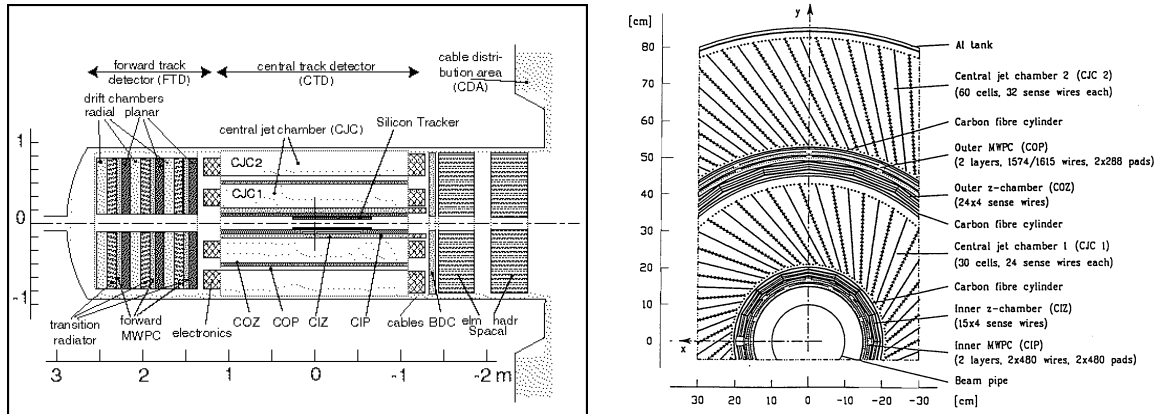
Figure 3.4: *The H1 tracking system: left) longitudinal view; right) transverse view.*

The LAr Calorimeter

The LAr calorimeter [119] (see Figure 3.5) provides energy measurement in the range $4^o < \theta < 154^o$ with full azimuthal coverage. In z–direction it is segmented into 8 wheels which each consist of 8 octants in ϕ. The six central wheels are divided into an electromagnetic and a hadronic section each, whereas the most forward wheel consists of two hadronic sections. The most backward wheel (BBE) consists only of an electromagnetic section and is also divided into 8 sections in ϕ. The LAr calorimeter is a sampling calorimeter which is located in a cryostat. The electromagnetic section consists of 2.4 mm thick lead absorber plates which are supplemented with high voltage and readout plates. The 2.35 mm gaps are filled with liquid Argon which serves as active material. Depending on the polar angle θ the depth of the electromagnetic section corresponds to $20 - 30$ radiation length. The hadronic section consists of 19 mm stainless steel absorber plates with a double gap of 2.4 mm filled with liquid Argon. This corresponds in total to 5 to 8 hadronic interaction lengths. The energy resolution for electromagnetic interacting particles, i.e. electrons and photons was determined from test beam measurements to be $\sigma(E)/E \simeq 11\%/\sqrt{E/\text{GeV}} \oplus 1\%$. The absolute energy scale for the measurement of high energetic electrons is known to a precision of 2 %.

The energy resolution for hadrons is $\sigma(E)/E \simeq 50\%/\sqrt{E/\text{GeV}} \oplus 2\%$. The LAr calorimeter is non compensating, i.e. the response to hadrons is about 30% smaller w.r.t. electrons with the same energy. This is corrected offline using a weighting technique. The main advantages of the liquid Argon technique are good stability, homogeneouty of the response, ease of calibration and fine granularity which opens the possibility to measure the scattering angles of photons with high precision. The total number of read–out channels is about 45000.

The Spacal and the BDC

The Spaghetti calorimeter, Spacal, [120] (see Figure 3.6) provides energy measurement in the backward region in the range $154° < \theta < 178°$ with full azimuthal coverage. It is a sampling calorimeter with lead as absorber material and scintillating fibres as active material. The Spacal is divided into an electromagnetic and a hadronic section with a lead to fibre ratio of $2.3 : 1$ and $3.4 : 1$, respectively. The electromagnetic section consists of cells of the size $40.5 \times 40.5 \times 225$ mm.
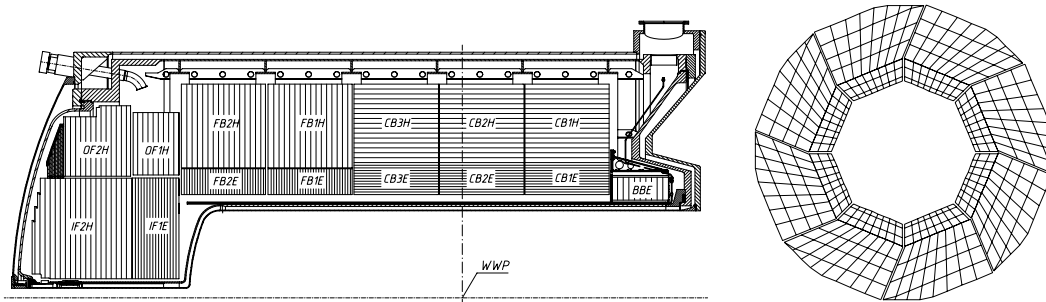
42

Figure 3.5: *The LAr calorimeter: left) side view: IF1E to BBE are the electromagnetic sections and IF2H to CB1H are the hadronic parts; right) transverse view.*

Each cell consists of grooved lead plates interspersed with scintillating fibres. Incident electrons and photons develop into an electromagnetic shower in the lead which subsequently causes the fibres to scintillate. The light is collected and read out by photomultiplier tubes. The cell size is adopted to the Molière radius of 25.5 mm. The length of the electromagnetic section corresponds to 28 radiation lengths which means that energy leakage of the detected electrons can be neglected. The energy resolution is determined to be $(7.1\pm0.2)\%/\sqrt{E/\mathrm{GeV}}\oplus(1.0\pm0.1)\%$. The absolute energy scale is known to a precision of 1.0% [121]. Due to the fine granularity a good spatial resolution of 3 mm is achieved and a good electron pion separation is ensured.
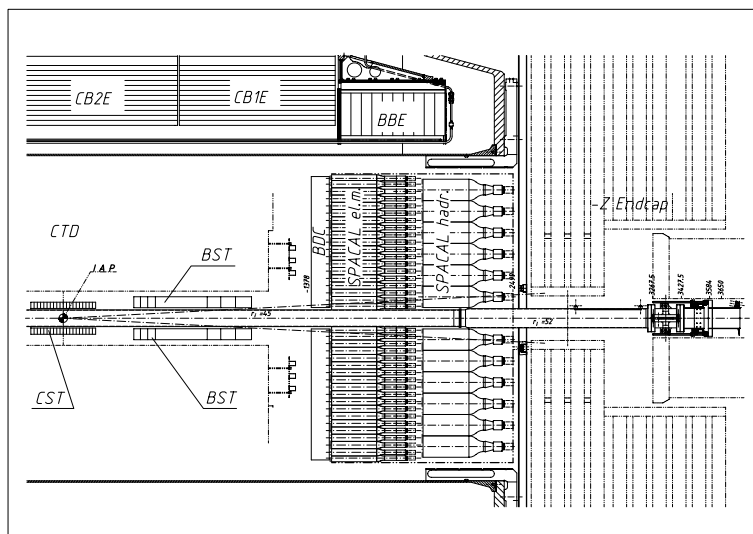

Figure 3.6: *A side view of the H1 detector focussing on the backward direction is shown.*

The Backward Drift Chamber (BDC) is mounted between the central tracking system and the Spacal. It provides a precise measurement of the polar angle of the scattered electron in the backward direction. The sense wires are perpendicular to the beam direction. The BDC consists of four double layers of 32 drift cells. Each layer is divided in 8 octants in ϕ. Each double layer is rotated with respect to the previous one by $\pi/16$ in ϕ which leads to an improved measurement at the boundaries of the octants and helps to resolve ambiguities in the ϕ measurement. In total the BDC contains 2048 signal channels.

43

The Forward Detectors

The aim of the present analysis is the measurement of a cross section for a process where the proton is scattered elastically. It leaves the main detector unseen, since it is typically scattered under small angles. Due to the small geometrical acceptance of the Proton Spectrometer [122] it cannot be used to tag the proton, therefore the forward muon detector (FMD) and the proton remnant tagger (PRT) are used to suppress events with proton dissociation. The remaining background from these kind of events is also determined using the FMD and PRT.
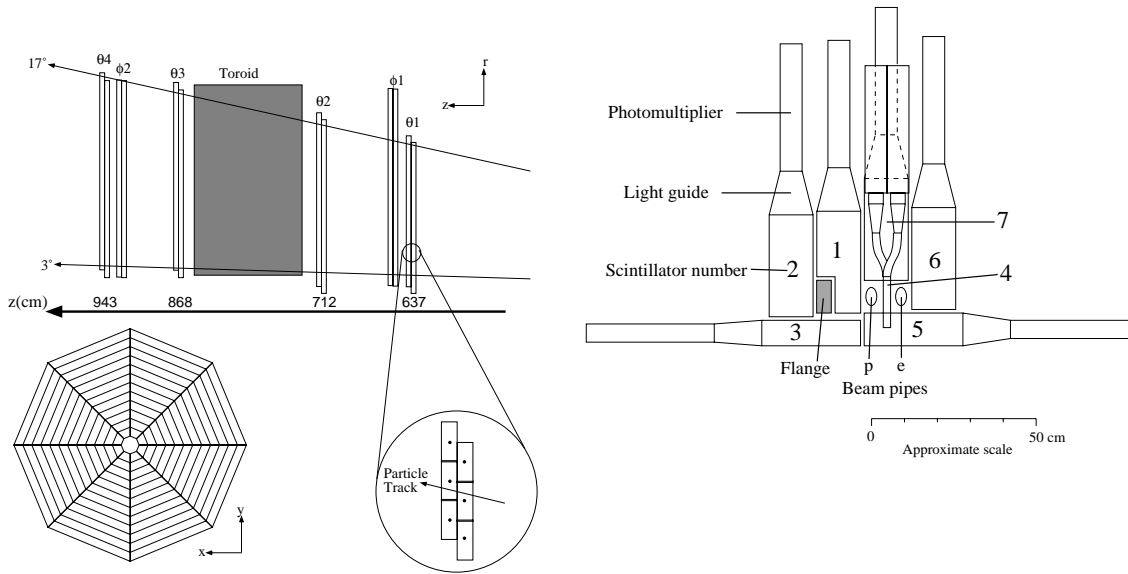
The Forward Muon Detector

Figure 3.7: *The forward detectors: left) sideview of the forward muon detector (FMD); right) front view of the proton remnant tagger (PRT) (see text for details)*
.

The FMD (see Figure 3.7) was designed to measure muons originating from heavy quark decays produced in the forward direction. The acceptance for the polar angle θ is $3° < \theta < 17°$ with full azimuthal coverage.

It consists of six double layers of drift chambers, four with wires strung in octants tangentially around the beam pipe to measure the polar angle θ and two double layers with wires strung radially to measure ϕ. Three double layers are placed at each side of a toroidal magnet designed to bend the muons to allow a measurement of the muon momentum. The FMD is able to measure muons in the range $5 < p_T < 100\,\mathrm{GeV}$.

Particles which are scattered under small angles into the forward region can hit collimators which are situated in the beam pipe to protect the main detector from synchrotron radiation. These secondary interactions produce a bunch of particles which then leaves signals in the FMD. The probability for elastically scattered protons to hit the collimators is very low. The geometrical

acceptance of the FMD corresponds to the region $1 < \eta < 2.5$. Due to the position of the collimators this acceptance is extended to the region $3.2 < \eta < 5.5$ [123]. Therefore signals in the FMD are a good signature for events where the proton does not scatter elastically.

The Proton Remnant Tagger

The PRT (see Figure 3.7) is located at $+24$ m in the forward direction inside the HERA tunnel. It consists of seven scintillators arranged around and between the electron and proton beam pipe. Each component consists of two scintillator sheets. The induced signals are passed through a light guide to photomultipliers. The PRT is sensitive to particles produced in the range $5 < \eta < 7$. It is as well as the FMD sensitive to particles which originate from secondary interaction of the hadrons emerging from proton dissociation events which extends the sensitivity for particles detection up to $\eta = 7.5$ [123].

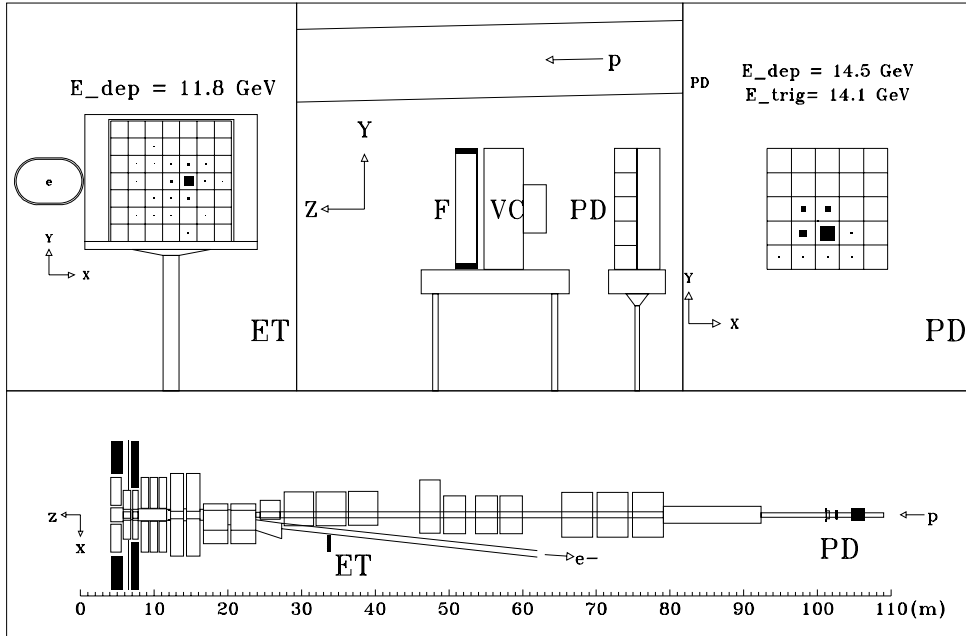**The Luminosity System and the Time of Flight System**

Figure 3.8: *The luminosity system consists of the electron tagger (ET) and the photon detector (PD) both located upstream w.r.t. the H1 detector. A typical Bethe–Heitler event is shown with signals in both detectors.*

An important ingredient to measure a cross section is the precise determination of the integrated luminosity. Normally the measurement of a process with a well known cross section is used to satisfy this demand. At HERA the Bethe–Heitler process $ep \longrightarrow e\gamma p$, where the electron and the photon are produced in the same direction as the incoming electron, is used for the luminosity measurement. It is fully calculable to high precision in QED.

Figure 3.8 shows the layout of the luminosity system. It consists of the electron tagger (ET) located at $z = -33.4$ m and the photon detector (PD) at $z = -102.9$ m which are two elec-

tromagnetic calorimeters. Both hodoscopes are crystal Cerenkov counters with high radiation resistance and good energy, spatial and time resolution. The scattered electrons from the Bethe–Heitler process are bent by a set of low-β quadrupole magnets before they leave the beam pipe at $z = -27.3$ m through an exit window and hit the electron tagger. The scattered photons are dominantly scattered under small angles. They leave the proton beam pipe undisturbed at $z = -92.3$ m where the beam pipe bends upwards; they then reach the photon detector. The PD is shielded from synchrotron radiation by a lead filter. A water Cerenkov counter is used to estimate the energy deposited by photons in the lead absorber. This is necessary to determine the energy of the scattered photon in the Bethe–Heitler process. The ET and the PD are mounted on movable platforms which are retracted during injection to protect the systems from radiation damage.

Two different methods exist to determine the luminosity:

- **Coincidence method:** The simultaneous measurement of an electron in the ET and a photon in the PD is required.

- **Photon method:** The luminosity is measured from the rate of detected photons alone.

The photon method is used for the final determination of the luminosity due to the smaller systematic uncertainties. The luminosity is determined using the formula:

$$L = \frac{N_{BH}^{ep}(E_\gamma > E_{min})}{\sigma_{BH}(E_\gamma > E_{min})}, \tag{3.1}$$

where $N_{BH}^{ep}(E_\gamma > E_{min})$ denotes the number of selected events with an energy E_γ larger than a minimal energy E_{min} measured by the photon detector. $\sigma_{BH}(E_\gamma > E_{min})$ denotes the cross section for the production of photons in that kinematic range. $N_{BH}^{ep}(E_\gamma > E_{min})$ has to be corrected for trigger efficiencies, acceptance of the photon detector which depends on the run dependent tilt of the beam and the pile up effect where more than one Bethe–Heitler process in a bunch crossing happens. The final systematic uncertainty is 1.5%.

The Time–of–Flight (ToF) system [117] rejects background from interactions of beam particles with residual atoms in the beam pipe or from interactions of beam particles with the beam pipe. At several positions scintillators are placed inside and outside the main detector. Based on the precisely known beam structure time windows are set to distinguish between background and useful physics events. The main part of the ToF system is the veto wall a double wall of scintillators situated at $-8.1 < z < -6.5$ m. In addition to the ToF system also the Spacal with a very good time resolution provides information on the interaction timing.

The Trigger and Data Acquisition

The bunch crossing rate inside the H1 detector is 10.4 MHz whereas the physics rate is only about 10 Hz. Since it is technically impossible to readout the whole detector information for each bunch crossing a three level trigger system was designed to reduce subsequently the rate of triggered events such that the readout rate is reasonable small.

The trigger system consists of a chain of four trigger levels from which three are actually implemented.

- **The level 1** trigger consists of a hardwired trigger logic with 128 subtriggers. These are built by logical combinations from 128 trigger elements provided by the different detector subsystems. The L1 trigger is fully pipelined and thus dead time free. Its decision time is $2.3\,\mu$s. After a positive trigger decision at level 1 the pipelines are stopped and the trigger data are submitted to the level 2 trigger systems. Almost all subdetectors deliver a trigger signal. For this analysis a subtrigger is used (for details see below) which uses only information of the Spacal inclusive electron trigger and the Time–of–Flight system.

- **The level 2** trigger consists of two subsystems: a topological trigger [124, 125] and a trigger based on neural networks. Both systems use the combination of signals from the different detector subsystem. The topological trigger takes a decision on the basis of pattern recognition which is hardwired in the electronics. An electron is e.g. identified by the combination of a track and cluster which are found close to each other in the θ–ϕ plane. The data for the neural network trigger are preprocessed and subsequently used as input for fast processors on which beforehand trained neural networks are implemented. The decision time for this trigger level is $20\,\mu$s in which the detector is not able to take events. After a positive level 2 decision the readout of data starts. Each subsystem delivers their data via an optical fibre ring to the event builder which collects the data and submits it to the level 4 filter farm.

- **The level 4** trigger consists in a farm of processors on which event reconstruction is performed and subsequently decision algorithms decide whether an event is taken or not. Up to 40 events are processed asynchronously with a processing time of about $100\,$ms for each event. After the acceptance of an event the data are submitted to the DESY computer centre where they are written to tape.

The data taking is organised in so called luminosity runs which last for about 10 to 60 minutes. The duration time is chosen such that during the run, conditions do not change drastically. After injection of beams and the ramping to the final energies the trigger rates are typically quite high due to the high instantaneous luminosity. The instantaneous luminosity decreases throughout a single luminosity fill which leads to a drop of the trigger rate. Hence to cope optimally use of the provided luminosity, the trigger setup is divided in four phases. Directly after lumi tuning when the high voltage of the tracking devices is not yet switched on data are taken in phase 1. After the HV is on phase 2 starts where the trigger rate is still quite high necessitating prescaling of subtriggers with high rate. These subtriggers are typically triggers which are designed to trigger low Q^2 processes or triggers which suffer from beam related background conditions. With improving data taking conditions the phase is switched from 2 to 3 and 4 where in the latter none of the main physics triggers is prescaled.

The Subtrigger S3

The level 1 subtrigger S3 used in this analysis consists of a logical combination of the inclusive electron trigger (IET) and trigger elements provided by the Time of Flight system. The IET is based on an energy deposition in the Spacal with the aim of detecting electron candidates. This is achieved by a sliding window technique. In Figure 3.9 the cell structure of the Spacal is shown. A presum of four Spacal cells is calculated representing one trigger cell. Four trigger cells are then combined two one trigger tower which overlap such that each trigger cell contributes to four trigger towers. If the energy in one trigger tower exceeds a certain threshold the trigger bit is set.
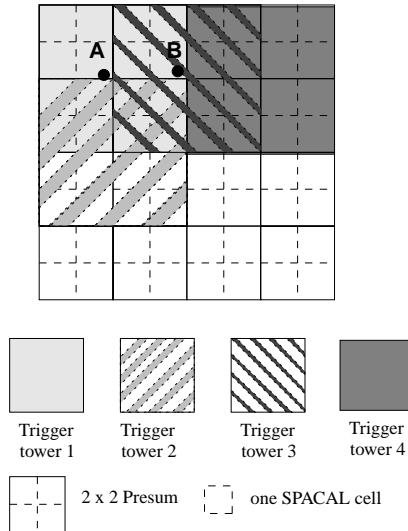
Figure 3.9: *Visualisation of the sliding window technique. The Spacal cells are combined to trigger cells which are further combined to overlapping trigger towers.*

Detector Simulation and Reconstruction

In order to measure a cross section, it is of paramount importance to understand the detector response in all aspects. A detailed simulation of the H1 detector has been implemented using the GEANT [126] simulation tool. Event generators based on Monte Carlo techniques are interfaced to the H1 detector simulation. The simulated events as well as the raw data read out from the detector are then subjected to the same reconstruction program which performs the identification of tracks in the tracking detectors as well as clustering of cells with energy deposition in the calorimeter.

Chapter 4

Event selection

4.1 Analysis Strategy

The aim of the analysis is to measure the elastic cross section for Deeply Virtual Compton Scattering (DVCS) for which the final state consists of a real photon, an electron and the scattered proton. Since the final state of the Bethe–Heitler (BH) process is identical the analysis strategy has been chosen such that a phase space region is selected in which the DVCS cross section is enhanced w.r.t. the BH process. The cross section for the BH process is largest if both particles are scattered into the backward direction (i.e. the direction of the incoming positron) of the H1 detector while topologies with one particle scattered into the backward and one into the forward direction are kinematically suppressed. This is different for DVCS which can be viewed as a two stage process (see Figure 2.1): First a virtual photon is emitted by the incoming positron which then scatters off the proton. Hence the scattered electron is most likely to be found in the backward direction because virtual photon emission is most probable for low values of the scaling variable y and low values of the photon virtuality Q^2, a property already known from ordinary DIS. In the second phase in which the virtual photon scatters off the proton, the outgoing photon is expected to be mainly scattered into the forward or central direction due to the large imbalance of the electron and proton beam energies leading to a photon–proton rest system fastly moving into $+z$ direction.

The scattered proton leaves the main detector undetected through the beam pipe. Therefore the events are selected by requiring an electron and a photon candidate. The rest of the detector must show no signal above noise level.

Two event samples are used in the analysis: the so called 'DVCS enriched sample' and a 'control sample' according to the following topologies:

- The **DVCS enriched sample** is selected by requiring the electron candidate in the backward direction, selecting events with an electromagnetic cluster in the Spacal. The photon candidate is identified by an electromagnetic cluster in the LAr calorimeter in the central or forward direction and the absence of a track in the central jet chamber (CJC). Both, the DVCS as well as the BH process contribute to this sample. A typical event of this class is shown in Figure 4.1.

- The **Control sample** is selected by requiring the electron candidate to be seen in the central or forward direction. Here the electron is identified by an electromagnetic energy

deposition in the LAr calorimeter and a reconstructed track in the CJC associated to the electromagnetic cluster. The photon candidate is to be found in the backward direction requiring an electromagnetic cluster in the Spacal. This sample is expected to be dominated by the BH process. The contribution of the DVCS process is highly suppressed since events of this topology would correspond to very high values of Q^2 which are kinematically suppressed. This suppression is expected to be smaller for BH events w.r.t. the DVCS process (see equation 2.9–2.10). A typical event of this sample is shown in Figure 4.2.
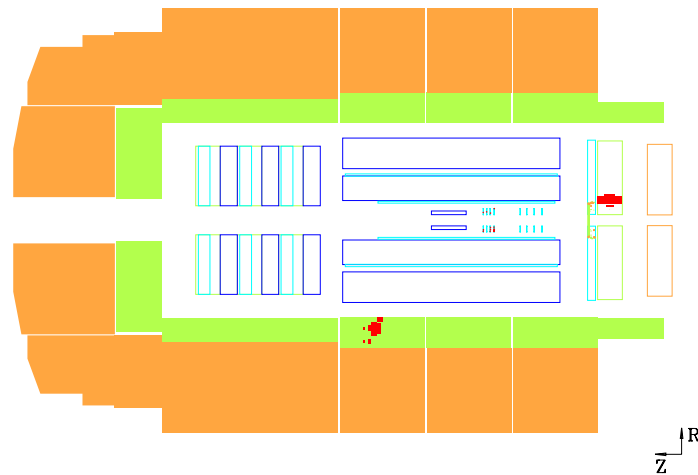

Figure 4.1: *An event of the* **DVCS enriched sample**. *It is identified by the presence of two electromagnetic clusters, one in the backward calorimeter Spacal and one in the LAr calorimeter. The photon candidate associated with the cluster in the LAr calorimeter is identified by the properties of the cluster and the absence of a matching track. The electron candidate in the Spacal must fulfill certain cluster properties. All subdetectors show no additional signal above noise level.*

4.2 Preselection

A preselection based on the detector status, luminosity and trigger conditions is performed to ensure a high quality of the data used in the analysis.

Run and HV Selection

The 1997 data taking period corresponds to the runs 176421 - 201519 with an integrated luminosity of $23.7\,\mathrm{pb}^{-1}$.
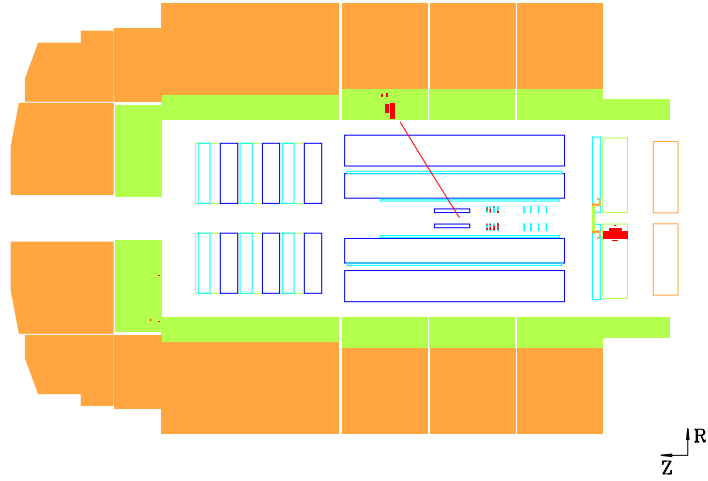
Figure 4.2: *An event of the* **control sample**. *The electron candidate is identified by a track in the CJC associated to an electromagnetic cluster in the LAr calorimeter. The photon candidate is identified by an electromagnetic cluster in the Spacal. All subdetectors show no additional signal above noise level.*

In the analysis only those runs are accepted which were taken in the trigger phase 2, 3 or 4 corresponding to no prescales for the subtrigger S3. The runs had to be flagged as 'good' or 'medium' implying all major components to be operational (CJC1-2, LAr calorimeter, Spacal and Luminosity system). In addition all detector components used in the analysis are required to be in operation. These systems are: The Time of Flight system (ToF), the Forward Muon Detector (FMD), the Proton Remnant Tagger (PRT) and the Forward tracker.

Several runs had to be excluded from the data analysis. Due to read out problems for the FMD only runs with a run number larger than 184257 could be used for the analysis. The runs 190123–193413 could not be used due to timing problems of the PRT. Runs with a run number larger than 198795 could not be used since the trigger setup changed and no appropriate trigger for DVCS events was available. In Table 4.1 further runs are listed which have been excluded due to problems with the offline data or the trigger. The final data sample taken for the analysis corresponds to an integrated luminosity of $\mathcal{L} = 8\,\mathrm{pb}^{-1}$.

Trigger

The events had to be triggered by the subtrigger S3 and pass the selection algorithm for inclusive diffractive events on level 4. There were no trigger requirement on the trigger levels 2 and 3.

The subtrigger S3 is based on a logical combination of trigger elements of the inclusive electron trigger for the Spacal and trigger elements provided by the Time of Flight system. Its aim is to trigger events with an electron scattered into the Spacal. The logical definition is:

run number	reason for exclusion
runrange: 184257 – 190080	
185665	offline data not available
186515	offline data not available
186752	offline data not available
187859	offline data not available
188142	offline data not available
188595	offline data not available
runrange: 193434 – 198795	
193433 – 193462	trigger malfunctioning
193502 – 193526	trigger malfunctioning
195678	offline data not available
195932 – 196376	trigger malfunctioning
197036	offline data corrupted

Table 4.1: *List of excluded runs due to problems with the offline data or the level 1 trigger.*

(SPCLe_IET_2.and.SPCLe_ToF_E_2).and. ((.not.SPCLh_AToF_E_1).and.(.not.BToF_BG)).and. ((.not.VETO_inner_BG).and.(.not.VETO_Outer_BG)).and. (FToF_IA.or.(.not.FToF_BG)).

The trigger element SPCLe_IET_2 is set for events with a locally concentrated energy deposition in the electromagnetic part of the Spacal above an energy of $6.5\,\mathrm{GeV}$. The total electromagnetic energy deposited in the Spacal is required to be larger than $12\,\mathrm{GeV}$ by the trigger element SPCLe_ToF_E_2 whereas no signal in the hadronic section of the Spacal is allowed in a time window outside the nominal ep interactions by the trigger element SPCLh_AToF_E_1. All further required trigger elements are provided by the Time of Flight system and summarised in Table 4.2.

trigger element	meaning
BToF_BG	Backward ToF Background
VETO_inner_BG	inner Veto wall Background
VETO_Outer_BG	outer Veto wall Background
FToF_IA	Forward ToF Interaction
FToF_BG	Forward ToF Background

Table 4.2: *List of trigger elements which are part of subtrigger S3. A trigger element is marked with the term 'Interaction' (IA) when the detector was triggered in a time window which corresponds to nominal ep collision time. It is marked with 'Background' (BG) when it was triggered outside this time window.*

The Level 4 selection algorithm used to select DVCS events was originally designed to flag inclusive diffractive DIS events with a low value of the photon virtuality Q^2. It requires an electron candidate to be found on the first trigger level; the diffractive selection is performed using the rapidity gap method which identifies events with no signal in the forward direction. It is based on three requirements: the absence of a signal in the PRT, the absence of a signal

above noise level in the FMD and no signal in the forward part of the LAr calorimeter

$$\sum_{\text{all layers}} \text{hits}_{\text{PRT}} = 0,$$

$$\sum_{\text{layer 1,2,3}} \text{hits}_{\text{FMD}} \leq 1,$$

$$\eta_{\max} < 3.2$$

where hits_{PRT} and hits_{FMD} denote the number of hits in the proton remnant tagger and the forward muon detector respectively. $\eta_{\max}$ is the rapidity value of the most forward energy deposition in the LAr calorimeter above a threshold of $0.5\,\text{GeV}$.

4.3   Final Selection Criteria

The final selection is based on the detection of two electromagnetic clusters, one in the Spacal and one in the LAr calorimeter which are subsequently identified as electron and photon according to the response of the tracking devices. In order to identify events with an elastically scattered proton there must be no additional signal registered by the detector above noise level. The following selection criteria have been applied:

- **Spacal selection**
  The DVCS process is expected to be dominated by so called kinematic peak events where the energy of the scattered electron is close to the initial electron beam energy. This property is already known from ordinary DIS events in the same kinematic region in x and Q^2. Thus events are selected with one electromagnetic cluster in the Spacal with an energy above $15\,\text{GeV}$ and a cluster radius $r_{cl} < 3.5\,\text{cm}$. The cluster radius is the energy weighted sum of the distance of all cells contributing to the cluster to the centre of gravity of the cluster [127]. It is a measure for the lateral extension of the electromagnetic shower. Electromagnetic interacting particles (i.e. electrons and photons) are found to produce smaller clusters than hadrons which makes the applied cut a powerful tool to suppress background initiated from hadrons. Some fiducial cuts on the impact position are applied to ensure that only events are selected where the electromagnetic cluster is correctly measured (see below).

- **LAr selection**
  Events are selected with a cluster in the LAr calorimeter with a transverse momentum $P_T > 1\,\text{GeV}$. The cluster is selected using the QESCAT algorithm which has been designed to separate clusters originating from electrons and photons from clusters initiated by hadrons. It requires that more than $90\,\%$ of the energy of the cluster is deposited in the electromagnetic section of the LAr calorimeter. Furthermore the cluster must be compact in the sense that it shows a small transverse dispersion and that $95\,\%$ of the energy are deposited in a core of not more than five cells for the calorimeter wheels CB1 and CB2 and not more than nine cells for the calorimeter wheels CB3, FB1 and FB2. Clusters have been selected with an impact position $z_{cl} > -150\,\text{cm}$. This cut is motivated by the analysis strategy to select only photon candidates in the central or forward region of the LAr calorimeter. The exact value has been chosen such that the centre of gravity of the cluster is not too close to the crack between the CB1 and the BBE (see Figure 3.5). Additional

fiducial cuts have been applied taking only well measured electromagnetic clusters into account (see below).

- **Track selection**
  The DVCS enriched sample and the control sample are classified according to the position of the photon and the electron candidate. The identification of these is performed using tracks measured with the central jet chamber.

  - In case of the **control sample** the electron is scattered into the central or forward direction and the photon is scattered in the backward direction. The electron is identified by a track which is reconstructed using the CJC and associated to the electromagnetic cluster in the LAr calorimeter. The electromagnetic cluster in the Spacal is then assumed to be the photon.

  - For the **DVCS enriched sample** the photon in the LAr calorimeter is identified by the absence of a track in the CJC. The electromagnetic cluster in the Spacal is then assumed to be the electron. A track for the electron candidate cannot be reconstructed due to the limited geometrical acceptance of the CJC; the electromagnetic clusters are dominantly found in the inner part of the Spacal which is not covered by the central jet chamber.

  If more than one track is reconstructed using the CJC the event is rejected.

  The reconstruction program provides two classes of tracks, one where the track is fitted to the interaction vertex and the other class for which tracks have been reconstructed but not fitted to the interaction vertex. For electrons it is likely that they emit a photon by the Bremsstrahlungs process when they cross the detector material (beam pipe, support structure, electronics, ...). If this happens the electron leaves its original direction which makes it impossible for the track reconstruction program to fit the track to the interaction vertex. It is important to take these kind of tracks into account since a misidentification of electrons as photons would spoil the measurement of the DVCS process. It has been found that the number of events in the control sample is increased by 3.5% when taking into account tracks which have not been fitted to the interaction vertex which is consistent with an independent analysis [128]. In addition the events of the DVCS enriched sample have been scanned with the event display program to cross check that the track veto condition has been correctly applied.

- **Elastic selection**
  Since the proton leaves the main detector through the beam pipe undetected and no further particles are produced, the detector should show no additional signal above noise level. To reduce background from other process (including non–elastic DVCS events) additional veto conditions have been applied.

  - Veto condition for the CJC
    If a track can be reconstructed with the CJC it has to be associated with the electromagnetic cluster in the Spacal or the LAr calorimeter. In case no association is possible or more than one reconstructed track is found the event is rejected.

  - Veto condition for the LAr calorimeter
    It is required that apart from the selected cluster in the LAr calorimeter no additional cluster with an energy $E_{cl} > 0.5\,\mathrm{GeV}$ is found. This cut has been chosen according to the noise distribution of the LAr calorimeter. A lower cut would lead to a rejection of

too many events leading to an increase of the statistical error for the measurement. The effect of this cut and the rejection of events due to noise has been taken into account in the MC simulations, in which the noise is not directly simulated but the simulated LAr calorimeter signals are overlayed with signals from randomly triggered data. By this procedure the LAr noise is correctly taken into account when applying the same cuts for data and MC simulation.

– Veto conditions for the forward detectors
The forward detectors, i.e. the FMD and PRT are used to suppress the contribution from inelastic events where the proton is excited into a higher state which subsequently decays as well as events from the inelastic continuum. For these kind of events it is likely that one or more of the final state particles hit the beam pipe or collimators originally designed to constrain the beam aperture and protect the detector from synchrotron radiation. This leads to a shower of secondary particles which eventually gives a signal in the FMD or PRT. At large $|t| > 1\,\mathrm{GeV}^2$ even the scattered proton could hit the scintillator pads of the PRT directly. It is required that no hit is observed in layer 0 and 1 of the PRT. All additional layers show almost no signal since they suffered from radiation damage and were thus not taken into account. For the FMD it was required that the sum of hit pairs in the first three layers is not larger than 1.

Figure 4.3 [130] shows the hit multiplicity distributions in the forward muon detector and the proton remnant tagger for inclusive DIS events. The data are compared to the sum of an inclusive DIS MC and a MC which generates diffractive events. For both the FMD and the PRT the data are well described by the MC simulation. The good description of the PRT response has been achieved by a decrease of its efficiency in the MC simulations of about $50\,\%$ as was observed for the 1997 data taking period due to radiation damage. Two independent methods have been developed to account for this effect which both led to the same results [130, 131]. The remaining differences for the FMD and PRT have been taken into account in the determination of the systematic error.
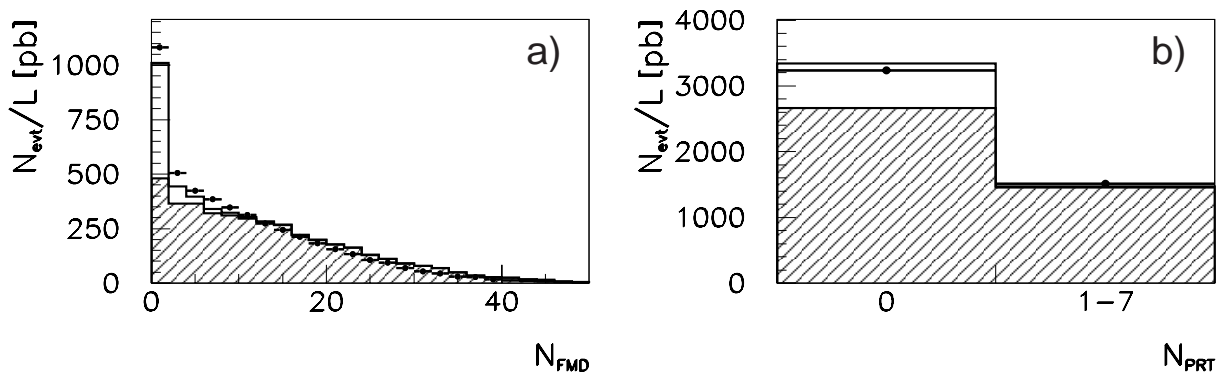

Figure 4.3: *Distributions of a) the number of hits in the forward muon detector and b) the proton remnant tagger (PRT). The data (black points) are compared to the sum of an inclusive DIS and a diffractive MC simulation (shaded and white histogram)* [130].

- **Fiducial Cuts**
Due to the malfunctioning of parts of the different subdetectors additional fiducial cuts

are applied to ensure that only fully functioning detector components contribute to the analysis. In Table 4.3 the fiducial cuts for the Spacal are listed. The inner module has to be excluded from the analysis since it is not part of the subtrigger S3 used in this analysis to select the events. Two additional regions are excluded due to malfunctioning. In the data taking period 1997 a wire of the CJC was broken resulting in a complete loss of parts of CJC1. To cope with this loss a cut on the position of the electromagnetic cluster in the LAr calorimeter has been applied. The excluded region is in the range $-2.4 < \phi_{cl} < -1.7$ rad.

Since the LAr calorimeter is divided into wheels which are itself subdivided into octants there are regions between the modules where no decent measurement is possible. Hence these regions are also excluded in a range of about 2° around the cracks. Furthermore due to malfunctioning of some cells in the LAr calorimeter the region $1.9 < \phi_{cl} < 3.8$ rad for $-50 < z_{cl} < 100$ cm is excluded as well.

x_{min}/cm	x_{max}/cm	y_{min}/cm	y_{max}/cm	reason
-17.0	10.0	-9.0	17.0	inner module
25.0	37.0	-38.0	-27.0	malfunctioning supermodule
-31.5	-25.5	33.1	39.0	malfunctioning cell

Table 4.3: *Fiducial Spacal cuts.*

4.4 Calibration of the LAr Calorimeter

Of major importance for the analysis is the LAr calorimeter which is used to measure the electron and photon energies and the scattering angle of the photon. The calibration of this calorimeter has been performed using test beam data [119]. It was improved by a calibration using a sample of high Q^2 neutral current events [128]. The mean electron energy of the events used for this calibration is about the electron beam energy of 27.5 GeV. Thus it is of paramount importance to check whether this calibration is also valid for lower energies down to 1 GeV as considered in this analysis. A check of the calibration has been performed using reconstructed J/ψ mesons which have been elastically produced in photoproduction events with subsequent decay into an electron–positron pair. The J/ψ mesons have been identified by events with two reconstructed tracks whose invariant mass is around the nominal J/ψ mass.

Figure 4.4a shows the reconstructed mass of all J/ψ candidates. The data are compared to simulated events which have been generated using the DIFFVM Monte Carlo program. The MC calculations are able to describe the mass spectrum reasonably well. The remaining differences can be attributed to events where one of the decay electrons from the J/ψ radiates a photon such that the reconstructed invariant mass is systematically shifted to smaller values and to the production of electron–pairs in photon–photon scattering not considered in the simulation. When taking these effects into account a better description of the data by the MC predictions is achieved [129]. Nevertheless the current accuracy is sufficient for this check of the calibration.

For the following study events have been selected with a reconstructed mass above $M_{e^+e^-} > 2.8$ GeV. In Figure 4.4b the momentum distribution for the tracks of the selected events as measured with the central tracking detectors is shown and again a good description of the data by the MC simulations can be observed. The same is true for Figure 4.4c where the energy for the electromagnetic clusters as measured with the LAr calorimeter is shown. The calibration

studies are completed by comparing the ratio of the cluster energy and the momentum of the track between data and MC (Figure 4.4d). Again good agreement is observed. For high energies the uncertainty on the energy scale is quoted to be 2%. In this analysis this uncertainty has been conservatively estimated to 4% as can be inferred from the deviations seen in Figures 4.4e and 4.4f where the cluster energies have been increased and, respectively, decreased by 4 %.

4.5 Reconstruction of the Event Kinematics

The kinematic variables of the reaction $ep \longrightarrow e\gamma p$ can be determined from the scattering angles and the energies of the final state electron and photon. Due to energy momentum conservation the determination of the kinematics is overconstrained which results in the possibility to use different reconstruction methods, i.e. the electron method where the kinematics is reconstructed from the scattered electron angle and energy, the double angle method where the kinematics is reconstructed from the scattering angles of the electron and the photon and the hadron method where it is determined from the scattering angle and energy of the final state photon. The double angle method was found to give the best resolution of both kinematic variables Q^2 and W which are calculated according to the following formulae:

$$Q^2 = 4E_0^2 \frac{\sin \theta_\gamma (1 + \cos \theta_e)}{\sin \theta_\gamma + \sin \theta_e - \sin (\theta_e + \theta_\gamma)}, \tag{4.1}$$

$$x = \frac{E_0}{E_p} \frac{\sin \theta_\gamma + \sin \theta_e + \sin (\theta_e + \theta_\gamma)}{\sin \theta_\gamma + \sin \theta_e - \sin (\theta_e + \theta_\gamma)}, \tag{4.2}$$

$$W^2 = \frac{Q^2}{x} (1 - x) \tag{4.3}$$

where E_0 and E_p denote the energies of the incident electron and proton beam, respectively. The polar scattering angles of the final state electron and photon are θ_e and θ_γ. Figure 4.5 shows the resolution of the kinematic variables Q^2 and W. For the control sample the reconstructed track in the CJC determines the interaction vertex given by the intersection of the reconstructed track with the beam line. In case of the DVCS enriched sample the interaction vertex cannot by reconstructed due to the absence of a track. Therefore the nominal vertex position, $z_{\text{vertex}} = 1.7 \, \text{cm}$, estimated with the control sample (see Section 4.6) , has been used to determine the scattering angles in combination with the reconstructed positions of the selected clusters in the LAr and Spacal calorimeter. The resolution for the reconstruction of the kinematic variable Q^2 is significantly degraded due to the unknown z–position of the event vertex. It changes from 3 % to 13 % whereas the resolution for W leaves almost unchanged at 5 %

When correcting the DVCS sample for the detector acceptance it is important to include contributions from events originating from ep–collisions which happened at the position ($z_{\text{vertex}} = 67.5 \, \text{cm}$) where electrons interact with the satellite bunch. For these kind of events the kinematic variables are systematically misreconstructed. Since a fraction of 3.5 % of the events originate from the forward satellite vertex this effect cannot be neglected and is thus accounted when calculating the acceptance correction (see chapter 5). The effect is strongest for the reconstruction of Q^2 as shown in Figure 4.5a. The resolution of the kinematic variables Q^2 and W is shown as determined using a MC simulation of events generated with the TINTIN program.

The variable t can be calculated in good approximation from the vectorial sum of the transverse momenta of the final state electron and photon:

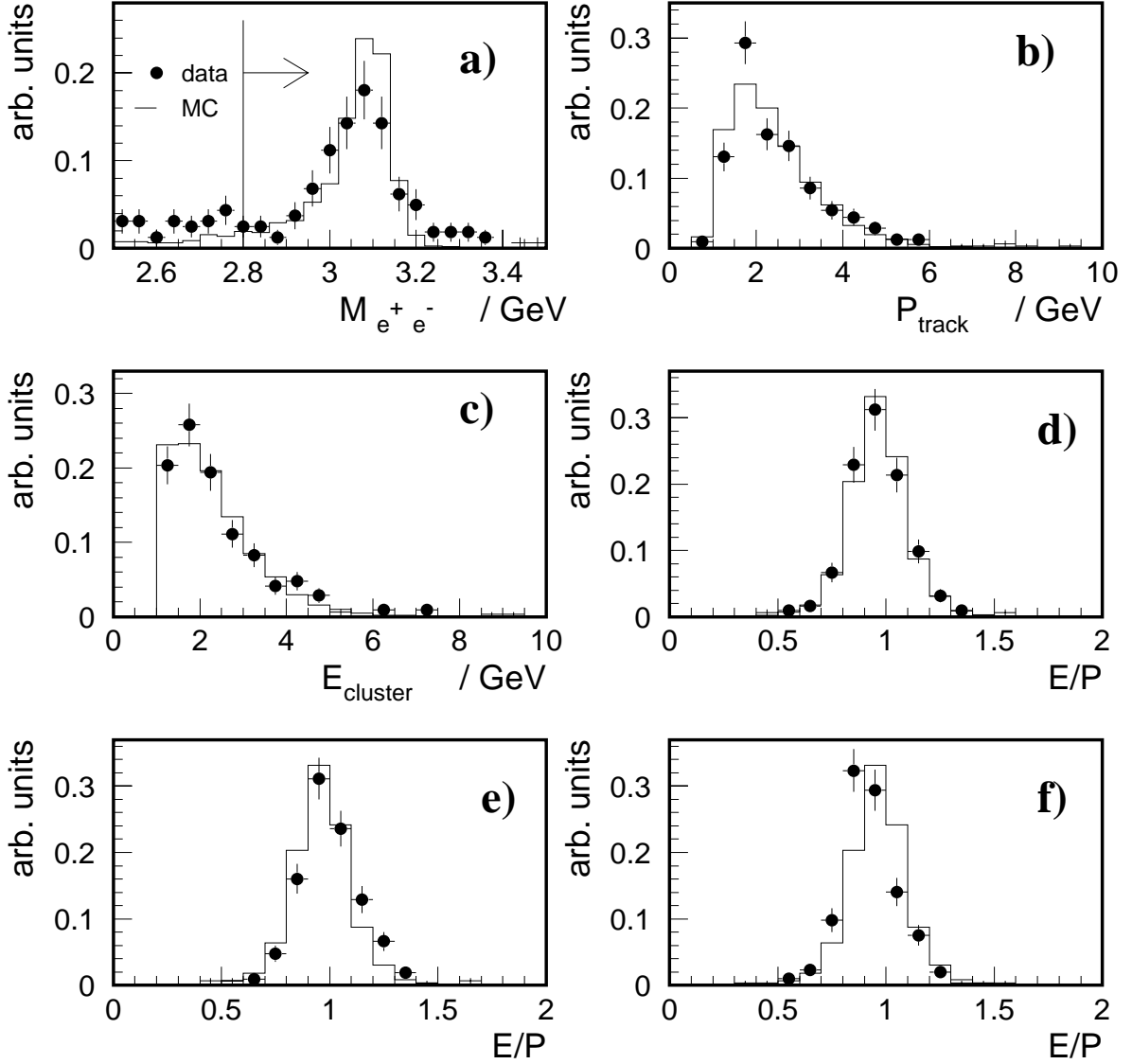$$t = -|\overrightarrow{P_{Te}} + \overrightarrow{P_{T\gamma}}|^2 \tag{4.4}$$

Figure 4.4: *The calibration of the LAr calorimeter has been checked using a sample of elastically produced J/ψ events in photoproduction. a) The invariant mass spectrum calculated from the two reconstructed tracks. The normalisation has been chosen such that for the invariant mass $M_{e^+e^-} > 2.8\,\text{GeV}$ the number of events in data and MC are equal. For the following distributions only events with $M_{e^+e^-} > 2.8\,\text{GeV}$ have been selected. b) Distribution of the momentum of the reconstructed tracks. c) Energy distribution of the reconstructed cluster associated to the track. d) Ratio of the energy of the cluster and the momentum of the track. e) Ratio of the energy of the cluster and the momentum of the track where the cluster energy has been increased by 4 % for the data. f) Ratio of the energy of the cluster and the momentum of the track where the cluster energy has been decreased by 4 % for the data.*
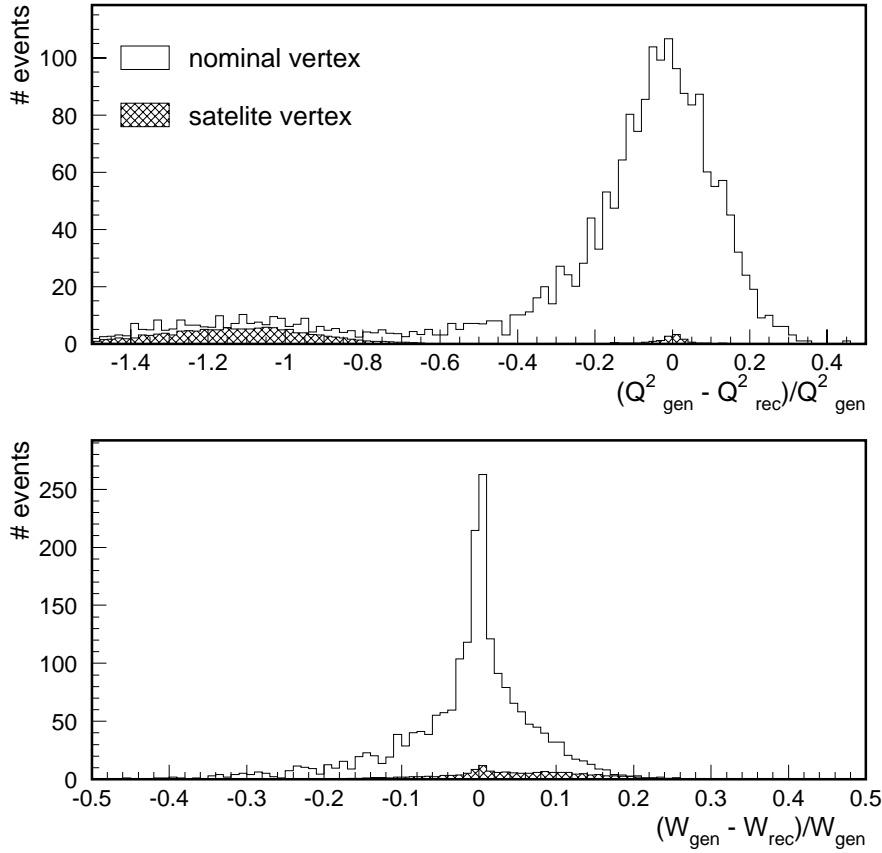
Figure 4.5: *Resolution of the kinematic variables a) Q^2 and b) W. The contribution from events originating from the main interaction vertex is shown by the white histogram. The shaded histogram shows the contribution for events which originate from the satellite vertex where the kinematic variables are systematically misreconstructed. The relative contribution of events from the satellite vertex is 3.5 %.*

where P_{Te} and $P_{T\gamma}$ are calculated from the azimuthal and polar scattering angles and the energies of the electron and photon.

For the calculation of the kinematic variables the data have been corrected for the beam tilt effect. The H1 coordinate system is defined by the Central Jet Chamber with the origin of the coordinate system in the centre of the CJC. The beam axis is however not perfectly aligned to the axis of the tracking device. Therefore the measured scattering angles are systematically misreconstructed which has to be corrected for in this analysis. The applied corrections originate from ordinary DIS events for which a large amount of events exists used to determine the exact beam axis. The influence on the measured cross section is about 5 %.

4.6 Control Sample

In addition to the already discussed selection criteria cuts are applied which restrict the kinematic domain to the region which is used for the measurement (see section 4.7). They restrict the data sample to the following kinematic domain: $2 < Q^2 < 20\,\mathrm{GeV}^2$, $30 < W < 120\,\mathrm{GeV}$ and $|t| < 1\,\mathrm{GeV}^2$. An additional cut on the variable $\sum E - P_z$ which is calculated from the electron and photon candidate and which characterises the longitudinal momentum conservation has been imposed: $\sum E - P_z > 45\,\mathrm{GeV}$. Its nominal value is equal to twice the electron beam energy $\sum E - P_z = 55\,\mathrm{GeV}$. This cut is imposed to minimise the effect of additional photon radiation from the incoming electron when extracting the DVCS cross section from the DVCS enriched sample.

When calculating the kinematic variables for the control sample the photon candidate has been treated as electron and the electron candidate has been treated as photon. This treatment leads to similar distributions for the scattering angles and energies of the final state particles in comparison to these distributions for the DVCS enriched sample. Therefore the control sample can be used to study directly the detector response for the region (i.e. angular range and energy domain) which is important for the DVCS measurement although the *true* kinematic distributions are completely different. In particular it can be tested whether the detector response is correctly described by the simulation.

The control sample consists of 338 events. It is expected to be dominated by the Bethe–Heitler process while the DVCS process does not contribute substantially. This can be understood by a simple numerical example. If the electron is scattered into the backward direction (e. g. $\theta_e = 177°$) and the photon is scattered into the central region of the detector (e. g. $\theta_\gamma = 90°$) as is the case for the enriched DVCS sample the photon virtuality Q^2 has the value $Q^2 = 1.7\,\mathrm{GeV}^2$ whereas in the inverse event topology ($\theta_e = 90°$, $\theta_\gamma = 177°$) Q^2 is $Q^2 = 63\,\mathrm{GeV}^2$. Since the DVCS cross section is expected to decrease faster with increasing Q^2 (see e.g. the FFS model in chapter 2) it is suppressed w.r.t. the Bethe–Heitler process.

Backgrounds to the Control Sample

It was found that two additional reactions can contribute to the same event topology as the control sample in a sizable way: The diffractive electro–production of ρ mesons and the dilepton production in two–photon interactions.

- Diffractive ρ meson production ($ep \longrightarrow e\rho p$, with $\rho \longrightarrow \pi^+\pi^-$) can contribute to the same event topology as the control sample when the final state electron is scattered into the backward direction and the positive charged decay pion is scattered into the central or forward direction, the negative charged pion and the proton leave the main detector undetected through the beam pipe. If the positive charged pion deposits its entire energy in the electromagnetic section of the LAr calorimeter it can in combination with its track be misidentified as an electron. The backward scattered electron seen in the Spacal is then mostly associated with the photon since the angular acceptance of the tracking devices is too small. It will therefore assumed to be a photon.

- Dilepton production in two photon events $e^+p \longrightarrow e^+e^-e^+p$ can contribute to the same event topology when one of the three final state leptons is detected in the backward direction, one lepton is scattered into the central part of the H1 detector while the third

lepton together with the proton leaves the main detector unseen. As for the diffractive ρ background the lepton measured by the Spacal will be interpreted as photon.

The two reactions have been studied using MC programs. Events of diffractive ρ electro–production have been generated by the DIFFVM MC generator while dilepton production has been simulated using the GRAPE program.

A possible background arising from events where an electron interacts with a nucleus of the residual gas in the beam pipe has been studied with a sample of events where only the electron bunches have been filled. No single event which satisfied the selection criteria has been found.

Figures 4.6–4.9 show different event distributions for which the data are compared to the sum of the MC predictions for the Bethe–Heitler process, diffractive ρ meson production and dilepton events. All distributions have been absolutely normalised. For the diffractive ρ production and the dilepton events only predictions for elastic scattering have been taken into account while for the Bethe–Heitler process also the contribution from the resonance region is included. As will be discussed in chapter 5 the applied cuts to select elastic events also select a small fraction of non–elastic events where the secondary particles from the dissociation of the hadronic system are not detected. Since the contributions from diffractive ρ production and dilepton events is very small the non–elastic component can be neglected. For the COMPTON 2.0 program which generates Bethe–Heitler events it was found [132] that the cross section for the resonance region was overestimated by about $50\,\%$. The number of events from the resonance region was therefore decreased by this amount.

Figure 4.6 shows the energy and angular distributions for the electron and the photon candidate. An overall good description of the data by the sum of the different MC prediction can be observed. The Figure 4.6a also shows that additional background from photoproduction events is not present in the event sample. For these kind of events where an almost real photon emitted by the incoming electron ($Q^2 \simeq 0$) interacts with the proton, a hadron of the final state could deposit energy in the Spacal which can be misidentified as photon and an additional hadron could fake an electron signal in the central part of the detector. This kind of events would lead to an energy distribution for the photon candidate rising steeply towards low energies which is not found in the data. The main part of the electron candidates is populated in the energy region from 1 to 5 GeV which motivates why the previously presented calibration study (Chapter 4.4) was necessary. The shapes of the angular distributions, especially the distribution of the azimuthal scattering angle ϕ is caused by the fiducial cuts. The dominating effect originates from the exclusion of the inner module in the Spacal.

Figure 4.7 shows distributions for the kinematic variables Q^2, x, t and W which have been reconstructed using the double angle method. Note that the usual interpretation for these variables cannot be applied due to the method used to calculate them (i.e. exchange of photon and electron candidate). An overall good description of these variables is observed. For the region of low Q^2 values a discrepancy can be observed which is however covered by the statistical error. Due to the small number of events in the DVCS enriched sample the statistical error is increased w.r.t. the control sample which justifies that the cross section measurement can also be performed at low Q^2.

Figure 4.8 shows the distributions for the Coplanarity and the variable $\sum E - P_z$. The Coplanarity is the difference of the azimuthal scattering angles of the final state electron and photon measured in the laboraty system. This distribution is governed by the dependence of the cross section as function of the momentum transfer t to the proton. The transferred momentum to
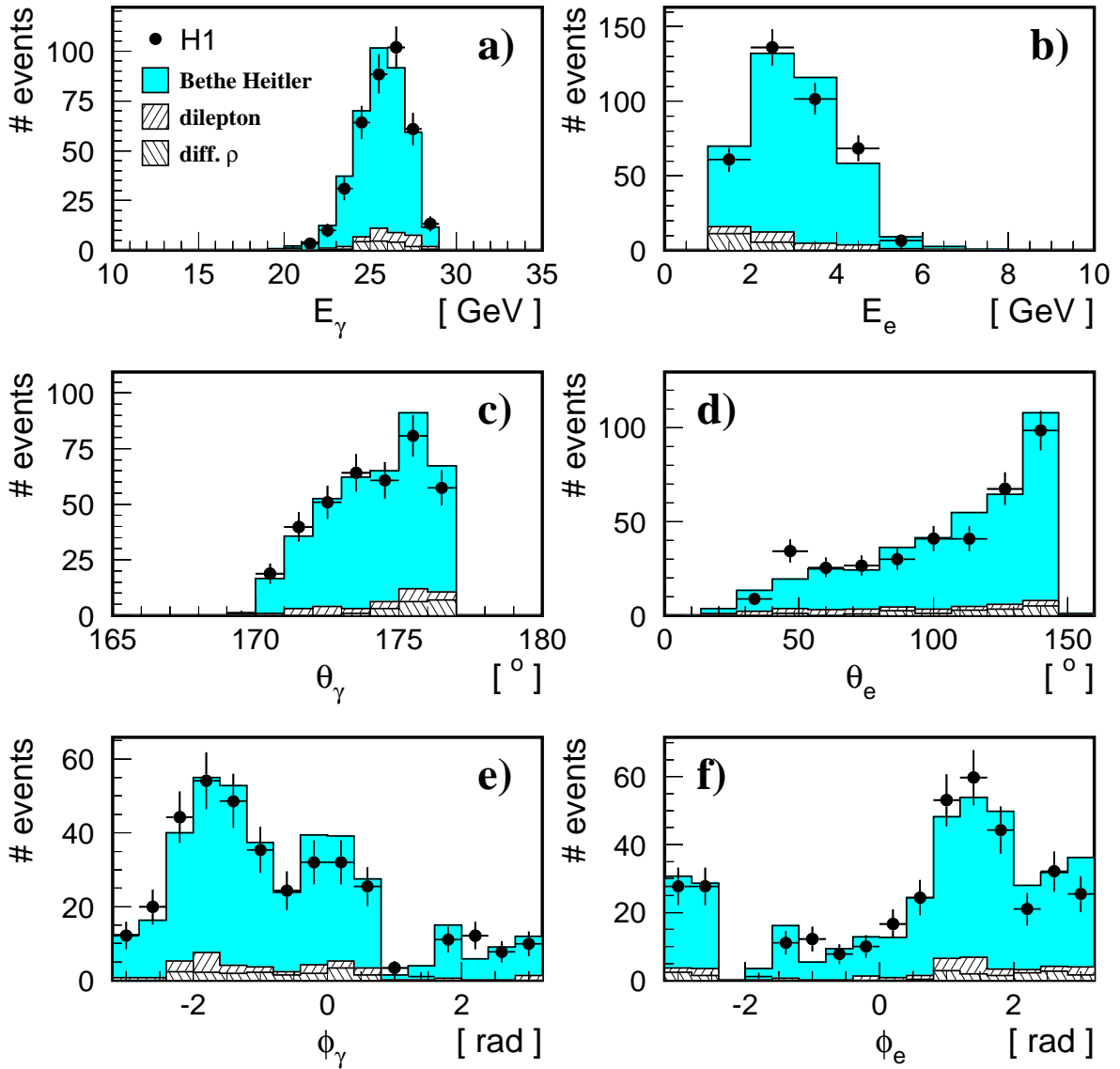
Figure 4.6: *Control sample distributions. The data are compared to the sum of predictions for the Bethe–Heitler process (elastic and quasi–elastic), elastic dilepton production and elastic ρ electro–production. All distributions are absolutely normalised. a) Energy of the photon candidate (i.e. cluster in the Spacal); b) energy of the electron candidate (i.e. cluster in the LAr calorimeter); c) polar angle of the photon candidate; d) polar angle of the electron candidate; e) azimuthal angle of the photon candidate; f) azimuthal angle of the electron candidate.*

the proton is compensated by the final state electron–photon system. For small momentum transfers the $e\gamma$ system is balanced and the Coplanarity variable takes a value close to 180° whereas for large momentum transfer the $e\gamma$ system becomes imbalanced leading to a deviation from 180°. The Coplanarity distribution therefore reflects the distribution of the transferred momentum to the proton. The Bethe–Heitler process is a purely electromagnetic process. The
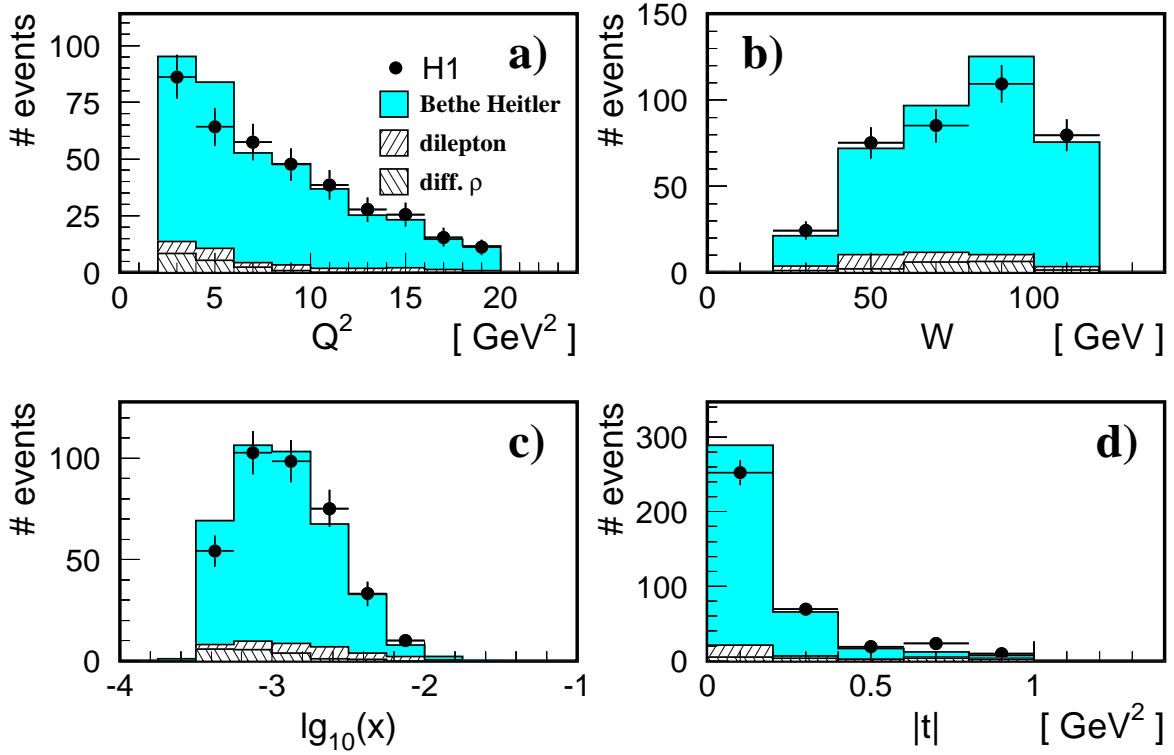
Figure 4.7: *Control sample distributions of the kinematic variables. a)* Q^2, *b)* W, *c)* $lg_{10}(x)$ *and d)* $|t|$. *These kinematic variables have been calculated by treating the electron candidate as the photon and the photon candidate as the electron (see text for details). The data are compared to the sum of MC predictions for the Bethe–Heitler process, diffractive ρ electro–production and dilepton events.*

t dependence can be approximated as $e^{-16|t|/\mathrm{GeV}^2}$ for small values of t [110, 111] which is a quite steep function. For the production of ρ mesons at HERA a $e^{-7|t|/\mathrm{GeV}^2}$ dependence was measured. Therefore the Coplanarity distribution of the BH–process is very narrow function w.r.t. diffractive interactions. A good description of this distribution by the MC predictions is observed.

The distribution of the variable $\sum E - P_z$ reflects the conservation of longitudinal momentum in the reaction. As said before its nominal value is twice the incident electron beam energy $\sum E - P_z = 2E_0 = 55\,\mathrm{GeV}$. The sum is calculated for the final state electron and photon candidate. The influence of the final state proton is negligible since the proton is scattered under small angle such that its longitudinal momentum is almost equal to its energy resulting in a vanishing $E - P_z$ value. A reasonably well description of this distribution is observed. The remaining difference is covered by the systematic uncertainty of the energy measured by the Spacal. If the Spacal energy scale is decreased by 1% corresponding to its absolute uncertainty the description of this distribution by the MC is almost perfect.

Figure 4.9 finally shows the distribution of the reconstructed vertex. Again a good description by the MC simulation is observed. The vertex is reconstructed from the track measured by
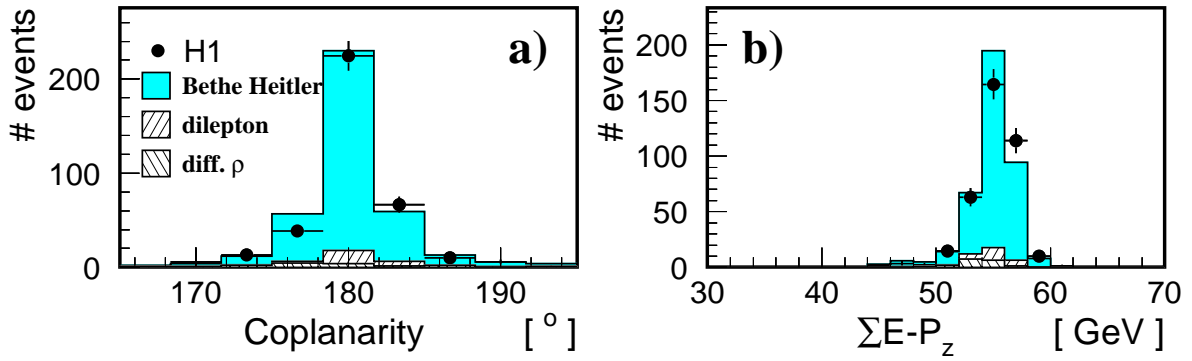
Figure 4.8: *Distributions of the Coplanarity and the variable $\sum E - P_z$ for the control sample. The data are compared to the sum of MC predictions for the Bethe–Heitler process and the different background contributions. The Coplanarity distribution reflects the momentum transfer to the proton while the quantity $\sum E - P_z$ shows the longitudinal momentum conservation.*

the CJC by determining the intersection of the track with the beam axis. The mean value of the central vertex was estimated to be 1.7 cm by fitting a Gaussian to the data. This value is used for the DVCS enriched sample to reconstruct the event kinematics since no vertex can be reconstructed for these events.
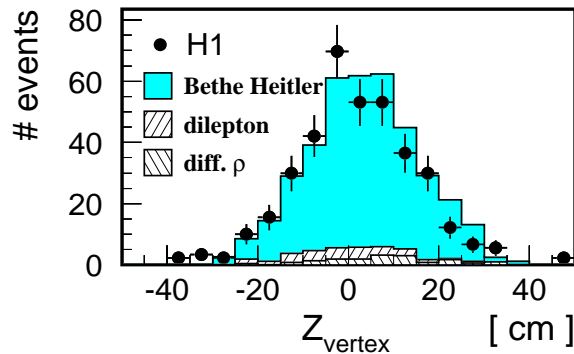

Figure 4.9: *Distribution of the z position of the reconstructed vertex. The data are compared to the sum of the MC predictions for the different contributions.*

The Bethe–Heitler process dominating the control sample is known with high accuracy such that the MC predictions for this sample are reliable. From the good description of the control sample by the sum of the different MC predictions it can be concluded that the detector response is well understood. In particular the measurement of low energetic particles with the LAr calorimeter can be trusted which is of paramount importance for the cross section extraction from the DVCS enriched sample.

4.7　DVCS Enriched Sample

The DVCS enriched sample has been restricted to the kinematic domain $2 < Q^2 < 20\,\mathrm{GeV}^2$, $30 < W < 120\,\mathrm{GeV}$ and $|t| < 1\,\mathrm{GeV}^2$. The lower limit of the Q^2 domain is determined by the geometrical acceptance of the Spacal whereas the Q^2 range is restricted to the upper value due to the measured event rate. The variable W is strongly correlated with the scattering angle of the photon and the cuts have been chosen such that the selected photons lie in the acceptance of the CJC. The lower W cut corresponds to a scattering angle of about $25°$ whereas the upper cut corresponds to about $160°$ for the main part of the events. The cut on the variable $\sum E - P_z > 45\,\mathrm{GeV}$ is imposed to minimise the radiative corrections when extracting the DVCS cross section.

The DVCS enriched sample consists of 172 events which are expected to comprise contributions of both the Bethe–Heitler and the DVCS process. In addition it was found that two non negligible additional processes contribute to the selected event topology: the diffractive electro–production of ω and ϕ mesons. In addition the contribution from proton dissociation Deeply Virtual Compton Scattering has to be taken into account when extracting the cross section for elastic DVCS (see chapter 5).

ω and ϕ Backgrounds

The diffractive electro–production of ω and ϕ mesons was found to contribute to the DVCS enriched data sample

- Diffractive ω vector meson production ($ep \longrightarrow e\omega p$) can contribute to the event topology when the produced ω meson decays into a three photon final state, i.e. $\omega \longrightarrow \pi^0 \gamma$ with the subsequent decay of the π^0 meson in two photons. These events have the same event topology as the DVCS enriched sample when the electron is scattered into the backward direction and measured in the Spacal (i.e. $Q^2 > 1\,\mathrm{GeV}^2$) while only one of the three final state photons is detected in the LAr calorimeter and the two remaining photons leave the main detector either through the beam pipe or their energy is below the noise cut of $E_{cl} < 0.5\,\mathrm{GeV}$. The dominating decay channel $\omega \longrightarrow \pi^+\pi^-\pi^0$ was found not to contribute to the event sample since one of the charged pions enters very likely the tracking detectors leading to a rejection of the event.

- Diffractive ϕ production can contribute to the event topology when the meson decays into kaons, i.e. $\phi \longrightarrow K_L^0 K_S^0$ with the subsequent decay of the K_S^0 into two neutral pions which itself decay into photons. These events contribute to the event topology when the scattered electron is detected in the Spacal and one of the final state photons or the long living kaon is measured in the LAr calorimeter satisfying the selection criteria while the remaining particles again leave the detector through the beam pipe or have an energy below the noise threshold.

In order to study these backgrounds, ω and ϕ events have been generated using the DIFFVM MC program. Note that this event generator does not predict the correct cross sections for the production of ω and ϕ mesons and that hence the generated number of events had to be rescaled [132] such that it corresponds to measured cross sections [68, 63].

A possible background arising from events where an electron interacts with a nucleus of the residual gas in the beam pipe has been studied with a sample of events where only the electron bunches have been filled. No single event which satisfied the selection criteria has been found.

Figure 4.10 shows event distributions for the DVCS enriched sample of the energies and the scattering angles of the final state electron and photon candidate. The data are compared to the sum of MC predictions for the Bethe–Heitler and DVCS process and the discussed vector meson backgrounds. The Bethe–Heitler process and the production of ω and ϕ mesons have been absolutely normalised while the contribution from the DVCS process is normalised such that the total number of MC events corresponds to the number of selected events in the data sample. This method can be applied since the contribution from the interference term of the DVCS and BH process is expected to cancel (for a detailed discussion see chapter 5.4). The Bethe–Heitler contribution to the DVCS enriched sample is estimated using the COMPTON program which generates events for the elastic contribution as well as the contribution from the resonance region to the cross section. The DVCS process has been simulated using the TINTIN MC program developed in this thesis, based on the calculations from Frankfurt, Freund and Strikman, which generates events for the elastic reaction $ep \longrightarrow e\gamma p$. It includes the Bethe–Heitler process, the DVCS process and the interference term.

When comparing the data to the sum of the predictions for the Bethe–Heitler process and the two vector meson backgrounds a large excess of events is observed which is very different in shape as well as in normalisation in comparison to the MC predictions. A good description of the data by the sum of the MC predictions is observed when including the DVCS process. This contribution is able to account completely for the missing parts. As discussed earlier the scattered electron has most likely an energy close to the incident electron beam energy (Figure 4.10a) which justifies the applied selection criterium $E_e > 15\,\text{GeV}$. From this distribution it also can be concluded that no photoproduction background is present which would show up as rising distribution towards low energies. Figure 4.10b shows the energy distribution for the photon candidate where the data again exhibit a quite different shape compared to the prediction of the Bethe–Heitler MC program. As before this difference is completely accounted for by including the DVCS prediction. The strongest differences in shape are observed for the polar angle distribution of the electron and photon candidate (Figure 4.10 c) and d)). The reason for the different shapes of the electron θ–distribution for DVCS and BH lies in the different Q^2–dependencies of the two processes. The strong difference in the polar angle distribution of the photon candidate originates from the different y dependencies of the cross sections. As discussed earlier for the BH–process both the scattered electron and the photon are most likely to be found in the backward direction whereas the photon in the DVCS process is more frequently expected in the central or forward direction. The cutoff at about $25°$ for the photon scattering angle is governed by the cut on the photon proton centre of mass energy $W > 30\,\text{GeV}$. Figure 4.10 e) and f) show the azimuthal angles of the measured electron and photon. The shape of these distributions is governed by the fiducial cuts where the exclusion of the inner part of the Spacal is causing the strongest effect.

The comparison of the distributions shown in Figure 4.10 and Figure 4.6 demonstrates that indeed for the control sample the same energy and angular ranges are covered as for the DVCS enriched sample which justifies the analysis strategy to prove the understanding of the detector response with the help of the control sample. Since it was shown that the detector response is well understood it can now be concluded that the observed excess of the data w.r.t. the Bethe–Heitler MC prediction proofs the existence of an up to now unmeasured process the Deeply Virtual Compton Scattering.
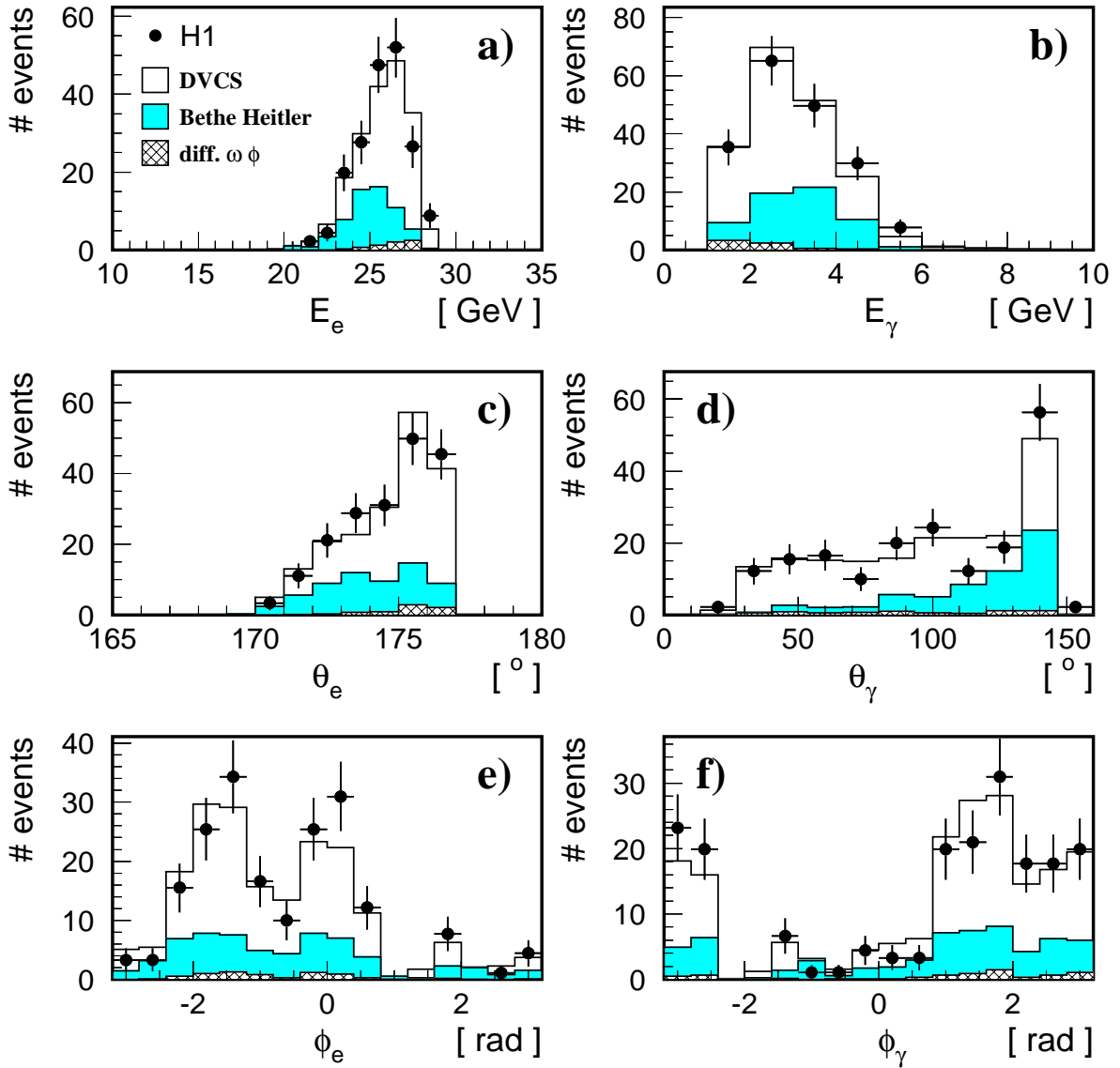
Figure 4.10: *Distributions for the DVCS enriched sample. The data are compared to the sum of the different MC predictions for the contributing processes: DVCS, Bethe–Heitler and diffractive ω and ϕ meson production. The Bethe–Heitler process and the diffractive vector meson contributions have been absolutely normalised whereas the DVCS contribution has been normalised such that the total MC prediction is equal to the number of observed data events. Distributions are shown for a) the energy of the electron candidate (i.e. energy of the cluster in the Spacal), b) the energy of the photon candidate (i.e. energy of the cluster in the LAr calorimeter.), c) the polar angle of the electron candidate, d) the polar angle of the photon candidate, e) the azimuthal angle of the electron candidate and f) the azimuthal angle of the photon candidate.*

Figure 4.11 shows the distributions for the Coplanarity and the variable $\sum E - P_z$. Again a good description of these variables can be achieved by summing up the different MC predictions. When comparing the data with the grey histogram it is observed that the Coplanarity distribution is broader for the data than expected for the contribution of the Bethe–Heitler process. As already discussed above the origin for the sharp[1] Bethe–Heitler distribution originates from the momentum transfer to the proton which is governed by the steeply falling electromagnetic form factor. In case of diffractive interactions it is already known from proton–proton scattering (see section 1.3) that the dependence of the cross section on the momentum transfer at the proton vertex is much flatter ($e^{-10|t|/\mathrm{GeV}^2}$ in comparison to $e^{-16|t|/\mathrm{GeV}^2}$ for BH). This confirms the expectation that the newly observed process originates from an diffractive interaction.

The quantity $\sum E - P_z$ is calculated from the energy and the z–component of the electron and photon candidate. A good description of this variable is observed by the sum of the MC predictions for the contributing processes (see Figure 4.11 b)).
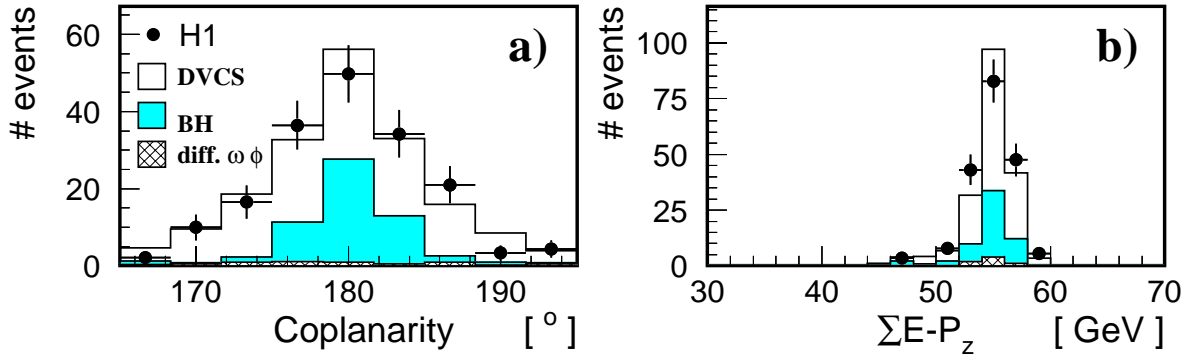

Figure 4.11: *Distributions of the Coplanarity and the variable $\sum E - P_z$ for the DVCS enriched sample. The data are compared to the sum of the different MC predictions.*

Backgrounds from Low Multiplicity Events

A possible background to the DVCS enriched sample could arise from low multiplicity DIS events when the scattered electron is detected in the Spacal and one of the hadronic final state particles fakes the photon signature in the LAr calorimeter while the remaining particles of the hadronic final state leave the detector through the beam pipe unseen.

The usage of standard DIS MC generators to investigate this background is not possible as they have been optimised to describe inclusive high multiplicity DIS events. The DJANGO program for instance predicts a background arising from low multiplicity events which has the same magnitude as the actually observed signal whereas no single background event to the

---

[1]Note that in case of the DVCS enriched sample the Coplanarity distribution for the Bethe–Heitler process is slightly broader w.r.t. the Coplanarity distribution for the control sample which can be understood by the different reconstruction of the azimuthal angle ϕ of the scattered particle in the central part of the detector. For the control sample it has been determined from the track reconstructed in the CJC. In case of the DVCS enriched sample it has been determined from the cluster position of the photon candidate. Due to the poorer spatial resolution of the LAr calorimeter a broader Coplanarity distribution is obtained.

DVCS enriched sample is found when using the HERWIG program. The different results of the two MC generators originate most probably from the different fragmentation algorithms used in these programs and is not physical. Therefore a possible background from DIS has to be estimated from the data itself.

If such background events really exist it is most probable that in the majority of cases the neutral particle which fakes up the photon signature in the LAr calorimeter is the lightest neutral meson, the π^0 meson. The background which is predicted by the DJANGO program actually consists of a fraction of 2/3 of neutral pions and 1/3 of η mesons faking a photon accompanied by additional neutral pions which escape detection through the beam pipe.

The basic idea for investigation of this kind of background events is to directly reconstruct neutral mesons via their two decay photons. Due to the cut on the transverse momentum for the cluster in LAr calorimeter ($P_T > 1\,\text{GeV}$) the clusters energy is at least $1\,\text{GeV}$. For these energies it is expected that the two decay photons from the pion deposit their energy very close together in the calorimeter. Depending on the size of the calorimeter cells, which changes with the polar angle θ, only for a small fraction of events two separate clusters are actually reconstructed by the H1 reconstruction program. For the majority of events only a single cluster is observed.

The minimum opening angle $\theta_{\gamma_1\gamma_2}^{\min}$ between the two photons originating from π^0 decay can be calculated with the formula

$$\cos \theta_{\gamma_1\gamma_2}^{\min} = 1 - \frac{2 \cdot m_{\pi^0}^2}{E_{\pi^0}^2} \tag{4.5}$$

where m_{π^0} denotes the pion mass and E_{π^0} its energy. It turns out that the distribution of the opening angle is a very steeply falling function starting at the minimal opening angle [133] such that for most events it is very close to the minimum angle $\theta_{\gamma_1\gamma_2}^{\min}$. For a pion with an energy of $3\,\text{GeV}$ the opening angle is $7.5°$ which corresponds to a distance of $13\,\text{cm}$ between the impact points in the LAr calorimeter for a scattering angle $\theta_\pi = 90°$.

In order to investigate the separation power of the LAr calorimeter a study with simulated pions has been performed where events with single pions are generated and subjected to the H1 detector simulation and reconstruction program. A selection of events with at least two electromagnetic clusters in the LAr calorimeter has been performed and the invariant mass of the two photon candidates is reconstructed. The two clusters are required to have an energy larger than $0.5\,\text{GeV}$.

In Figure 4.12 a) the reconstructed invariant mass spectrum of these events is shown exhibiting a clear peak around the nominal π^0 mass. Background from clusters originating from electronic noise in the calorimeter, correctly taken into account in the simulation, is not observed. For this study neutral pions have been simulated in the energy range $1.2 < E_{\pi^0} < 5.0\,\text{GeV}$ uniformly distributed over the polar angle range $25° < \theta_{\pi^0} < 142°$ which corresponds to the region for the enriched DVCS sample. In Figure 4.12 b) the energy distribution for the generated and reconstructed pions is shown whereas in Figure 4.12 c) these quantities are given as a function of the polar scattering angle θ_{π^0}. Figure 4.12 d) shows the efficiency of reconstructing π^0 mesons as a function of energy. The falling distribution can by understood by the fact that with increasing energy the opening angle between the two decay photons decreases. The shape of the reconstructed pion distribution as a function of the polar angle (see Figure 4.12 c) is due to the size of the cells in the electromagnetic LAr calorimeter which is smaller for the central part of the LAr calorimeter thus decreasing the separation power. The overall reconstruction efficiency for pions is found to be about 20% which makes the investigation of the pion background via this method feasible.
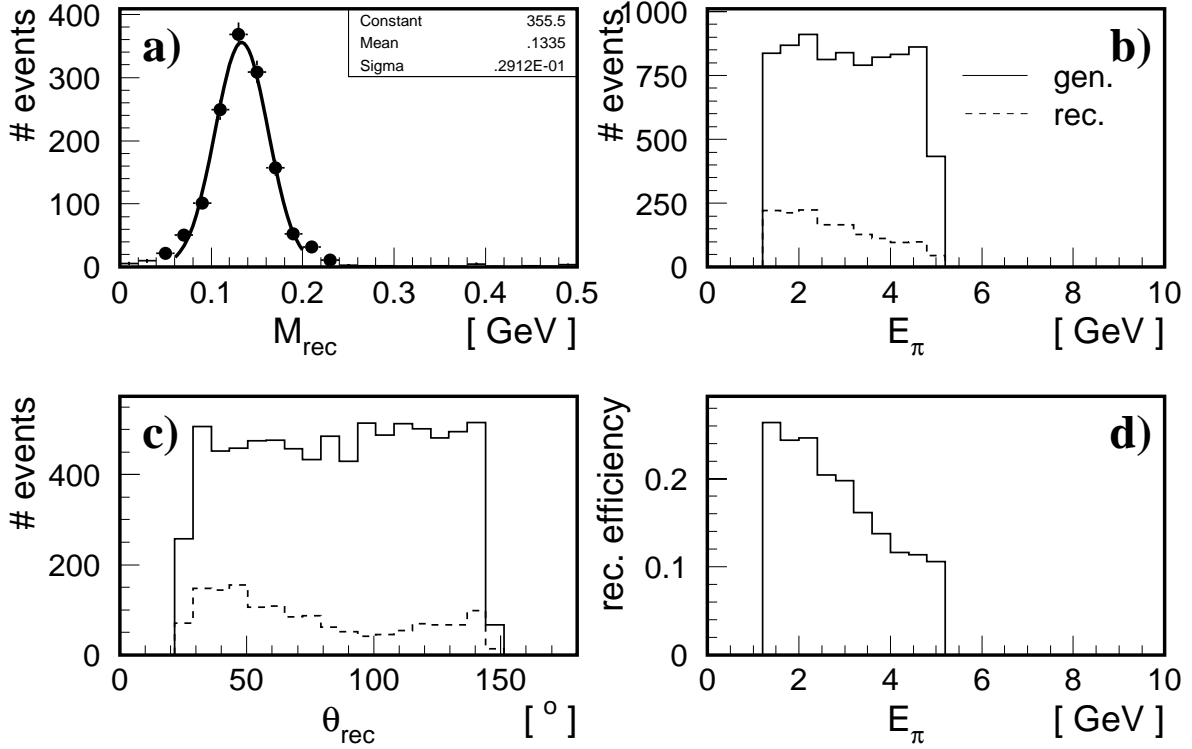
Figure 4.12: *The π^0 background studied using events with two electromagnetic clusters in the LAr calorimeter. a) the reconstructed invariant mass spectrum for a sample of simulated π^0's, b) the distribution of the generated and reconstructed energy, c) the generated and reconstructed polar angle of the π^0 mesons and d) the reconstruction efficiency in dependence of the generated pion energy.*

Since the described method for investigating the low multiplicity background has been proven to be feasible a sample of events has been selected from the data with two clusters in the LAr calorimeter with an energy $E_{cl} > 0.5\,\text{GeV}$. In addition an electron candidate is required to be found in the Spacal using the same cuts as for the DVCS enriched sample. Since pions with an energy starting at $E_{\pi^0} = 1\,\text{GeV}$ should be studied the cut on the cluster energy has been decreased to $E_{cl} > 0.5\,\text{GeV}$ because the energy of the pion is shared by two photons. All additional cuts which have been applied for the DVCS enriched sample are also imposed for this selection. In Figure 4.13 a) the reconstructed mass spectrum is shown for the selected events. The data are compared to the sum of the prediction for diffractive ω and ϕ production. No prominent peak around the nominal π^0 mass can be observed. The mass spectrum is entirely described by the sum of the predictions for vector meson production. When integrating over the full mass spectrum the data are described by the MC predictions within 1.3 standard deviations. The enhancement of events at about $M_{rec} \sim 0.7\,\text{GeV}$ actually originates from the decay of ω mesons into a neutral pion and a photon where the two photons from the π^0 decay is detected as one cluster and the photon as the second cluster. When reconstructing the invariant mass of the two clusters it is observed to be slightly below the nominal ω mass. To ensure that the separation from one to two clusters is adequately described by the H1 detector simulation the distributions of opening angles are studied. In Figure 4.13 b) and c) the differences of the measured polar

angles $\Delta\theta$ and azimuthal angle $\Delta\phi$ are shown. A good description of these variables by the MC simulations is found. Figure 4.13 d) and e) show the opening angles for the events with a reconstructed mass below $M_{rec} < 0.25\,\text{GeV}$ again well described by the MC predictions.
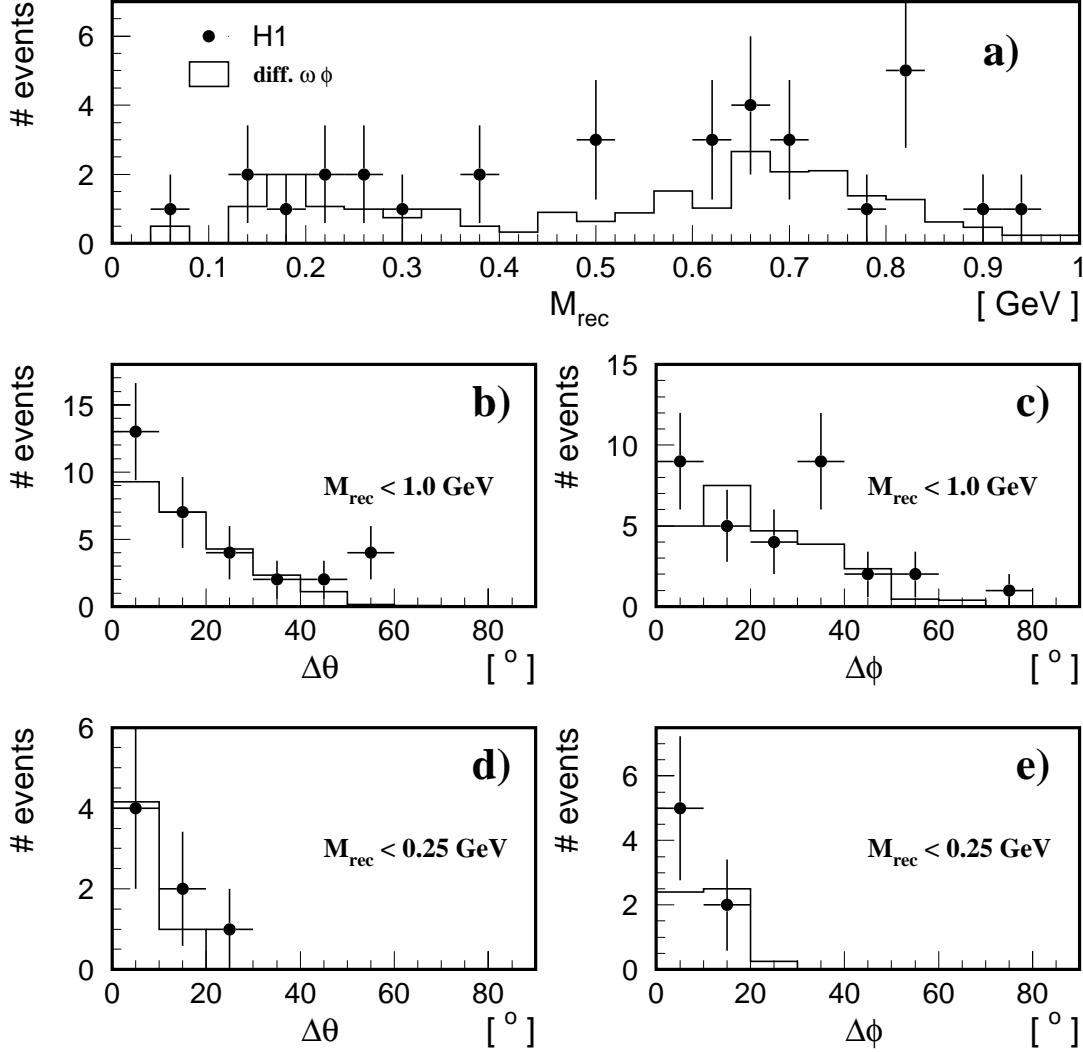

Figure 4.13: a) Mass spectrum for reconstructed events with two electromagnetic clusters in the LAr calorimeter. The data are compared to the sum of the predictions for diffractive electro–production of ω and ϕ mesons. b) Difference of the polar angle θ of the two reconstructed electromagnetic clusters for a reconstructed mass $M_{\text{rec}} < 1\,\text{GeV}$. c) Difference of the azimuthal angle ϕ of the two reconstructed clusters for a reconstructed mass $M_{\text{rec}} < 1\,\text{GeV}$. d) Difference of the polar angle θ of the two reconstructed electromagnetic clusters for a reconstructed mass $M_{\text{rec}} < 0.25\,\text{GeV}$. e) Difference of the azimuthal angle ϕ of the two reconstructed clusters for a reconstructed mass $M_{\text{rec}} < 0.25\,\text{GeV}$.

From this study it is concluded that the total background from DIS with a neutral pion faking the photon in the enriched DVCS sample is accounted for by the predictions for diffractive ω and ϕ electro–production. Additional backgrounds from low multiplicity DIS events with neutral pions in the final state are not present in the selected data sets.

Chapter 5

Cross Section Measurement

In this chapter the determination of the elastic differential cross section for the reaction $ep \longrightarrow e\gamma p$ as a function of Q^2 and W in the kinematic range $2 < Q^2 < 20\,\mathrm{GeV}^2$, $30 < W < 120\,\mathrm{GeV}$ and $|t| < 1\,\mathrm{GeV}$ will be discussed. After subtraction of the contribution from the Bethe–Heitler process the photon–proton cross section ($\gamma^* p \longrightarrow \gamma p$) will be extracted which in the next chapter will then be compared to theoretical predictions.

5.1   Cross Section Determination

The differential electron–proton cross section for the reaction $ep \longrightarrow e\gamma p$ is obtained from the DVCS enriched sample by the formula:

$$\frac{\mathrm{d}\sigma_{bin}}{\mathrm{d}Q^2} = \frac{(N_{bin} - N_{backg.} - N_{p.dis.})}{\epsilon \cdot A \cdot \Delta Q^2 \cdot \mathcal{L}} \cdot (1 + \delta_{rad}), \tag{5.1}$$

$$\frac{\mathrm{d}\sigma_{bin}}{\mathrm{d}W} = \frac{(N_{bin} - N_{backg.} - N_{p.dis.})}{\epsilon \cdot A \cdot \Delta W \cdot \mathcal{L}} \cdot (1 + \delta_{rad}) \tag{5.2}$$

where $\frac{\mathrm{d}\sigma_{bin}}{\mathrm{d}Q^2}$ and $\frac{\mathrm{d}\sigma_{bin}}{\mathrm{d}W}$ denote the differential cross section for a certain bin in Q^2 and W, respectively. The cross section $\frac{\mathrm{d}\sigma_{bin}}{\mathrm{d}Q^2}$ is measured in the kinematic range $30 < W < 120\,\mathrm{GeV}$ and $|t| < 1\,\mathrm{GeV}^2$ whereas the cross section $\frac{\mathrm{d}\sigma_{bin}}{\mathrm{d}W}$ is determined for $2 < Q^2 < 20\,\mathrm{GeV}^2$ and $|t| < 1\,\mathrm{GeV}^2$. N_{bin} is the number of events from the DVCS enriched sample in a certain bin. $N_{backg.}$ and $N_{p.dis.}$ are the number of background events (from diffractive electroproduction of ω and ϕ mesons) in that bin and the number of proton dissociation events, respectively. ϵ is the efficiency of the event selection which decomposes into two terms $\epsilon = \epsilon^{Trigger} \cdot \epsilon^{Noise}$ where $\epsilon^{Trigger}$ denotes the trigger efficiency and ϵ^{Noise} originates from losses due to noise in the forward detectors leading to a rejection of events. A is the acceptance for reconstructing events in a certain bin; it takes the geometrical acceptance of the detector as well as migrations and selection efficiencies into account. ΔQ^2 and ΔW are the actual bin sizes. The cross section is corrected for higher order QED contributions such that the measurement can be directly compared to theoretical predictions. This correction is denoted by the term $(1 + \delta_{rad})$. $\mathcal{L}$ is the integrated luminosity of the event sample taken into account in this analysis.

Definition of Bins

The binning has been chosen such that the number of selected events is almost equal for all bins and that the bin size is larger than the resolution for reconstruction of the kinematic variables which have been found to be $\sigma\left(Q^2\right) = 13\,\%$ and $\sigma\left(W\right) = 5\,\%$, respectively. This minimises the systematic uncertainties as well as migration effects. The cross section is measured in four bins of Q^2 over the whole W range and in four bins of W for the entire Q^2 regime. The bin definition and the number of selected events per bin is given in Table 5.1.

Q^2–domain [GeV^2]			# events		W–domain [GeV]			# events
2.0	-	4.0	58		30	-	60	60
4.0	-	6.5	44		60	-	80	35
6.5	-	11.0	43		80	-	100	51
11.0	-	20.0	27		100	-	120	26

Table 5.1: *Bin definition for the measurement of the differential cross section as function of Q^2 and W and number of events per bin.*

Acceptance Correction

The acceptance A has been estimated for each bin using a sample of simulated events generated with the TINTIN MC program. It is defined by the formula

$$A = \frac{N_{rec}}{N_{gen}}, \tag{5.3}$$

where N_{rec} is the number of events reconstructed in a certain bin and N_{gen} is the number of events generated in that bin. This procedure takes into account the limited geometrical acceptance of the detector induced by the fiducial cuts as well as migration effects due to the limited resolution of the apparatus. This is however only true if the detector resolution is correctly described by the detector simulation which is ensured by the observation that the distributions for both, the control sample and the DVCS enriched sample, are correctly described by the sum of the different MC predictions (see Chapter 4). The acceptance calculation must be further modified such that it accounts for the contribution of events with an interaction vertex at the position of the forward satellite vertex. This leads to the relation:

$$A = \frac{N_{rec\,\mathrm{NV}} + f \cdot N_{rec\,\mathrm{SV}}}{N_{gen\,\mathrm{NV}} + f \cdot N_{gen\,\mathrm{SV}}}, \tag{5.4}$$

where $N_{rec\,\mathrm{NV}}$ and $N_{rec\,\mathrm{SV}}$ are the number of reconstructed events which originate from the nominal vertex (NV) and satellite vertex (SV), respectively, while $N_{gen\,\mathrm{NV}}$ and $N_{gen\,\mathrm{SV}}$ are the corresponding numbers for the generated sample. The fraction f is ratio of events originating from the satellite vertex and the number of events originating from the nominal vertex. In the present case f is $3.5\,\%$ determined by the luminosity system in combination with the Time of Flight system which was used to study the bunch structure.

For the determination of the acceptance using the TINTIN program an exponential t–dependence of the cross section has been assumed $\frac{d\sigma}{dt} \sim e^{-b|t|}$ where the slope parameter b has been chosen to be $b = 7\,\mathrm{GeV}^{-2}$, a value which has been measured for elastic production of ρ mesons in

diffractive ep scattering [60], b has been varied by two units $b = 7 \pm 2\,\mathrm{GeV}^{-2}$ which leads to a variation of the cross section by less than $2\,\%$ and has been taken into account in the systematic uncertainty.

The resulting acceptance is on average $25\,\%$ which mostly originates from the fiducial cuts for the electron candidate in the Spacal and the geometric requirements in the CJC. The acceptance is $8.5\,\%$ for the lowest bin in Q^2 and rises up $60\,\%$ for the highest bin in Q^2; there is almost no dependence as function of W.

Purity and Stability

In order to control the quality of the measurement the purity $\mathcal{P}$ and stability $\mathcal{S}$ are calculated which are a measure for the migration of events from one bin to an other. The purity $\mathcal{P}$ is defined by

$$\mathcal{P} = \frac{N_{rec\&gen}}{N_{rec}} \qquad \in [0,1]\,, \tag{5.5}$$

where $N_{rec\&gen}$ denotes the number of events which have been generated and reconstructed in a bin and N_{rec} is the number of events which have been reconstructed in the same bin. An ideal detector would measure all events in the same bin as their true value leading to a purity of 1. In case of migrations due to the limited detector resolution events from outside a certain bin are reconstructed inside the bin and N_{rec} increases leading to a purity below unity.

The stability $\mathcal{S}$ is defined via:

$$\mathcal{S} = \frac{N_{rec\&gen}}{N_{gen}} \qquad \in [0,1]\,, \tag{5.6}$$

where N_{gen} denotes the number of events which have been generated in the bin in question after application of all selection criteria. For the ideal case the stability $\mathcal{S}$ is 1 while migration of events outside the bin of their true value is, lead to a decrease of $N_{rec\&gen}$ resulting in a stability value smaller than 1.

In Figure 5.1 the purity and stability are shown for all bins chosen for the measurement. The determined values are about $70 - 90\,\%$ and show almost no dependence on Q^2 and W. The purity and stability for the measurement as a function of W are about $10\,\%$ higher than for the measurement in Q^2 which can be understood due to the better resolution for reconstructing W in contrast to Q^2.

Trigger Efficiency

As discussed earlier events are triggered by the subtrigger $S3$ and the level 4 selection algorithm for inclusive diffractive DIS events. The efficiency for the subtrigger $S3$ has been determined using an independent subtrigger as reference sample [134]. In Figure 5.2 the efficiency of the trigger elements SPCLe_IET_1 and SPCLe_IET_2 is shown as a function of the energy deposited in the Spacal together with the time dependence of the total efficiency for energies above $7\,\mathrm{GeV}$ over the whole data taking period. Both trigger elements are found to be fully efficient for energies above $7\,\mathrm{GeV}$. Luminosity runs with a trigger efficiency less than $98.5\,\%$ have been excluded from the analysis. Efficiency losses due to the other trigger elements used in the S3 subtrigger condition have been estimated to be negligible; $S3$ is thus determined to be $100\,\%$ efficient.
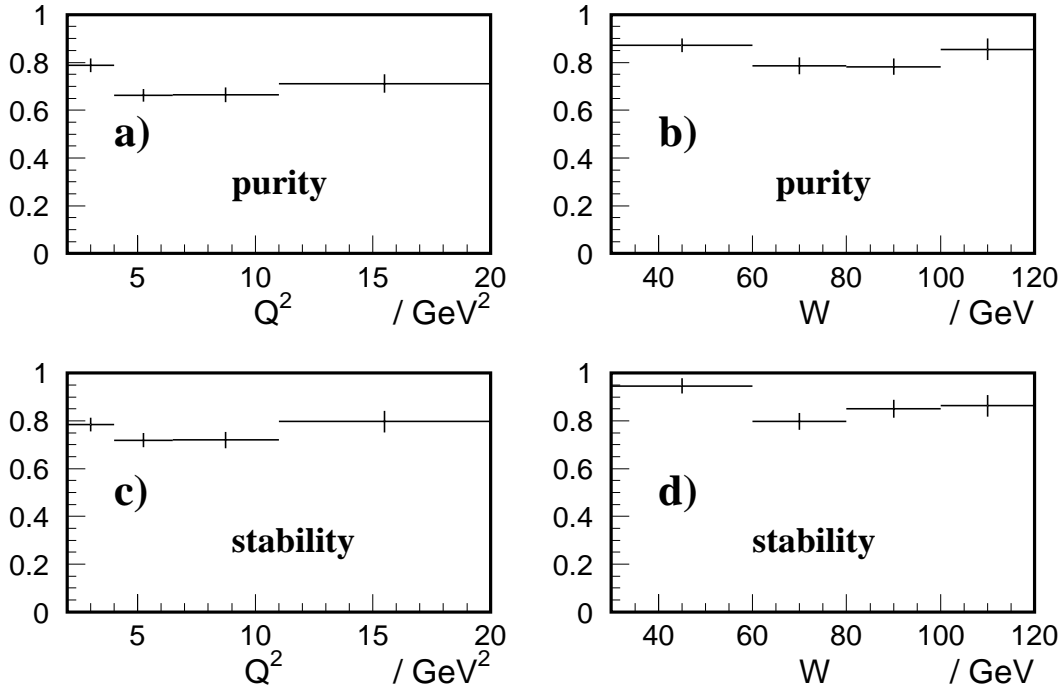
Figure 5.1: *The purities and stabilities for the bins used in the measurement: a) purity in dependence of Q^2, b) purity in dependence of W, c) stability in dependence of Q^2, d) stability in dependence of W.*

The level 4 selection algorithm has also been determined to be fully efficient since the final selection criteria are stronger than the cuts applied on the filter farm level. This has been checked using so called L4reject tapes, a subsample of actually rejected events. One out of 100 rejected events is written to tape and subjected to the same reconstruction program as those events accepted by level 4. Not a single good event was found in the L4reject sample.

The Veto Conditions

The forward detectors (FMD and PRT), the LAr calorimeter and the CJC are used for the selection of elastic events by demanding the absence of any signal except the photon in the LAr calorimeter. Noise in these detectors can lead to a loss of *good* events which has to be corrected for when extracting the cross section. Figure 5.3 shows the noise for a) the FMD and b) the PRT as a function of luminosity fills. It has been determined by using so called random trigger events, which are taken with a rate of 0.1 Hz during the normal data taking. They are subjected to the same reconstruction program as the ordinary data. To determine the noise from these random trigger data, events have been selected which do not have any cluster in the LAr calorimeter above an energy of 0.5 GeV.

To determine the noise in the FMD the number of events with more than one hit pair in the first three FMD layers is divided by the total amount of events with no signal in the LAr calorimeter.
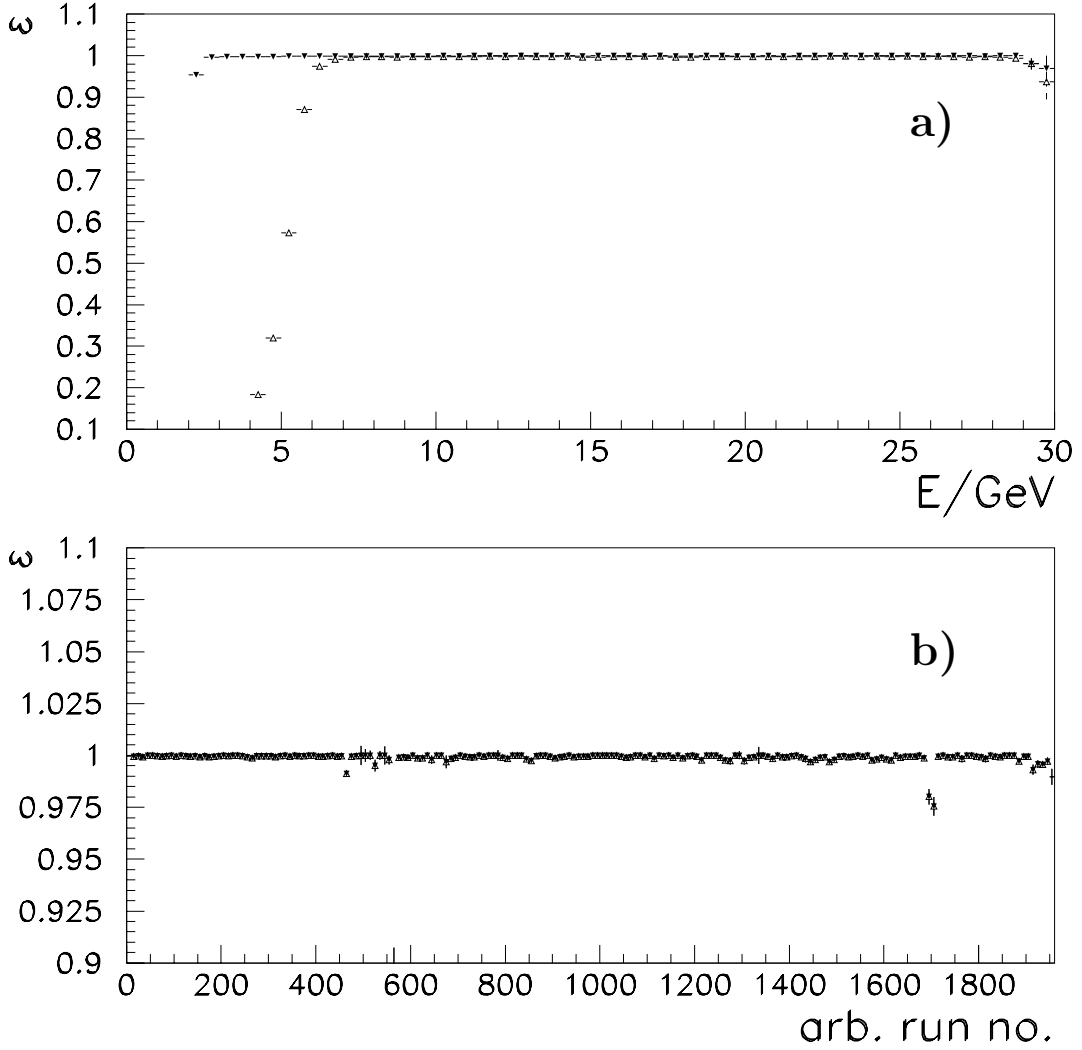
Figure 5.2: *Efficiency of the trigger elements SPCLe_IET_1 (full triangles) and SPCLe_IET_2 open triangles) [134]: a) Efficiency in dependence of the cluster energy; b) Efficiency of the trigger element SPCLe_IET_1 and SPCLe_IET_2 for energies above 4 GeV as function of the luminosity run for the complete data taking period. Single runs with an efficiency less than 98.5 % are excluded from the analysis.*

For the PRT the number of events with any hit is divided by the total number of events with no cluster in the LAr calorimeter.

As can be inferred from Figure 5.3 the data taking period 1997 is divided into five periods from which only data of the periods II and IV have been used in the analysis. The noise for these periods has been determined to be $5.3 \pm 1.5\,\%$. The origin of the noise is synchrotron radiation from the positron beam which can be investigated in further detail by studying the contribution from each layer of the FMD. It turned out that the dominant contribution to the noise comes from the most forward layer which is exposed most to the synchrotron radiation. A short phase

in period IV with a higher noise level than for the rest of the period. has been traced back to wrong collimator settings upstream the electron beam which were designed to protect the detector from synchrotron radiation. The noise in the PRT can be savely neglected since it is always well below 0.5 %.
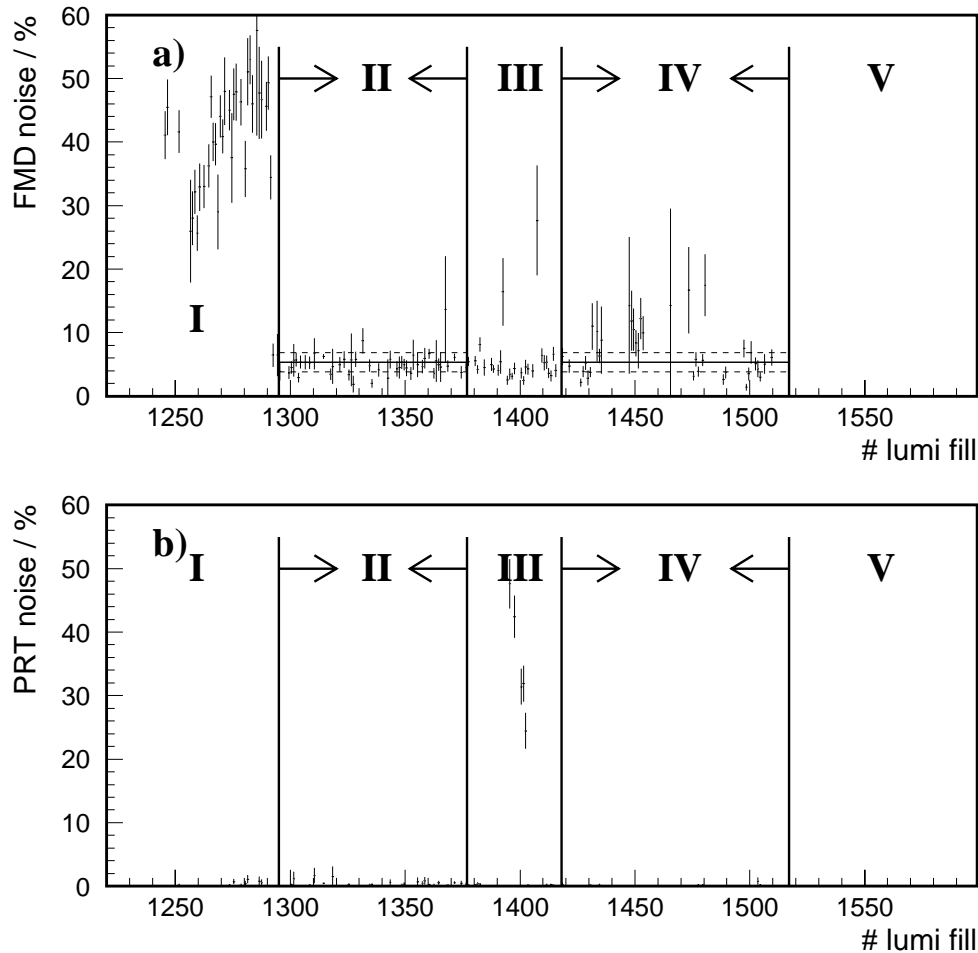

Figure 5.3: *Noise in the forward detectors as function of the lumi fill number: a) noise in the forward muon detector (FMD); b) noise in the proton remnant tagger (PRT). The five different regions correspond to different detector conditions for the data taking. I) Problems in the FMD readout leading to an abnormal high noise rate; II) normal data taking; III) Problems in the PRT readout; IV) normal data taking; V) change of trigger setup. The solid line in a) indicates the fitted noise of 5.3 %. The error of 1.5 % is shown by the dashed lines.*

Period I has been neglected due to severe read out problems in the FMD which led to a mixing of the FMD signals from different events. The effect results in an increase of the noise up to $40 - 50\,\%$. Period III has not been used in the analysis due to malfunctioning of the PRT leading to an increase of its noise to an abnormal high level. Period V has been excluded from

the analysis since no appropriate trigger setup was available for DVCS events.

The noise in the LAr calorimeter has already been taken into account when determining the acceptance A. The H1 detector simulation overlaps randomly triggered events from the LAr calorimeter during the event simulation. These noise events have been recorded in special runs throughout the data taking.

A further correction of $3.5\pm2.0\%$ originates from a read out problem in the CJC which consisted in the mixing of signals from different events in the recorded event. Some wire signals were actually taken from the event triggered directly before the event in question eventually leading to fake hits. These wrong hits mostly led to a reconstructed track resulting in a rejection of the event in this analysis. Since this error happened randomly for different (small) regions of the CJC the influence on the analysis was found to be small and could be corrected for. The correction factor of 3.5% has been determined from an event sample of randomly triggered events.

Proton Dissociation Background

The selection criteria have been chosen such that the contribution from proton dissociation events is suppressed. Especially the cuts on the forward detectors (FMD and PRT) have been designed for a rejection of inelastic DVCS events. Due to their limited geometrical and kinematic acceptance there is however still a sizable background from this process present.

This has been estimated from the relative amount of untagged (events which survive the cuts on the FMD and PRT) and tagged events (events which have signals in the forward detectors) in combination with the efficiency to tag events from elastic and proton dissociation processes. The total number of events N_{tot} can be written as the sum of untagged and tagged events

$$N_{tot} = N_{untagged} + N_{tagged}. \tag{5.7}$$

At the same time N_{tot} is also given by the sum of elastic and proton dissociation events

$$N_{tot} = N_{el.} + N_{diss.}. \tag{5.8}$$

Note that $N_{diss.}$ denotes only proton dissociation events which leave no signal in the main detector, neither the CJC nor the LAr calorimeter. Therefore this method cannot be used to determine the cross section for the proton dissociation process. When introducing the probabilities $P_{diss-tag}$ and P_{el-tag} which denote the probability to tag proton dissociation and elastic events, respectively, the following formula can be derived

$$N_{el} = \frac{N_{untagged} - N_{tot} \cdot (1 - P_{diss-tag})}{P_{diss-tag} - P_{el-tag}}. \tag{5.9}$$

The numbers $N_{untagged}$ and N_{tot} are derived from data. The tagging efficiencies $P_{dis-tag}$ and P_{el-tag} have been determined using the DIFFVM MC program in combination with the H1 detector simulation. The DIFFVM program offers the possibility to generate the four vectors of all particles in the hadronic final state which is not possible for the TINTIN program which generates only elastic events. The DIFFVM program has been run in the ρ–meson mode which should have no influence on the analysis since it is expected that the cross section for generating an excited mass M_Y of the proton has the same shape for ρ meson production as for DVCS. In chapter 4 it was discussed that the forward detectors are correctly described by the H1 detector

simulation (see Figure 4.3). Therefore the simulation can be used to determine the two tagging efficiencies in question. Using this method the following results have been derived

$$
\begin{aligned}
P_{diss-tag} &= 0.56, \\
P_{el-tag} &= 0.005.
\end{aligned}
$$

The uncertainty on the extraction of the proton dissociation background has been estimated by varying the FMD efficiency by $\pm 4\%$ and the PRT efficiency by $\pm 25\%$ where the value for the FMD is justified by the differences between the data and the MC prediction. The large variation for the PRT originates from the large correction which had to be applied to get a good description of the data by the MC simulations. The final result for the proton dissociation background which has to be subtracted from the data is $16 \pm 8\%$.

Background from ω and ϕ Production

It was found (see chapter 4) that background from diffractive electro–production of ω and ϕ mesons contributes to the enriched DVCS sample. This is statistically subtracted bin by bin. It has been estimated using the DIFFVM MC program that this background contributes by about 3.5% in average being less than 6% for any of the used bins. The prediction from the DIFFVM MC program has been normalised to measured cross sections [132, 63, 68].

Radiative Corrections

The cross section has been corrected for QED initial state radiation (ISR), i.e. for the collinear emission of photons off the incoming electron, which for HERA kinematics represents the most important contribution to the higher order QED corrections. The effect due to photon emission from the outgoing electron can be neglected since such photons are radiated in the outgoing electron direction and deposit thus their energy in the same cluster of calorimeter cells.

The factor $(1 + \delta_{rad})$ (see equations 5.1 and 5.2) has been determined by the MC program TINTIN which was run with and without inclusion of initial state radiation. The earlier discussed comparisons between data and MC predictions as well as the determination of the acceptance have been performed with a DVCS MC sample including ISR. The correction factor $1 + \delta_{rad}$ can now be calculated using the relation

$$
1 + \delta_{rad} = \frac{\sigma_{DVCS}^{Born}}{\sigma_{DVCS}^{Born+ISR}} \tag{5.10}
$$

where σ_{DVCS}^{Born} denotes the cross section on the born level and $\sigma_{DVCS}^{Born+ISR}$ the cross section including ISR as estimated using the MC program. This correction was determined bin wise and found to be about 3% independent of Q^2 and W. This small value justifies the cut $\sum E - P_z > 45\,\text{GeV}$ since δ_{rad} would be about 10% without this requirement.

5.2 The ep Cross Section

All variables of equations 5.1 and 5.2 having estimated, the cross section can be calculated. The measured differential cross section of the reaction $ep \longrightarrow e\gamma p$ is shown in Figure 5.4 as a function

of Q^2 and W and compared to the contribution from the Bethe-Heitler process. The data points are given with the statistical error (inner error bars) and the statistical and systematic error (see below) added in quadrature (outer error bars). The measured cross section is observed to be quite different in shape and normalisation in comparison to the expectation for the Bethe–Heitler process. When fitting the Q^2 dependence of the cross section with a function

$$f\left(Q^2\right) = a \cdot \left(\frac{1}{Q^2}\right)^n.$$
(5.11)

The parameter n was found[1] to be $n = 2.47 \pm 0.14$ which significantly differs from $n = 2.0$ expected for the Bethe–Heitler process. For the measured cross section as function of W the difference in shape is even more evident. For large values of W corresponding to the electron and the photon being scattered into the backward direction, the Bethe–Heitler process dominates the cross section. Its contribution to the cross section decreases rapidly towards small values of W whereas the measured cross section however tends to be rather constant.

As discussed in chapter 2 the interference term contributing to the cross section is proportional to $\cos\phi_R$ where ϕ_R is the angle between the electron scattering and photon production plane in the photon–proton centre of mass system. Since the measurement is performed for all values of ϕ_R (see below for a detailed discussion) the interference term cancels. Hence the observed difference between the measured cross section and the contribution from the Bethe–Heitler process can be entirely attributed to the DVCS process. As the $\cos\phi_R$ dependence follows from the helicity dependence of the QCD matrix element it is assumed to be true for all models (e.g. dipole models) which do not aim to predict the interference term and only provide results for the pure DVCS contribution.

5.3 Systematic Errors

In this section the systematic uncertainties and their influence on the measurement will be discussed. They are divided into two contributions, one which covers all global systematic uncertainties shared by all data points and one with the bin dependent uncertainties. The global uncertainties taken into account are:

- Luminosity measurement: 1.5%,

- Noise determination for the FMD: 1.5%,

- Noise determination for the CJC noise (event mixing induced): 2%,

- Subtraction of the proton dissociation background: 8%,

- Uncertainty on the acceptance correction (including the change of acceptance by varying the t-slope): 4%.

When added in quadrature, they add up to a total global uncertainty of 9.4%.

The bin dependent uncertainties are derived by varying the relevant measurement related quantities (e.g. energy scales) within their experimental uncertainties (in positive and negativ direction) taking the maximal deviation of the resulting cross section as systematic error. The

---

[1]Note that the cross section has not been corrected for the bin centre. It was however found that changing the centre for single bins does only marginally influence the results of the fit.

uncertainties from the different sources are then added in quadrature. They are listed in Table 5.2 and 5.3 together with the measured ep cross sections.

range in Q^2			$\frac{d\sigma^{ep \longrightarrow e\gamma p}}{dQ^2}$	δ_{stat}	$\delta_{E_\gamma \pm 4\,\%}$	$\delta_{E_e \pm 1\,\%}$	$\delta_{\theta_\gamma \pm 3\,\mathrm{mrad}}$	$\delta_{\theta_e \pm 1.3\,\mathrm{mrad}}$	δ_{global}	δ_{tot}
[GeV^2]			[pb/GeV^2]	[%]	[%]	[%]	[%]	[%]	[%]	[%]
2.0	-	4.0	37.6	14	1.8	1.8	1.8	9	9.4	20
4.0	-	6.5	8.0	16	2.4	2.4	2.4	10	9.4	21
6.5	-	11.0	2.87	16	2.4	0.0	0.0	7	9.4	20
11.0	-	20.0	0.61	19	0.0	0.0	3.8	15	9.4	27

Table 5.2: Differential cross section as a function of Q^2 for the reaction $ep \longrightarrow e\gamma p$ in the kinematic range $2 < Q^2 < 20\,\mathrm{GeV}^2$, $30 < W < 120\,\mathrm{GeV}$ and $|t| < 1\,\mathrm{GeV}^2$. The statistical error δ_{stat} is given in the third column. The bin dependent systematic errors are given in columns four to seven. δ_{global} denotes the global systematic error and δ_{tot} is the total error. The bin dependent systematic errors taken into account are: $\delta_{E_\gamma \pm 4\,\%}$ is the error due to the variation of the energy scale of the LAr calorimeter by $\pm 4\,\%$; $\delta_{E_e \pm 1\,\%}$ stems from the variation of the energy scale of the Spacal by $\pm 1\,\%$; $\delta_{\theta_e \pm 1.3\,\mathrm{mrad}}$ effect from the variation of the angle measurement for the electron by $\pm 1.3\,\mathrm{mrad}$ and $\delta_{\theta_\gamma \pm 3\,\mathrm{mrad}}$ due to the variation of the angle measurement using the LAr calorimeter by $\pm 3\,\mathrm{mrad}$.

The four bin dependent systematic uncertainties are $\delta_{E_\gamma \pm 4\,\%}$ resulting from the variation of the energy scale of the LAr calorimeter by $\pm 4\,\%$, $\delta_{E_e \pm 1\,\%}$ due to the energy scale uncertainty of the Spacal of $1\,\%$, $\delta_{\theta_e \pm 1.3\,\mathrm{mrad}}$ resulting from the variation of the angle measurement for the electron by $1.3\,\mathrm{mrad}$ and $\delta_{\theta_\gamma \pm 3\,\mathrm{mrad}}$ due to the variation of the measured angle using the LAr calorimeter by $3\,\mathrm{mrad}$. Since the kinematic variables have been reconstructed from the scattering angles of the electron and photon the dominating systematic uncertainties originate from the accuracy of their measurement. The largest uncertainty originates from the measurement of the angle of the scattered electron due to the Spacal alignment accuracy. Its absolute position has been determined using two different methods, one based on Bethe–Heitler events [135] and one using track cluster matching between CJC and Spacal [136], which agree within $1.3\,\mathrm{mrad}$. The uncertainty on the energy scales of the calorimeters only effect the event selection and the measurement of $|t|$ and are hence of minor importance.

The systematic uncertainties for the cross section measurement as function of W are slightly smaller than for the measurement in Q^2 since the resolution is better for W than for Q^2 resulting in a smaller sensitivity to a variation of the scattering angles.

5.4 The $\gamma^* p$ Cross Section

The excess of events above the Bethe–Heitler cross section can be attributed to the DVCS process as discussed before. Mandatory for such a clear separation of the two processes is the cancellation of contributions from the interference term . To guarantee this it is important that the detector acceptance is independent of the angle ϕ_R (see chapter 1.3) However due to the fiducial cuts applied in the Spacal and the CJC, one can in principle produce an acceptance resulting in a non–vanishing interference term. Hence before extracting the cross section for the reaction $\gamma^* p \longrightarrow \gamma p$ the ϕ_R acceptance has to be investigated.

range in W	$\frac{\mathrm{d}\sigma^{ep\longrightarrow e\gamma p}}{\mathrm{d}W}$	δ_{stat}	$\delta_{E_\gamma \pm 4\%}$	$\delta_{E_e \pm 1\%}$	$\delta_{\theta_\gamma \pm 3\,\mathrm{mrad}}$	$\delta_{\theta_e \pm 1.3\,\mathrm{mrad}}$	δ_{global}	δ_{tot}
[GeV]	[pb/GeV]	[%]	[%]	[%]	[%]	[%]	[%]	[%]
30 - 60	1.06	14	1.8	0.0	0.0	1.8	9.4	16.8
60 - 80	1.05	18	3.0	0.0	0.0	3.0	9.4	20.8
80 - 100	1.58	14	0.0	0.0	2.0	4.0	9.4	17.9
100 - 120	1.66	20	0.0	0.0	3.9	7.8	9.4	23.7

Table 5.3: Differential cross section as a function of W for the reaction $ep \longrightarrow e\gamma p$ in the kinematic range $2 < Q^2 < 20\,\mathrm{GeV}^2$, $30 < W < 120\,\mathrm{GeV}$ and $|t| < 1\,\mathrm{GeV}^2$. The statistical error δ_{stat} is given in the third column. The bin dependent systematic errors are given in the columns four – seven. δ_{global} denotes the global systematic error and δ_{tot} is the total error. The bin dependent systematic errors taken into account are: $\delta_{E_\gamma \pm 4\%}$ resulting from a variation of the energy scale of the LAr calorimeter by $\pm 4\%$; $\delta_{E_e \pm 1\%}$ due to the variation of the energy scale of the Spacal by $\pm 1\%$; $\delta_{\theta_e \pm 1.3\,\mathrm{mrad}}$ obtained from a variation of the angle measurement for the electron by $\pm 1.3\,\mathrm{mrad}$; $\delta_{\theta_\gamma \pm 3\,\mathrm{mrad}}$ due to the variation of the angle measurement using the LAr calorimeter by $\pm 3\,\mathrm{mrad}$.
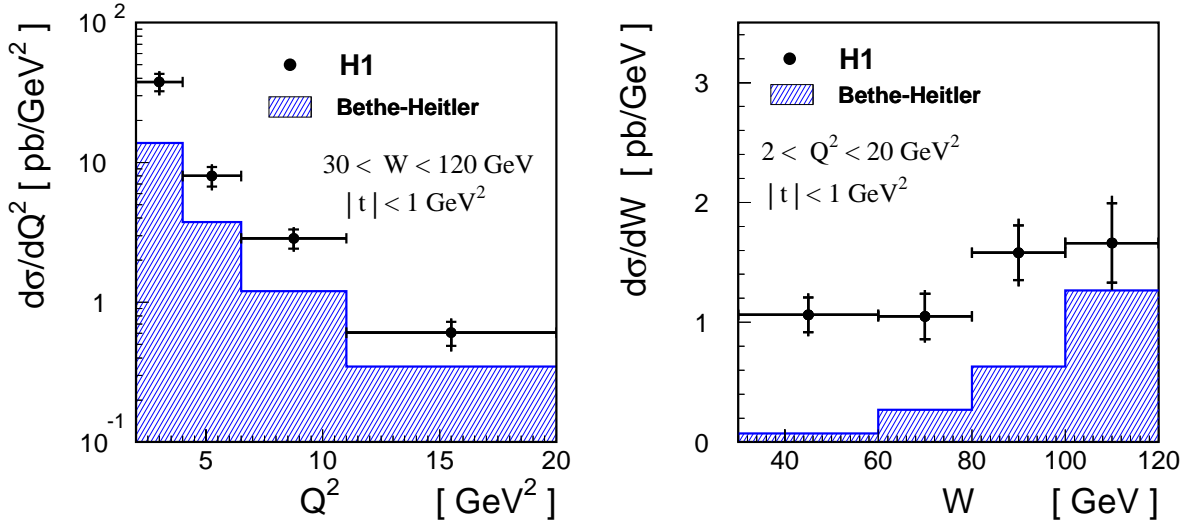

Figure 5.4: Differential cross sections for the reaction $ep \longrightarrow e\gamma p$ in the kinematic range $2 < Q^2 < 20\,\mathrm{GeV}^2$, $30 < W < 120\,\mathrm{GeV}$ and $|t| < 1\,\mathrm{GeV}^2$: left) cross section as function of Q^2; right) cross section in dependence of W. The data are compared to the prediction for the Bethe–Heitler process (shaded histogram). A clear difference in shape and absolute normalisation is observed which is attributed to the DVCS process.

The ϕ_R Acceptance

The ϕ_R acceptance was determined using the TINTIN MC program. Figure 5.5a shows the ϕ_R distribution before and after the fiducial cuts. The two distributions are relatively normalised. Slight differences between the two distributions can be observed but when adding up the events in the region where the interference term has a positive $(-\pi/2 < \phi_R < \pi/2)$ and a negative $(-\pi < \phi_R < -\pi/2$ and $\pi/2 < \phi_R < \pi)$ contribution to the cross section a perfect agreement is

observed (see Figure 5.5 b). Thus the acceptance is such that the contribution of the interference term to the cross section indeed cancels.
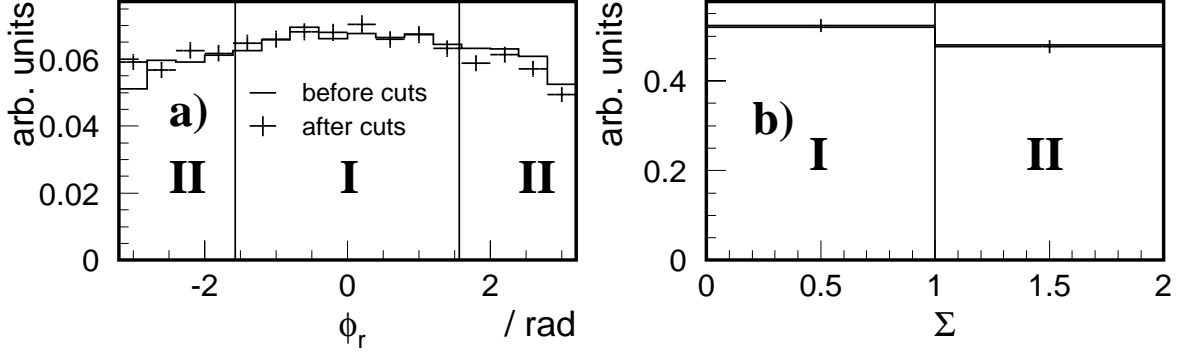

Figure 5.5: a) Distribution of the angle ϕ_R for a MC simulation before and after application of the fiducial cuts. Both distributions are relatively normalised. The region **I** denotes the region $\pi/2 < \phi_R < \pi/2$ where the interference term of the Bethe–Heitler and the DVCS process has a positive contribution to the cross section. In the region **II** the interference term leads to a negative contribution to the cross section. b) Sum of events for the regions I and II (see text for discussion).

Extraction of the $\gamma^* p$ Cross Section

Before one can extract the cross section for the reaction $\gamma^* p \longrightarrow \gamma p$ the Bethe–Heitler contribution has to be subtracted from the measured electron–proton cross section. This has been done using the BH cross section prediction of the COMPTON 2.0 program; the values are listed in Table 5.4.

Q^2–domain			$\frac{\mathrm{d}\sigma^{BH}}{\mathrm{d}Q^2}$		W–domain			$\frac{\mathrm{d}\sigma^{BH}}{\mathrm{d}W}$
[GeV^2]			[pb/GeV^2]		[GeV]			[pb/GeV]
2.0	-	4.0	13.82		30	-	60	0.07
4.0	-	6.5	3.75		60	-	80	0.27
6.5	-	11.0	1.20		80	-	100	0.63
11.0	-	20.0	0.35		100	-	120	1.27

Table 5.4: The cross sections for the Bethe–Heitler contribution to the electron–proton cross section as calculated with the COMPTON 2.0 program as function of Q^2 for $30 < W < 120\,\mathrm{GeV}$ and as function of W for $2 < Q^2 < 20\,\mathrm{GeV}^2$ both for $|t| < 1\,\mathrm{GeV}^2$.

After the subtraction of the Bethe–Heitler contribution the photon–proton cross section can be obtained using the following formula based on the decomposition of the electron–proton cross section into a photon flux and the photon–proton cross section

$$\frac{\mathrm{d}\sigma^{ep \longrightarrow e\gamma p}}{\mathrm{d}Q^2 \mathrm{d}y}\left(Q^2, y\right) = \Gamma\left(Q^2, y\right) \cdot \sigma^{\gamma^* p \longrightarrow \gamma p}\left(Q^2, y\right) \tag{5.12}$$

where Γ is the flux of virtual photons emitted from the incoming electron. It can be approximated for low y using the Hand convention [137]

$$\Gamma = \frac{\alpha_{em}\left(1 - y + \frac{y^2}{2}\right)}{\pi y Q^2}.$$

(5.13)

Here α_{em} represents the electromagnetic coupling constant. Note that while the electron–proton cross section is differential in Q^2 and y, the photon–proton cross section is not.

Using these formulae the photon–proton cross section can be obtained by the following method. When integrating the differential electron–proton cross section one gets

$$\int_{Q^2_{min}}^{Q^2_{max}} \int_{y_{min}}^{y_{max}} \frac{\mathrm{d}^2\sigma^{ep \longrightarrow e\gamma p}}{\mathrm{d}Q^2 \mathrm{d}y} \mathrm{d}Q^2 \mathrm{d}y = \sigma^{ep \longrightarrow e\gamma p} = \frac{C_{tot}N}{\mathcal{L}}$$

(5.14)

where C_{tot} includes all corrections as discussed before (see equations 5.1 and 5.2), N is the number of events in the bin under consideration and $\mathcal{L}$ is the integrated luminosity of the data sample. Hence $\sigma^{ep \longrightarrow e\gamma p}$ is nothing else but the measured differential electron–proton cross section multiplied with the bin width. When integrating the right side of equation 5.12 one obtains the following relation:

$$\sigma^{ep \longrightarrow e\gamma p} = \int_{Q^2_{min}}^{Q^2_{max}} \int_{y_{min}}^{y_{max}} \Gamma\left(Q^2, y\right) \cdot \sigma^{\gamma^* p \longrightarrow \gamma p}\left(Q^2, y\right) \mathrm{d}Q^2 \mathrm{d}y.$$

(5.15)

This relation cannot be simplified further since both $\Gamma\left(Q^2, y\right)$ and $\sigma^{\gamma^* p \longrightarrow \gamma p}\left(Q^2, y\right)$ depend on Q^2 and y. Therefore the $\gamma^* p$ cross section has to be parameterised. In vector meson production the following factorised ansatz has been successfully used [60]:

$$\sigma^{\gamma^* p \longrightarrow \gamma p}\left(Q^2, y\right) = A \cdot y^a \cdot \left(\frac{1}{Q^2}\right)^n$$

(5.16)

with two free parameters a and n. The normalisation factor A can be obtained using this ansatz and solving equation 5.15. Finally one gets the following expression for the photon–proton cross section:

$$\sigma^{\gamma^* p \longrightarrow \gamma p}\left(Q_0^2, y_0\right) = \frac{C_{tot}N}{\mathcal{L}} \cdot \frac{1}{B} \cdot y_0^a \cdot \left(\frac{1}{Q_0^2}\right)^n$$

(5.17)

with

$$B = \frac{\alpha_{em}}{\pi} \int_{y_{min}}^{y_{max}} \mathrm{d}y\, y^a \frac{1 - y + \frac{y^2}{2}}{y} \int_{Q^2_{min}}^{Q^2_{max}} \mathrm{d}Q^2 \frac{1}{Q^2} \left(\frac{1}{Q^2}\right)^n.$$

(5.18)

When calculating the photon–proton cross section as function of Q^2, the bin boundaries Q^2_{max} and Q^2_{min} are chosen as the boundaries of the corresponding bin for the electron–proton cross section. The y–range is chosen such that it corresponds to the full W–region of the measurement $\left(W^2 \approx ys\right)$. For the measurement of the photon–proton cross section as function of W the integration over y corresponds to the bins in W of the electron–proton cross section and the integration over Q^2 is performed for the full range of the measurement. The cross section $\sigma^{\gamma^* p \longrightarrow \gamma p}\left(Q_0^2, y_0\right)$ is the photon–proton cross section at y_0 and Q_0^2. It is not possible to extract the photon–proton cross section and the free parameters a and n at the same time. Therefore an iterative method has been chosen with reasonable starting values a_0 and n_0. By this procedure the $\gamma^* p$ cross section has been extracted and the Q^2 and y dependences have been fitted to

the data and used as new starting values for the next iteration. The procedure converges fast leading to the following result:

$$a = 0.35 \pm 0.22, \tag{5.19}$$
$$n = 1.63 \pm 0.23$$

where the errors originate from the error on the last fit to the photon–proton cross section.

Four data points have been determined as function of Q^2 extrapolated to $W = 75\,\mathrm{GeV}$ where the cross section has been evaluated for the centres of the bins from the electron–proton cross section. The photon–proton cross section as function of W has been determined for $Q^2 = 4.5\,\mathrm{GeV}^2$ where again the bin centres of the electron–proton cross section have been chosen for the data points of the photon–proton cross section.

The final results for the photon–proton cross section are listed in Table 5.5 with the corresponding statistical and systematic errors. When varying the fitted Q^2 and y dependencies within their uncertainties $a = 0.35 \pm 0.22$ and $n = 1.63 \pm 0.23$ the extracted photon–proton cross section changes by 7% which has been accounted for as an additional systematic error. In the next chapter the results are compared with different theoretical predictions.

Q^2 $[\mathrm{GeV}^2]$	$\sigma^{\gamma^*p \to \gamma p}$ [nb]			W [GeV]	$\sigma^{\gamma^*p \to \gamma p}$ [nb]		
3.0	11.0	± 2.4	± 2.5	45	4.33	± 0.64	± 0.54
5.25	3.8	± 1.1	± 1.0	70	5.51	± 1.34	± 0.86
8.75	2.43	± 0.66	± 0.54	90	8.9	± 2.2	± 1.7
15.50	0.64	± 0.30	± 0.28	110	4.8	± 4.0	± 2.6

Table 5.5: *Measured cross section for the elastic DVCS process $\gamma^*p \to \gamma p$ as a function of Q^2 for $W = 75\,\mathrm{GeV}$ and as a function of W for $Q^2 = 4.5\,\mathrm{GeV}^2$, both for $|t| < 1\,\mathrm{GeV}^2$. The first errors are statistical, the second systematic.*

Chapter 6

Discussion of the Results

In this chapter the measured photon–proton cross section of the DVCS process will be compared to different theoretical predictions of which few exist at present.

In Figure 6.1 the measurement is compared to the calculation of Frankfurt, Freund and Strikman (FFS) [97] and the prediction from Donnachie and Dosch (DD) [100]. The cross section is measured as function of Q^2 for $W = 75\,\text{GeV}$ and $|t| < 1\,\text{GeV}^2$ and as function of W for $Q^2 = 4.5\,\text{GeV}^2$ and $|t| < 1\,\text{GeV}^2$. The data are presented as points with statistical errors (inner error bars) and statistical and systematic uncertainties added in quadrature (outer error bars). Since the calculations are performed for $t = t_{\min}$ an exponential function $\frac{\mathrm{d}\sigma}{\mathrm{d}t} \sim e^{-b|t|}$ for the unknown $|t|$ dependence has been assumed with $5 < b < 9\,\text{GeV}^{-2}$ which corresponds to the range measured in vector meson production at HERA and is assumed to be a reasonable range for DVCS. This leads to a normalisation uncertainty of the predictions since the cross section is integrated over t The upper bound for the predictions corresponds to $b = 5\,\text{GeV}^{-2}$ whereas the lower bound is given by $b = 9\,\text{GeV}^{-2}$. Within this uncertainty the data are well described by the theoretical calculations. The absolute normalisation is best for large values of b. For a more definite statement on the normalisation a measurement of the t–slope has however to be performed.

In the model of Frankfurt, Freund and Strikman the cross section was calculated at a normalisation point Q_0^2 using the aligned jet model and the evolution to higher values of Q^2 was performed using leading order evolution kernels for generalised parton distributions. Thus at low values of Q^2 effects of the skewedness have been neglected while they are generated at higher values of Q^2 by the evolution procedure. Within the present accuracy of the data this method is succesfull, most probably due to the small skewedness expected for low values of Q^2 and its effect on the cross section calculation. This observation is in agreement with the measurement of the cross section for light vector meson production where the data can be explained without including effects due to generalised parton distributions.

The model of Donnachie and Dosch is based on the dipole approach where the virtual photon is assumed to fluctuate into a quark antiquark system which subsequently interacts with the proton and then recombines to the real photon. The dipole cross section has been modelled within the framework of the two pomeron approach where small dipoles interact predominantly with the hard pomeron and large dipoles with the soft pomeron. The free parameters of this model have been determined from proton–proton scattering experiments and inclusive diffraction data from HERA measurements. The prediction for DVCS itself has no free parameter.
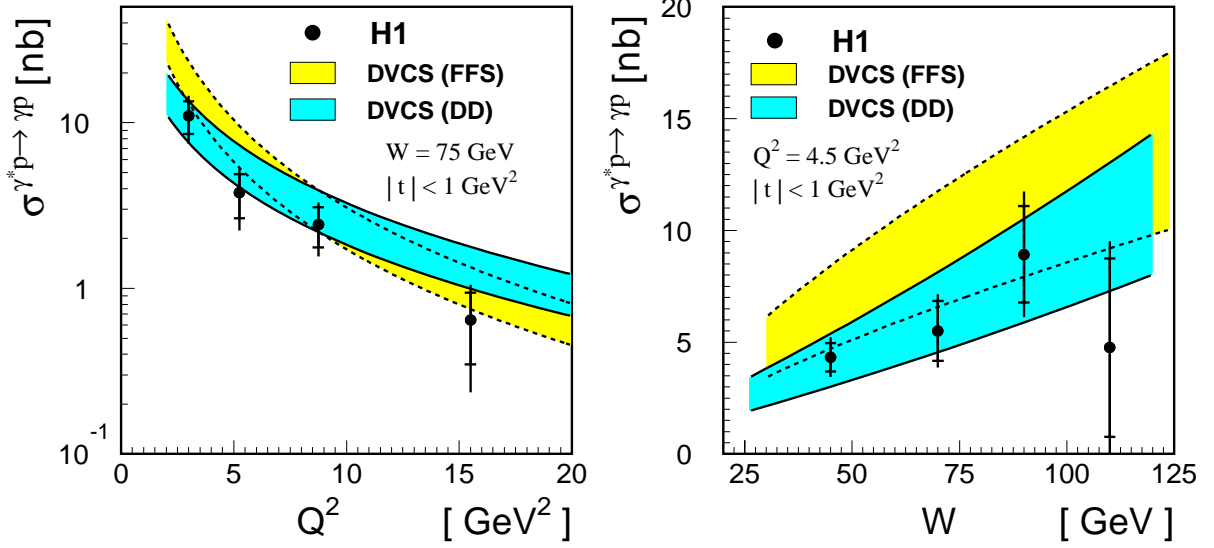
Figure 6.1: *The measurement of the photon–proton cross section of the DVCS process $\gamma^* p \longrightarrow \gamma p$ in the kinematic range $2 < Q^2 < 20 \, \text{GeV}^2$, $30 < W < 120 \, \text{GeV}$ and $|t| < 1 \, \text{GeV}^2$ in comparison to theoretical predictions from Frankfurt, Freund and Strikman (FFS) [97] and Donnachie and Dosch (DD) [100]. The error bars denote the statistical error (inner) and the quadratic sum of the statistical error and the systematic uncertainty (outer): left) Cross section as a function of the photon virtuality Q^2 for $W = 75 \, \text{GeV}$; right) cross section as function of the photon–proton centre of mass energy W for $Q^2 = 4.5 \, \text{GeV}^2$. An exponential $|t|$ dependence $\frac{d\sigma}{dt} \sim e^{-b|t|}$ leading to a normalisation uncertainty indicated by the band for the predictions, has been assumed with $5 < b < 9 \, \text{GeV}^{-2}$. The upper bound of the prediction corresponds to $b = 5 \, \text{GeV}^{-2}$ and the lower bound is given by $b = 9 \, \text{GeV}^{-2}$.*

The model of Donanchie and Dosch predicts a systematicaly lower cross section for the DVCS process in the low Q^2 region $\left(Q^2 < 8 \, \text{GeV}^2\right)$ which leads to an even better agreement with the data. To further investigate the validity of this model more precise data are needed.

Figure 6.2 shows the measurement in comparison with the predictions based on the dipole approach from Forshaw, Kerley and Shaw (FKS) [102, 103] and McDermott, Frankfurt, Guzey and Strikman (MFGS) [102, 104]. Again the calculations are performed for $t = t_{\min}$ and hence an exponential t–dependence has been assumed with the t–slope $b = 7 \, \text{GeV}^{-2}$. When changing the t–slope b to smaller or larger values again the normalisation changes. Although both dipole models depend on very different assumptions they provide an excellent description of the data except at large values of Q^2 where the MFGS prediction tends to be larger than the data. The parameters of these models have been determined from fits to the diffractive structure function $F_2^{D(3)}$ and vector meson production cross sections. They exhibit no free parameter for the DVCS prediction. This can be interpreted as a tight connection existing between the different diffractive processes on which these models are based. In order to investigate these models in further detail again more precise data are needed.
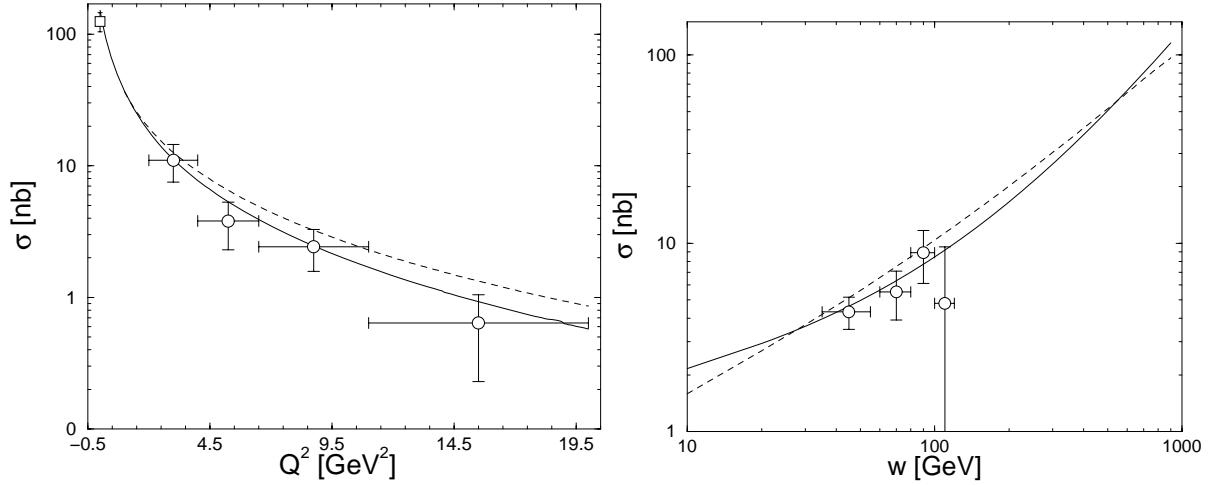
Figure 6.2: *The measurement of the photon–proton cross section of the DVCS process $\gamma^* p \longrightarrow \gamma p$ in the kinematic range $2 < Q^2 < 20\,\mathrm{GeV}^2$, $30 < W < 120\,\mathrm{GeV}$ and $|t| < 1\,\mathrm{GeV}^2$ in comparison to the predictions from Forshaw, Kerley and Shaw (FKS) [102, 103] and McDermott, Frankfurt, Guzey and Strikman (MFGS) [102, 104]: left) Cross section as a function of the photon virtuality Q^2 for $W = 75\,\mathrm{GeV}$ where the data point at $Q^2 \simeq 0\,\mathrm{GeV}^2$ stems from the measured total photon–proton cross section; right) cross section as function of the photon–proton centre of mass energy W for $Q^2 = 4.5\,\mathrm{GeV}^2$. The data are displayed with their total errors. The FKS prediction is indicated by the solid line and the MFGS calculation is represented by the dashed line. An exponential $|t|$ dependence $\frac{d\sigma}{dt} \sim e^{-b|t|}$ has been assumed with $b = 7\,\mathrm{GeV}^{-2}$ leading to a normalisation uncertainty.*

Summary

In this thesis the first measurement of the cross section for elastic Deeply Virtual Compton Scattering (DVCS) in ep collisions has been presented. The data have been taken with the H1 experiment at the electron–proton collider HERA. For ep scattering the DVCS process represents the scattering of a virtual photon off a proton ($\gamma^* p \longrightarrow \gamma p$) where the virtual photon is emitted by the incoming electron. In a QCD based approach the process can be interpreted as a scattering of the photon off a quark from the proton and thus delivers a clean tool to investigate the proton structure. In particular the process resides its interest from the potential access it delivers to the generalised parton densities. A complication of the measurement is that the Bethe–Heitler (BH) process where the electron scatters elastically off the proton and a photon is emitted by the electron has the same signature and is thus indistinguishable from the DVCS process under investigation. However the BH cross section is calculable to high precision in the framework of QED and thus can be subtracted statistically.

The DVCS signal has been established by the selection of events with one electron and one photon candidate measured with the H1 detector in a region of phase space where DVCS is expected to dominate. The data sample was taken in the 1997 data taking period and corresponds to an integrated luminosity of $8\,\mathrm{pb}^{-1}$. A large excess of events over the prediction for the Bethe–Heitler process is observed. To assure the quality of the measurement the detector response has been controlled with a data sample dominated by Bethe–Heitler events.

Using a newly developed DVCS MC program, within the scope of this thesis, the differential electron–proton cross section for the reaction $ep \longrightarrow e\gamma p$ has been extracted as a function of the photon virtuality Q^2 and the photon–proton centre of mass energy W in the kinematic range $2 < Q^2 < 20\,\mathrm{GeV}^2$, $30 < W < 120\,\mathrm{GeV}$ and $|t| < 1\,\mathrm{GeV}^2$ where t denotes the squared momentum transfer at the proton vertex. The cross section has been corrected for several background and detector effects. After subtraction of the contribution of the Bethe–Heitler process the electron–proton cross section has been converted to a photon–proton cross section as function of Q^2 and W. Within the present accuracy QCD based as well as semiclassical models are able to describe the measured cross sections. The main results of this analysis have been published [141].

In order to achieve further progress future measurements with more precise data are needed. This goal can be achieved due to the expected increase of luminosity after the HERA upgrade and the usage of newly installed detectors yielding a decrease of the systematic uncertainties. It is of particular interest to measure the t–dependence of the cross section to overcome the normalisation problem of the theoretical predictions. In addition a measurement of the azimuthal angle asymmetry would provide access to the real part of the QCD amplitude and information on the generalised parton densities.

Appendix A

TINTIN: A DVCS MC program

The MC program TINTIN developed within the scope of this analysis generates the four vectors of the final state particles for events of the reaction $ep \longrightarrow e\gamma p$ and calculates the cross section in a given kinematic range based on the predictions of Frankfurt, Freund and Strikman (see Chapter 2.2). The generated four vectors are interfaced to the H1 detector simulation.

The TINTIN program is based on the Monte Carlo technique (see e.g. [138]) using an acceptance–rejection–method. According to the predicted cross section, the kinematic variables $\left(Q^2, y, t, \phi\right)$ are generated from which the four vectors of the final state particles are reconstructed. The emission of real photons from the incident lepton which is expected to be the largest higher order QED correction for HERA kinematics can optionally be chosen. The implemented photon radiation is based on the collinear approximation [139, 140].

The TINTIN program is implemented in the H1 generator software environment and consists of 11 subroutines. A steering file provides the input to the program (see Table A.1) and the output is written to FPACK–files where the events are stored in form of BOS–banks the H1 internal data format. The basic routines of the program are:

- TIN
  Main routine of the TINTIN program which is called from the H1 generator software.

- TININI
  Initialisation of all parameters for the event generation.

- TINCHA
  The routine reads the steering card and changes the parameters for the event generation.

- TINEVT
  Main routine of the event loop. It generates the number of events as required in the steering file.

  - QED_ISR
    Subroutine which generates the emission of a real photon from the incoming electron line according to the collinear approximation.

  - KINCHA
    Routine which recalculates the kinematic variables according to the energy of the emitted photon from the incident electron.

- KINGEN
Routine which generates the variables Q^2, y, t and ϕ taking the boundary values (e.g. t_{min}) correctly into account.

- CALCSIG
Calculation of the cross section for the generated point in phase space according to the calculations of Frankfurt, Freund and Strikman.

- CALCKIN
Calculation of the four vectors of the outgoing particles.

At the end of the event loop the decision is taken whether a generated event is accepted or rejected according to the defined phase space region.

- TINFILL
Interface to the H1 generator software for the four vectors of the final state particles.

- TINYEND
Calculation of the cross section and final book keeping.

100	!	NEVT	!	Number of events to be generated
-1	!	SIGN	!	lepton beam (+1=electron, -1=positron)
1	!	ITYP	!	generation type(1=sum, 2=BH, 3=DVCS)
1	!	IRAD	!	ISR-flag (0=off/1=on)
1.5	!	Q2MIN	!	minimum Q2 [GeV**2]
1000.0	!	Q2MAX	!	maximum Q2 [GeV**2]
0.0001	!	YMIN	!	minimum y
1.0	!	YMAX	!	maximum y
1.0E-5	!	XMIN	!	minimum x
1.0	!	XMAX	!	maximum x
2.0	!	TMAX	!	max t
27.5	!	ELEP	!	lepton energy [GeV]
820.0	!	EPROT	!	proton energy [GeV]
0.55	!	R	!	IM_A(g*p->g*p)/IM_A(g*p->gp)
4.5	!	B	!	t-slope [GeV**-2]
0.0	!	THLMIN	!	minimal lepton angle [grad]
178.0	!	THLMAX	!	maximal lepton angle [grad]
15.0	!	ELMIN	!	minimal lepton energy [GeV]
0.0	!	THGMIN	!	minimal photon angle [grad]
177.0	!	THGMAX	!	maximal photon angle [grad]
0.3	!	EGMIN	!	minimal photon energy [GeV]
0.0	!	EIMIN	!	minimal ISR photon energy [GeV]

Table A.1: *Typical steering file with the list of parameters which have to be chosen for the event generation.*

Acknowledgements

Bibliography

[1] R. G. Roberts, "The Structure Of The Proton", *Cambridge Univ. Pr., 1990.*

[2] H. Abramowicz and A. Caldwell, Rev. Mod. Phys. **71** (1999) 1275 [arXiv:hep-ex/9903037].

[3] A. Levy, DESY-97-013 *Lectures given at Strong Interaction Study Days, Kloster Banz, Germany, 10-12 Oct 1995.*

[4] M. Göckeler, R. Horsley, D. Pleiter, P. E. Rakow and G. Schierholz, arXiv:hep-ph/0108105.

[5] C. Adloff *et al.* [H1 Collaboration], Eur. Phys. J. C **21** (2001) 33 [arXiv:hep-ex/0012053].

[6] C. Adloff *et al.* [H1 Collaboration], Eur. Phys. J. C **19** (2001) 269 [arXiv:hep-ex/0012052].

[7] C. Adloff *et al.* [H1 Collaboration], Eur. Phys. J. C **13** (2000) 609 [arXiv:hep-ex/9908059].

[8] J. Breitweg *et al.* [ZEUS Collaboration], Eur. Phys. J. C **12** (2000) 411 [arXiv:hep-ex/9907010].

[9] S. Chekanov *et al.* [ZEUS Collaboration], arXiv:hep-ex/0105090.

[10] A. C. Benvenuti *et al.* [BCDMS Collaboration], Phys. Lett. B **223** (1989) 485.

[11] M. R. Adams *et al.* [E665 Collaboration], Phys. Rev. D **54** (1996) 3006.

[12] M. Arneodo *et al.* [New Muon Collaboration (NMC)], Nucl. Phys. B **483** (1997) 3.

[13] E. D. Bloom *et al.*, Phys. Rev. Lett. **23** (1969) 930.

[14] M. Breidenbach *et al.*, Phys. Rev. Lett. **23** (1969) 935.

[15] J. D. Bjorken, Phys. Rev. **179** (1969) 1547.

[16] J. D. Bjorken and E. A. Paschos, Phys. Rev. **185** (1969) 1975.

[17] R. P. Feynman, Phys. Rev. Lett. **23** (1969) 1415.

[18] R. P. Feynman, *Photon Hadron Interactions*, Bejamin 1972.

[19] D. J. Fox *et al.*, Phys. Rev. Lett. **33** (1974) 1504.

[20] H. D. Politzer, Phys. Rev. Lett. **30** (1973) 1346.

[21] D. J. Gross and F. Wilczek, Phys. Rev. D **8** (1973) 3633.

[22] D. J. Gross and F. Wilczek, Phys. Rev. Lett. **30** (1973) 1343.

[23] D. J. Gross and F. Wilczek, Phys. Rev. D **9** (1974) 980.

[24] M. Gell-Mann, Phys. Lett. **8** (1964) 214.

[25] G. Zweig, CERN-TH-412.

[26] J. C. Collins, D. E. Soper and G. Sterman, Nucl. Phys. B **261** (1985) 104.

[27] J. R. Forshaw and D. A. Ross, "Quantum chromodynamics and the pomeron", *Cambridge Univ. Pr., 1997.*

[28] Y. L. Dokshitzer, Sov. Phys. JETP **46** (1977) 641 [Zh. Eksp. Teor. Fiz. **73** (1977) 1216].

[29] V. N. Gribov and L. N. Lipatov, Yad. Fiz. **15** (1972) 781 [Sov. J. Nucl. Phys. **15** (1972) 438].

[30] V. N. Gribov and L. N. Lipatov, Yad. Fiz. **15** (1972) 1218 [Sov. J. Nucl. Phys. **15** (1972) 675].

[31] G. Altarelli and G. Parisi, Nucl. Phys. B **126** (1977) 298.

[32] K. G. Wilson, Phys. Rev. **179** (1969) 1499.

[33] E. A. Kuraev, L. N. Lipatov and V. S. Fadin, Sov. Phys. JETP **44** (1976) 443 [Zh. Eksp. Teor. Fiz. **71** (1976) 840].

[34] E. A. Kuraev, L. N. Lipatov and V. S. Fadin, Sov. Phys. JETP **45** (1977) 199 [Zh. Eksp. Teor. Fiz. **72** (1977) 377].

[35] I. I. Balitsky and L. N. Lipatov, Sov. J. Nucl. Phys. **28** (1978) 822 [Yad. Fiz. **28** (1978) 1597].

[36] M. Ciafaloni, Nucl. Phys. B **296** (1988) 49.

[37] G. Marchesini, Nucl. Phys. B **445** (1995) 49 [arXiv:hep-ph/9412327].

[38] S. Catani, F. Fiorani and G. Marchesini, Nucl. Phys. B **336** (1990) 18.

[39] C. Adloff *et al.* [H1 Collaboration], Nucl. Phys. B **538** (1999) 3 [arXiv:hep-ex/9809028].

[40] C. Adloff *et al.* [H1 Collaboration], Phys. Lett. B **462** (1999) 440 [arXiv:hep-ex/9907030].

[41] M. Glück, E. Reya and A. Vogt, Z. Phys. C **53** (1992) 127.

[42] M. Glück, E. Reya and A. Vogt, Eur. Phys. J. C **5** (1998) 461 [arXiv:hep-ph/9806404].

[43] M. Botje, arXiv:hep-ph/0110123.

[44] A. B. Kaidalov, Phys. Rept. **50** (1979) 157.

[45] G. Alberi and G. Goggi, Phys. Rept. **74** (1981) 1.

[46] K. Goulianos, Phys. Rept. **101** (1983) 169.

[47] P. D. Collins, "An Introduction To Regge Theory And High-Energy Physics", *Cambridge Univ. Pr., 1977.*

[48] A. Donnachie and P. V. Landshoff, Phys. Lett. B **296** (1992) 227 [arXiv:hep-ph/9209205].

[49] G. Ingelman and P. E. Schlein, Phys. Lett. B **152** (1985) 256.

[50] R. Bonino *et al.* [UA8 Collaboration], Phys. Lett. B **211** (1988) 239.

[51] A. Brandt *et al.* [UA8 Collaboration], Phys. Lett. B **297** (1992) 417.

[52] T. Ahmed *et al.* [H1 Collaboration], Nucl. Phys. B **429** (1994) 477.

[53] T. Ahmed *et al.* [H1 Collaboration], Nucl. Phys. B **435** (1995) 3.

[54] M. Derrick *et al.* [ZEUS Collaboration], Phys. Lett. B **346** (1995) 399 [arXiv:hep-ex/9501011].

[55] M. Derrick *et al.* [ZEUS Collaboration], Phys. Lett. B **315** (1993) 481.

[56] J. C. Collins, Phys. Rev. D **57** (1998) 3051 [Erratum-ibid. D **61** (1998) 019902] [arXiv:hep-ph/9709499].

[57] C. Adloff *et al.* [H1 Collaboration], Z. Phys. C **76** (1997) 613 [arXiv:hep-ex/9708016].

[58] C. Adloff *et al.* [H1 Collaboration], Eur. Phys. J. C **20** (2001) 29 [arXiv:hep-ex/0012051].

[59] C. Adloff *et al.* [H1 Collaboration], arXiv:hep-ex/0108047.

[60] C. Adloff *et al.* [H1 Collaboration], Eur. Phys. J. C **13** (2000) 371 [arXiv:hep-ex/9902019].

[61] C. Adloff *et al.* [H1 Collaboration], Eur. Phys. J. C **10** (1999) 373 [arXiv:hep-ex/9903008].

[62] C. Adloff *et al.* [H1 Collaboration], Phys. Lett. B **483** (2000) 23 [arXiv:hep-ex/0003020].

[63] C. Adloff *et al.* [H1 Collaboration], Phys. Lett. B **483** (2000) 360 [arXiv:hep-ex/0005010].

[64] J. Breitweg *et al.* [ZEUS Collaboration], Phys. Lett. B **437** (1998) 432 [arXiv:hep-ex/9807020].

[65] J. Breitweg *et al.* [ZEUS Collaboration], Eur. Phys. J. C **6** (1999) 603 [arXiv:hep-ex/9808020].

[66] J. Breitweg *et al.* [ZEUS Collaborations], Eur. Phys. J. C **12** (2000) 393 [arXiv:hep-ex/9908026].

[67] J. Breitweg *et al.* [ZEUS Collaboration], Eur. Phys. J. C **14** (2000) 213 [arXiv:hep-ex/9910038].

[68] J. Breitweg *et al.* [ZEUS Collaboration], arXiv:hep-ex/0006013.

[69] J. J. Sakurai, Annals Phys. **11** (1960) 1.

[70] A. Donnachie and P. V. Landshoff, Phys. Lett. B **348** (1995) 213 [arXiv:hep-ph/9411368].

[71] M. G. Ryskin, Z. Phys. C **57** (1993) 89.

[72] A. Kreisel, talk at DIS, Bologna, 2001

[73] F. E. Low, Phys. Rev. D **12** (1975) 163.

[74] S. Nussinov, Phys. Rev. Lett. **34** (1975) 1286.

[75] J. C. Collins, L. Frankfurt and M. Strikman, Phys. Rev. D **56** (1997) 2982 [arXiv:hep-ph/9611433].

[76] X. Ji, W. Melnitchouk and X. Song, Phys. Rev. D **56** (1997) 5511 [arXiv:hep-ph/9702379].

[77] B. Geyer, D. Robaschik, M. Bordag and J. Horejsi, Z. Phys. C **26** (1985) 591.

[78] T. Braunschweig, B. Geyer, J. Horejsi and D. Robaschik, Z. Phys. C **33** (1986) 275.

[79] F. M. Dittes, D. Müller, D. Robaschik, B. Geyer and J. Horejsi, Phys. Lett. B **209** (1988) 325.

[80] D. Müller, D. Robaschik, B. Geyer, F. M. Dittes and J. Horejsi, Fortsch. Phys. **42** (1994) 101 [arXiv:hep-ph/9812448].

[81] P. Jain and J. P. Ralston, arXiv:hep-ph/9305250.

[82] X. Ji, Phys. Rev. Lett. **78** (1997) 610 [arXiv:hep-ph/9603249].

[83] X. Ji, Phys. Rev. D **55** (1997) 7114 [arXiv:hep-ph/9609381].

[84] A. V. Radyushkin, Phys. Rev. D **56** (1997) 5524 [arXiv:hep-ph/9704207].

[85] M. Diehl, T. Feldmann, R. Jakob and P. Kroll, Eur. Phys. J. C **8** (1999) 409 [arXiv:hep-ph/9811253].

[86] A. V. Radyushkin, Phys. Lett. B **380** (1996) 417 [arXiv:hep-ph/9604317].

[87] A. V. Radyushkin, arXiv:hep-ph/0101225.

[88] V. Y. Petrov, P. V. Pobylitsa, V. Polyakov, I. Bornig, K. Goeke and C. Weiss, Phys. Rev. D **57** (1998) 4325 [arXiv:hep-ph/9710270].

[89] M. Penttinen, V. Polyakov and K. Goeke, Phys. Rev. D **62** (2000) 014024 [arXiv:hep-ph/9909489].

[90] V. Polyakov and C. Weiss, Phys. Rev. D **60** (1999) 114017 [arXiv:hep-ph/9902451].

[91] A. D. Martin, M. G. Ryskin and T. Teubner, Phys. Lett. B **454** (1999) 339 [arXiv:hep-ph/9901420].

[92] G. P. Lepage and S. J. Brodsky, Phys. Lett. B **87** (1979) 359.

[93] A. V. Efremov and A. V. Radyushkin, Phys. Lett. B **94** (1980) 245.

[94] J. C. Collins and A. Freund, Phys. Rev. D **59** (1999) 074009 [arXiv:hep-ph/9801262].

[95] M. Diehl, T. Gousset, B. Pire and J. P. Ralston, Phys. Lett. B **411** (1997) 193 [arXiv:hep-ph/9706344].

[96] A. Freund, Nucl. Phys. Proc. Suppl. **79** (1999) 368 [arXiv:hep-ph/9905233].

[97] L. L. Frankfurt, A. Freund and M. Strikman, Phys. Rev. D **58** (1998) 114001 [Erratum-ibid. D **59** (1998) 119901] [arXiv:hep-ph/9710356].

[98] L. L. Frankfurt and M. I. Strikman, Phys. Rept. **160** (1988) 235.

[99] G. R. Kerley and M. McDermott, J. Phys. G **G26** (2000) 683 [arXiv:hep-ph/0001050].

[100] A. Donnachie and H. G. Dosch, Phys. Lett. B **502** (2001) 74 [arXiv:hep-ph/0010227].

[101] A. Donnachie and P. V. Landshoff, Phys. Lett. B **437** (1998) 408 [arXiv:hep-ph/9806344].

[102] M. McDermott, R. Sandapen and G. Shaw, arXiv:hep-ph/0107224.

[103] J. R. Forshaw, G. Kerley and G. Shaw, Phys. Rev. D **60** (1999) 074012 [arXiv:hep-ph/9903341].

[104] M. McDermott, L. Frankfurt, V. Guzey and M. Strikman, Eur. Phys. J. C **16** (2000) 641 [arXiv:hep-ph/9912547].

[105] A. Freund and M. F. McDermott, arXiv:hep-ph/0106115.

[106] A. Freund and M. F. McDermott, arXiv:hep-ph/0106124.

[107] A. Freund and M. F. McDermott, arXiv:hep-ph/0106319.

[108] R. S. Thorne, A. D. Martin, W. J. Stirling and R. G. Roberts, arXiv:hep-ph/0106075.

[109] H. Abramowicz and A. Levy, arXiv:hep-ph/9712415.

[110] T. Carli, A. Courau, S. Kermiche and P. Kessler, *In Proceedings, Physics at HERA, vol. 3, 1468-1472, Hamburg, 1991.*

[111] A. Courau, S. Kermiche, T. Carli and P. Kessler, *In Proceedings, Physics at HERA, vol. 2, 902-915, Hamburg, 1991.*

[112] A. Courau and P. Kessler, Phys. Rev. D **46** (1992) 117.

[113] B. List and A. Mastroberardino, *Prepared for Workshop on Monte Carlo Generators for HERA Physics (Plenary Starting Meeting), Hamburg, Germany, 27-30 Apr 1998.*

[114] T. Abe, Comput. Phys. Commun. **136** (2001) 126 [arXiv:hep-ph/0012029].

[115] G. A. Schuler and H. Spiesberger, *In Proceedings, Physics at HERA, vol. 3, 1419-1432, Hamburg, 1991.*

[116] G. Marchesini, B. R. Webber, G. Abbiendi, I. G. Knowles, M. H. Seymour and L. Stanco, Comput. Phys. Commun. **67** (1992) 465.

[117] C. Wissing, "Bestimmung der Charakteristika des Flugzeitsystems des H1–Detektors zur Messung des Strahluntergrundes" (In German), Diploma thesis, Universität Dortmund, 1998.

[118] H1 Collaboration, I. Abt et al., Nucl. Instrum. Methods A 3 86(1997) 310 and 348.

[119] B. Andrieu *et al.* [H1 Calorimeter Group Collaboration], Nucl. Instrum. Meth. A **336** (1993) 460.

[120] R. D. Appuhn *et al.* [H1 SPACAL Group Collaboration], Nucl. Instrum. Meth. A **386** (1997) 397.

[121] T. Nicholls *et al.* [H1 SPACAL Group Collaboration], Nucl. Instrum. Meth. A **374** (1996) 149.

[122] P. Van Esch *et al.*, Nucl. Instrum. Meth. A **446** (2000) 409 [arXiv:hep-ex/0001046].

[123] M. Dirkmann, "Messung der diffraktiven Strukturfunktion $F_2^{D(3)}$ des Protons bei kleinen Impulsüberträgen mit dem H1-Detektor" (In German), Dissertation, Universität Dortmund, 1998.

[124] R. Stamen, talk at DPG, Heidelberg, 1999

[125] R. Stamen, talk at the H1 trigger Workshop, Schloß Ringberg, 2000

[126] R. Brun, R. Hagelberg, M. Hansroul and J. C. Lassalle, CERN-DD-78-2-REV.

[127] M. Dirkmann, "Untersuchungen an einem Spaghetti–Kalorimeter unter besonderer Berücksichtigung des inneren Randbereiches und des Nachweises von Pi-Mesonen" (In German), Diploma thesis, Universität Dortmund, 1995.

[128] B. Heinemann, "Measurement of charged current and neutral current cross sections in positron proton collisions at $\sqrt{s} \approx 300\,\text{GeV}$", Dissertation, Universität Hamburg, 1999, DESY-THESIS-1999-046.

[129] D. Schmidt, "Diffractive photoproduction of charmonium in the H1 detector at HERA" (In German), Dissertation, Universität Hamburg, 2001, DESY-THESIS-2001-029.

[130] P. D. Thompson, "Open Charm Production in Inclusive and Diffractive Deep–Inelastic Scattering at HERA", Dissertation, University of Birmingham, 1999.

[131] X. Janssen, private communication.

[132] V. Lendermann, "Measurement of the QED Compton Scattering Cross Section with the H1 Detector at HERA", Dissertation, Universität Dortmund, 2001.

[133] G. Källen, *Elementary Particle Physics*, Addison–Wesley Publ. Comp.

[134] R. Wallny, "Measurement and QCD analysis of the structure function $F_2\left(x, Q^2\right)$", Dissertation, Universität Zürich, 2001.

[135] R. Stamen, "Analyse quasireeller QED-Compton–Ereignisse" (In German), Diploma thesis, Universität Dortmund, 1998.

[136] A. Glazov, "Measurement of the Proton Structure Functions $F_2\left(x, Q^2\right)$ and $F_L\left(X, Q^2\right)$ with H1 Detector at HERA", Dissertation, Humboldt–Universität Berlin, 1998.

[137] L. N. Hand, Phys. Rev. **129** (1963) 1834.

[138] R. Y. Rubinstein, "Simulation and the Monte Carlo Method", *John Wiley and Sons, Inc., New York, 1981.*

[139] G. Pancheri, P. Touschek, Nuovo Cim. B **51** (1962) 216.

[140] G. Pancheri, Nuovo Cim. A **60** (1963) 321.

[141] C. Adloff *et al.* [H1 Collaboration], Phys. Lett. B **517** (2001) 47 [arXiv:hep-ex/0107005].